

Intelligent Computation for Clinical Data Processing in Intensive Care Units

Lead Guest Editor: Abbas AlZubaidi

Guest Editors: Kazunori Uemura, Saif Al-Shaikhli, and Ahmed F. Hussein





Intelligent Computation for Clinical Data Processing in Intensive Care Units

Journal of Healthcare Engineering

Intelligent Computation for Clinical Data Processing in Intensive Care Units

Lead Guest Editor: Abbas AlZubaidi

Guest Editors: Kazunori Uemura, Saif Al-Shaikhli,
and Ahmed F. Hussein



Copyright © 2020 Hindawi Limited. All rights reserved.

This is a special issue published in "Journal of Healthcare Engineering." All articles are open access articles distributed under the Creative Commons Attribution License, which permits unrestricted use, distribution, and reproduction in any medium, provided the original work is properly cited.

Associate Editors

Xiao-Jun Chen , China
Feng-Huei Lin , Taiwan
Maria Lindén, Sweden

Academic Editors



Cherif Adnen, Tunisia
Saverio Affatato , Italy
Óscar Belmonte Fernández, Spain
Sweta Bhattacharya , India
Prabadevi Boopathy , India
Weiwei Cai, USA
Gin-Shin Chen , Taiwan
Hongwei Chen, USA
Daniel H.K. Chow, Hong Kong
Gianluca Ciardelli , Italy
Olawande Daramola, South Africa
Elena De Momi, Italy
Costantino Del Gaudio , Italy
Ayush Dogra , India
Luobing Dong, China
Daniel Espino , United Kingdom
Sadiq Fareed , China
Mostafa Fatemi, USA
Jesus Favela , Mexico
Jesus Fontecha , Spain
Agostino Forestiero , Italy
Jean-Luc Gennisson, France
Badicu Georgian , Romania
Mehdi Gheisari , China
Luca Giancardo , USA
Antonio Gloria , Italy
Kheng Lim Goh , Singapore
Carlos Gómez , Spain
Philippe Gorce, France
Vincenzo Guarino , Italy
Muhammet Gul, Turkey
Valentina Hartwig , Italy
David Hewson , United Kingdom
Yan Chai Hum, Malaysia
Ernesto Iadanza , Italy
Cosimo Ieracitano, Italy

Giovanni Improta , Italy
Norio Iriguchi , Japan
Mihajlo Jakovljevic , Japan
Rutvij Jhaveri, India
Yizhang Jiang , China
Zhongwei Jiang , Japan
Rajesh Kaluri , India
Venkatachalam Kandasamy , Czech Republic
Pushpendu Kar , India
Rashed Karim , United Kingdom
Pasi A. Karjalainen , Finland
John S. Katsanis, Greece
Smith Khare , United Kingdom
Terry K.K. Koo , USA
Srinivas Koppu, India
Jui-Yang Lai , Taiwan
Kuruva Lakshmanna , India
Xiang Li, USA
Lun-De Liao, Singapore
Qiu-Hua Lin , China
Aiping Liu , China
Zufu Lu , Australia
Basem M. ElHalawany , Egypt
Praveen Kumar Reddy Maddikunta , India
Ilias Maglogiannis, Greece
Saverio Maietta , Italy
M.Sabarimalai Manikandan, India
Mehran Moazen , United Kingdom
Senthilkumar Mohan, India
Sanjay Mohapatra, India
Rafael Morales , Spain
Mehrbakhsh Nilashi , Malaysia
Sharnil Pandya, India
Jialin Peng , China
Vincenzo Positano , Italy
Saeed Mian Qaisar , Saudi Arabia
Alessandro Ramalli , Italy
Alessandro Reali , Italy
Vito Ricotta, Italy
Jose Joaquin Rieta , Spain
Emanuele Rizzuto , Italy

Dinesh Rokaya, Thailand
Sébastien Roth, France
Simo Saarakkala , Finland
Mangal Sain , Republic of Korea
Nadeem Sarwar, Pakistan
Emiliano Schena , Italy
Prof. Asadullah Shaikh, Saudi Arabia
Jiann-Shing Shieh , Taiwan
Tiago H. Silva , Portugal
Sharan Srinivas , USA
Kathiravan Srinivasan , India
Neelakandan Subramani, India
Le Sun, China
Fabrizio Taffoni , Italy
Jinshan Tang, USA
Ioannis G. Tollis, Greece
Ikram Ud Din, Pakistan
Sathishkumar V E , Republic of Korea
Cesare F. Valenti , Italy
Qiang Wang, China
Uche Wejinya, USA
Yuxiang Wu , China
Ying Yang , United Kingdom
Elisabetta Zanetti , Italy
Haihong Zhang, Singapore
Ping Zhou , USA


Contents

Comparative Analysis of Cutting Forces, Torques, and Vibration in Drilling of Bovine, Porcine, and Artificial Femur Bone with Considerations for Robot Effector Stiffness

Oluseyi Adewale Orelaja , Xingsong Wang , Donghua Shen, Dauda Sh. Ibrahim, Tianzheng Zhao, Umer Sharif, and Ishola A. Afiz

Research Article (12 pages), Article ID 8817422, Volume 2020 (2020)

Automatic Detection of Brain Tumor on Computed Tomography Images for Patients in the Intensive Care Unit

Fahmi Fahmi , Fitri Apriyulida, Irina Kemala Nasution, and Sawaluddin




Research Article (13 pages), Article ID 2483285, Volume 2020 (2020)

Cortical Tasks-Based Optimal Filter Selection: An fNIRS Study

Rayyan Azam Khan , Noman Naseer , Sajid Saleem, Nauman Khalid Qureshi , Farzan Majeed Noori , and Muhammad Jawad Khan

Research Article (15 pages), Article ID 9152369, Volume 2020 (2020)

Modular Organization of Muscle Synergies to Achieve Movement Behaviors

Kunkun Zhao , Zhisheng Zhang , Haiying Wen, Zihan Wang, and Jiankang Wu 

Research Article (9 pages), Article ID 8130297, Volume 2019 (2019)

Research Article

Comparative Analysis of Cutting Forces, Torques, and Vibration in Drilling of Bovine, Porcine, and Artificial Femur Bone with Considerations for Robot Effector Stiffness

Oluseyi Adewale Orelaja ^{1,2}, Xingsong Wang ¹, Donghua Shen,¹ Dauda Sh. Ibrahim,¹ Tianzheng Zhao,¹ Umer Sharif,¹ and Ishola A. Afiz³

¹School of Mechanical Engineering, Southeast University, Nanjing, China

²Department of Mechanical Engineering, Moshood Abiola Polytechnic, Abeokuta, Ogun, Nigeria

³Department of Mechanical Engineering, Federal University of Agriculture, Abeokuta, Ogun, Nigeria

Correspondence should be addressed to Xingsong Wang; 101003909@seu.edu.cn

Received 26 June 2020; Revised 6 September 2020; Accepted 23 September 2020; Published 20 October 2020

Academic Editor: Abbas AlZubaidi

Copyright © 2020 Oluseyi Adewale Orelaja et al. This is an open access article distributed under the Creative Commons Attribution License, which permits unrestricted use, distribution, and reproduction in any medium, provided the original work is properly cited.

Bone drilling is known as one of the most sensitive milling processes in biomedical engineering field. Fracture behavior of this cortical bone during drilling has attracted the attention of many researchers; however, there are still impending concerns such as necrosis, tool breakage, and microcracks due to high cutting forces, torques, and high vibration while drilling. This paper presents a comparative analysis of the cutting forces, torques, and vibration resulted on different bone samples (bovine, porcine, and artificial femur) using a 6dof Robot arm effector with considerations of its stiffness effects. Experiments were conducted on two spindle speeds of 1000 and 1500 rpm with a drill bit diameter of 2.5 mm and 6 mm depth of cut. The results obtained from the specimens were processed and analyzed using MATLAB R2015b and Visio 2000 software; these results were then compared with a prior test using manual and conventional drilling methods. The results obtained show that there is a significant drop in the average values of maximum drilling force for all the bone specimens when the spindle speed changes from 1000 rev/min to 1500 rev/min, with a drop from (20.07 to 12.34 N), approximately 23.85% for bovine, (11.25 to 8.14 N) with 16.03% for porcine, and (5.62 to 3.86 N) with 33.99% for artificial femur. The maximum average values of torque also decrease from 41.2 to 24.2 N-mm (bovine), 37.0 to 21.6 N-mm (porcine), and 13.6 to 6.7 N-mm (artificial femur), respectively. At an increase in the spindle speed, the vibration amplitude on all the bone samples also increases considerably. The variation in drilling force, torque, and vibration in our result also confirm that the stiffness of the robot effector joint has negative effect on the bone precision during drilling process.

1. Introduction

Bone drilling is a repair technique which involves creating a pilot hole for proper insertion or screwing on the already inserted plate, or for attaching prosthetic devices to provide rigidity and prevent misalignment of the fractured bone [1–3]. The bone is a hard, anisotropic, heterogeneous, and viscoelastic connective tissue that constitute the skeletal system, exhibiting piezoelectric properties due to the complexity of the binding structure in the dry state. However, bone is a poor conductor of heat, with the thermal

conductivity of fresh cortical bone at approximately 0.38–2.3 J/m·sK¹. It means that bone could not dissipate the heat generated immediately when cutting forces are applied on it, and consequently, temperature in the drilled site is increased [4]. According to Currey [5], bone has high stiffness features, therefore tends to break or fracture when subjected to high external forces. Yearly, around seven million car accidents happen in the United State of America, resulting in femur shaft fractures [6], which could be attributed to reckless driving and over speeding on highways. According to Gupta and Tse [7], femur is the longest and

strongest bone in the human body, with its fractures occurring in middle-age patients which are due to high energy impact force, while mostly due to low energy or impact fall in aged women.

Bone drilling is a repair process peculiar to a femur fracture, which involves creating a pilot hole for proper insertion or screwing on the already inserted plate to avoid misalignment. However, drilling an accurate hole with minimal cutting force and vibration to prevent cracks, and tool breakage, or with no complication, are essential. Often, surgical drill is operated manually by a surgeon, and in some cases, the operation requires considerable skill and a high degree of mental and utmost concentration. Although the use of robots in the theatre room is so enormous now due to its flexibility, the adequacy and usefulness in various areas of surgical fields are paramount [8]. In this work, Hans Robot model HREF 01-LD010-1000-SI was employed for the drilling. The drilling and navigation were done by the robot effector which complemented the aspects of computer-assisted orthopedic surgery [9] due to high precision level. Improper bone drilling procedure can negate the clinical result due to the following: (1) high cutting force and (2) torques and (3) excessive vibration and (4) type of the cutting tools [10]. High forces, torques, and extreme vibration are caused by improper tooling and use of manual drilling method, resulting to serious complications [11]. This research is based on the critical criteria that affect surgical bone drilling [9, 12–14], as well as checking the relationship between the amount of forces, torques, and vibration while drilling different bone samples with utmost consideration of the robot effector stiffness and possible error limits compensation [15]. In this experiment, bovine bone was used to replace human femur because of the similarity in their properties as described by Poumarat et al. [15, 16]. The determination of the successful surgical drilling method depends mostly on parameters such as force, torque, and vibration [17, 18]. Many researchers have compared surgical drilling of bovine and artificial femur [19], but no one has considered bovine, porcine, and artificial femur with utmost consideration for the stiffness on the effector of the robot arm during their investigations. However, due to low drilling accuracy resulting from weak stiffness and low kinematic accuracy, industrial robot is rarely applied in precision machining process [20]. Therefore, in order to reduce deformation or backlash due to vibration during bone drilling, robot stiffness influence should be considered; hence, this study is focused on measuring and comparing the cutting forces, torque and vibration on the bone while drilling, with consideration of the robot stiffness.

2. Methods

2.1. The Bone Drilling Set-Up System. The set-up of the experiment involved 6dof Hans Robot which is a PC-based and single phase 220 V (50–60 Hz, power 1.5 kW) electric motor with a speed control range of 1500 rpm. Also, a four-component dynamometer (Kistler Type 9272 A) was calibrated and mounted on the work platform. The ICAM amplifier was set with the PC software to measure this range

of coulomb: ± 100 pC and ± 10 pC; data acquisition system measured the electrical current signals from the force sensor in accordance to the exerted force and torque across all the axes, a vibrator sensor (accelerometer) of frequency range of 20–30 Hz was also attached to each of the bone specimen to measure the resulted vibration, and a charge controller regulates voltage and a computer system interprets the visible signals. The hardware block diagram is shown in Figure 1.

2.2. Bone Samples for Drilling. The bone samples used for the experiments were excised from the middle portion of the bovine and porcine femur (see Figures 2(a) and 2(b)) and obtained from butchers shop (Table 1). The residue tissues on the femur were stripped off to ensure that no defect of any sort is seen on the bones, followed by refrigeration to a temperature of about -20°C before drilling and allowed to thaw at 24°C ambient room temperature for at least 90 minutes before the drilling. The composite femur (large left femur, Model 3310, Sawbones, Pacific Research Labs, Vashon Island, WA, USA) samples were purchased for the experiments and used as received, as shown in Figure 2(c).

2.3. Mechanical Properties of Human Bone, Bovine Bone, and Pig Bone. Mechanical properties of human bone, bovine bone, and pig bone are given in Table 1.

2.4. Drilling Method and Mechanical Modeling. The parameters used for drilling in this experiment are provided in Tables 2 and 3. The drill bit diameter, range of drill speed, and feed rates used in this study are widely reported in the literature related to robotic and navigation procedures and applications of bone drilling as suggested by previous works [17, 23–25]. During the drilling, the force, torque, and vibration measurements were recorded in z -axis only.

The robot-effector's arm was set to drill through the depth of 6 mm for all the specimens, while the drilling force, torque, and bone vibration were measured in z -axis only at varying cutting speed of 1000 rpm and 1500 rpm. This procedure was repeated twice to ensure repeatability and error-free. Figure 3 shows the drilling procedure using the 6dof Hans Robot for bone drilling.

2.5. Modeling of Robot Effector Stiffness. The stiffness of a robot is of great importance to accurately manipulate drilling operation. It shows the accuracy and the rigidity needed by the force effector to drill with less vibration and deflections [26, 27]. Figure 4(a) shows the complete set-up of the Hans Robot manipulation process; however, it is essential to model the stiffness of the Hans Robot when drilling to compensate for errors that could occur due to external forces on the effector. Modeling the stiffness end of the effector is done by applying Jacobian matrix principle to identify the relationship between joint rotation and end effector motion, as shown in Figure 4(b).

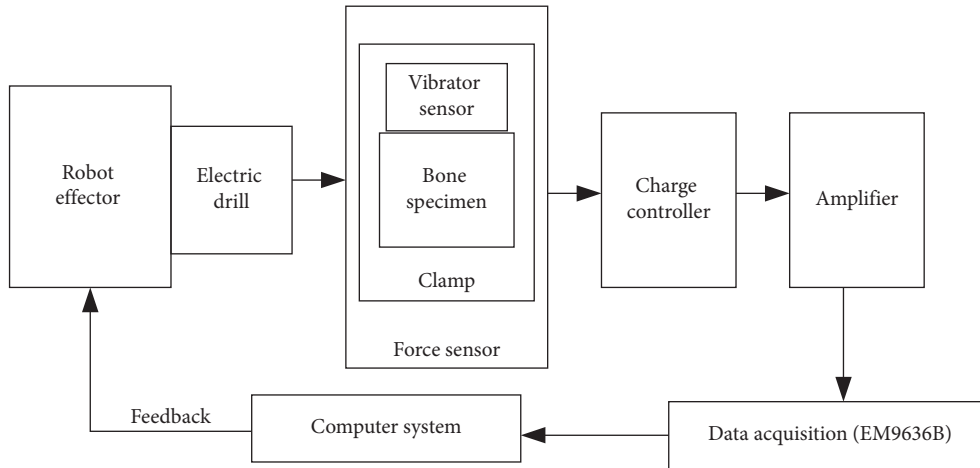


FIGURE 1: The block diagram of the bone drilling process.

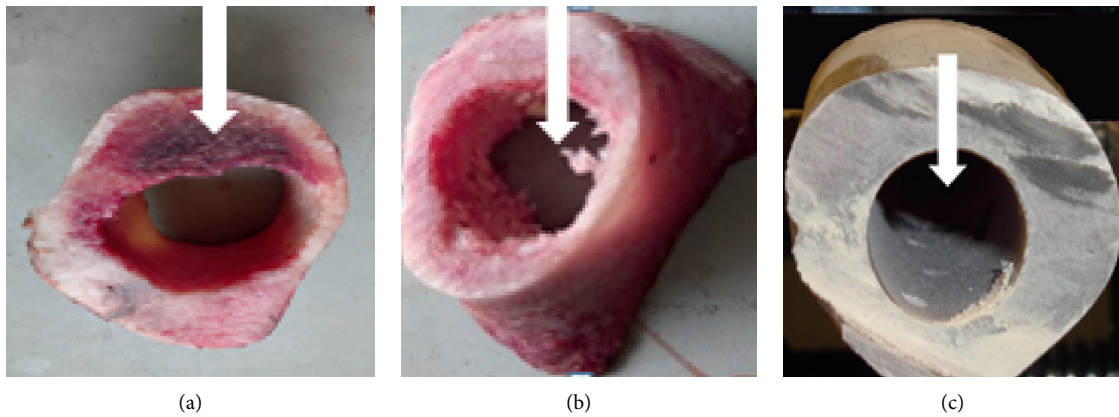


FIGURE 2: Cross-sectional views of (a) bovine, (b) porcine, and (c) artificial femoral samples.

TABLE 1: Prior bone fracture mechanics properties test and values according to [21, 22].

Bone type	Shear strength (Mpa)	K_C (Mpa m ^{1/2})	Specific heat (J/kg K)	Energy required	Speed	Test-type
Bovine bone	65–71	3.21	2.58	$G_{JC} = 1.4-2.6$	Slow	SENT
Human bone	82	2.4–5.3	1150	–	Slow	CT
Pig bone	75	–	1330	–	Slow	CT

TABLE 2: Drilling parameters.

Machine speed (rpm)	Drill diameter (mm)	Feed (mm/min)	Depth of cut (mm)	Point angle (°)
1000, 1500	2.5	Set at 110 mm/min	Set at 6 mm for all	118

TABLE 3: Specimen parameters.

Specimens	Bovine	Porcine	Artificial femur
Density	1.193 g/cm ³	1.013 g/cm ³	1.86 g/cm ³
Marrow diameter	32.45 mm	12.05 mm	18 mm
Bone thickness	5.5 mm	5.68 mm	5.91 mm
Specimen length	34 mm	22 mm	35 mm

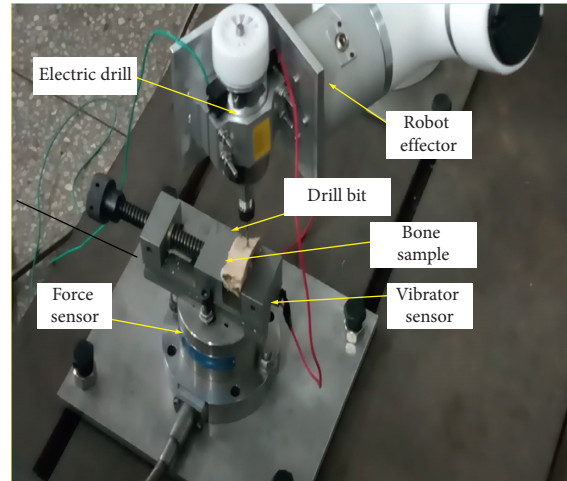


FIGURE 3: The bone drilling procedure using the 6dof Hans Robot.

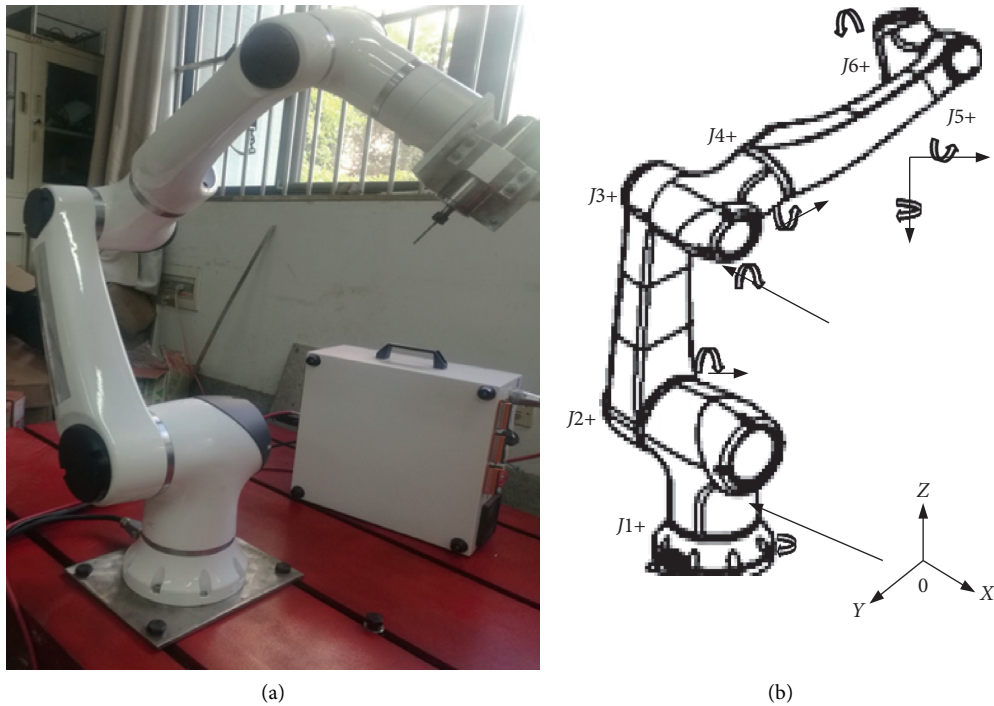


FIGURE 4: Hans Robot model HREF 01-LD010-1000-SI.

2.5.1. Jacobian Matrix. This matrix $J(q)$ of robot is used to determine the relationship between the joint rotation Δq and end effector motion ΔX [28]. The relationship of the robot actuator motion and force exerted on the specimen to be drilled can be obtained as follows:

$$\Delta X = J(q)\Delta q, \quad (1)$$

where $J(q)$ can also be expressed as representing 6×1 (external forces vector) on the manipulator end-point.

$$J_{i,j}(q) = \frac{\partial X_i(q)}{\partial q_j}, \quad (i, j = 1, 2, \dots, 6), \quad (2)$$

and the relationship between joint torques and counter actuator forces/torques to stabilize the external force is illustrated as

$$T = J^T(q)F, \quad (3)$$

where $\tau = (\tau_1, \tau_2, \tau_3, \tau_4, \tau_5, \tau_6)$ represent the 6×1 vector of the torques needed to balance the external force during bone drilling. $F = (F_x, F_y, F_z, \tau_{yz}, \tau_{xz}, \tau_{xy})$.

2.5.2. Stiffness Model. The end deflection ΔX on the effector caused by external force can be calculated by [29]:

$$F = K_m \Delta X, \quad (4)$$

where the angular rotation of the joint is given as

$$\tau = K_m \Delta X, \quad (5)$$

where K_m is the Cartesian stiffness of the effector manipulator and K_θ represents the joint stiffness. However, the partial differentiation of equation (3) with respect to q results in

$$\frac{\delta \tau}{\delta q} = \frac{\delta J^T}{\delta q} F + J^T \frac{\delta F}{\delta X(q)} \frac{\delta X(q)}{\delta q}. \quad (6)$$

By replacing equation (5), the equation of the joint stiffness can then be summarily written as

$$K_\theta = K_c + J^T K_m J. \quad (7)$$

It must be noted that $K_c = \delta J^T / \delta q F$ is the complementary stiffness of the robot effector due to loading or cutting force as a result of drilling, as stated by Claire Dumas [29], which can then be rewritten as

$$K_m = J^{-T} K_m J^{-1}. \quad (8)$$

This summarily equals to

$$\begin{bmatrix} K_{m11} & \cdots & K_{m16} \\ \vdots & \ddots & \vdots \\ K_{m61} & \cdots & K_{m61} \end{bmatrix}, \quad (9)$$

where K_m is the joint stiffness matrix.

$\Delta \theta$ is the model for dynamic manipulator effector stiffness of the robot effector. By further analysis, the stiffness of the effector manipulator can also be remodeled as [30]

$$K_c = \begin{bmatrix} \frac{\delta J^T}{\delta \theta_1} F & \frac{\delta J^T}{\delta \theta_2} F & \frac{\delta J^T}{\delta \theta_3} F & \frac{\delta J^T}{\delta \theta_4} F & \frac{\delta J^T}{\delta \theta_5} F & \frac{\delta J^T}{\delta \theta_6} F \end{bmatrix}. \quad (10)$$

Assuming $(\delta J^T / \delta \theta_1 n F)$ is a 6×1 column vector, then drilling force on the robot effector is $F = [F_x, F_y, F_z]^T$ and that resulted in deflection during drilling is $\Delta X = [\delta x, \delta y, \delta z]^T$, by substituting equation (6) into equation (3), we obtained

$$\Delta X = K_X^{-1} F = g(\theta, K_{\theta_i}, F). \quad (11)$$

The relationship above represents a little deflection of the effector during bone specimen drilling as shown in the experimental set-up in Figure 5. Therefore, joint stiffness K_θ can be written as combinations of stiffness of servo motor K_d , gear shaft K_j , and harmonic reducer K_c of the effector. Figure 6 shows the schematic diagram of the kinematic chains representation of the Hans Robot used for this experiment.

$$\frac{1}{K_\theta} = \frac{1}{K_d} + \frac{1}{K_j} + \frac{1}{K_c}. \quad (12)$$

With reference to K_θ , the stiffness matrix varies as drilling changes, this can be mathematically summarized as

$$\sum = \sum_{i=1}^6 k_{ii} + \sum_{i=1, j=1}^6 i \neq j / k_{ij}. \quad (13)$$

The inertia cutting force in the direction of acceleration causes unbalance force in the robot system which affects the stiffness and possibly given errors or affects its precision. Table 4 illustrates the robot joint type and components for its manipulations.

2.6. Analysis of the Drilling Force. Force analysis of the 6dof Robot arm is presented as a relationship between the effector, torque (τ_z) of the electric motor, and the force (F_z) generated. Different forces on a twist drill are shown in Figure 7, where F_z is not fully caused by the F_q components of the cutting force (F_{z1}) but partially caused by the impacts force on the cutting chisel edge (F_{z2}). The developed derivatives are dependent on the fact that direct current motor torque is proportional to the motor power, the torque controller of the motor driver has the transfer function $G(s)$ as

$$G(s) = \frac{k_1}{k_1(s) + 1}. \quad (14)$$

From Figure 5, F_{z1} is deduced as

$$F_{z1} = 2 F_q \cos \alpha_p. \quad (15)$$

Here, α_p is the inclination angle of force F_q experienced on the cutting edge of the drill, as shown in Figure 6, which is

$$\alpha_p = 90^\circ - \frac{2\rho}{2}, \quad (16)$$

where 2ρ is the point angle of the drill bit.

Torque effect is a factor of the drill diameter and the amount of drilling force F_p that is on the bone specimen type:

$$\tau_z = \frac{d}{2} F_p. \quad (17)$$

When a more substantial size drill is used, then the motor torque will be higher, which will affect the stiffness of the robot effector and the quality of the hole made.

2.7. Vibration Analysis. The displacement, $y(t)$, caused by the vibrating bone causes displacement, $y_e(t)$, of the vibration meter output attached to the bone as stated by [31] so that the relative displacement $y_{rel}(t)$ is given as follow.:

From the equation of motion,

$$m \ddot{y}_e(t) + c(\dot{y}_e(t) - \dot{y}(t)) - k(y_e(t) - y(t)), \quad (18)$$

where $y(t)$ and $y_e(t)$ are the displacements of the vibrating bone and the mass of the vibrating sensor,

$$m \ddot{y}_{rel}(t) + c \dot{y}_{rel}(t) + k y_{rel}(t) = -m \ddot{y}(t), \quad (19)$$

$$y_{rel}(t) = y_e(t) - y(t), \quad (20)$$

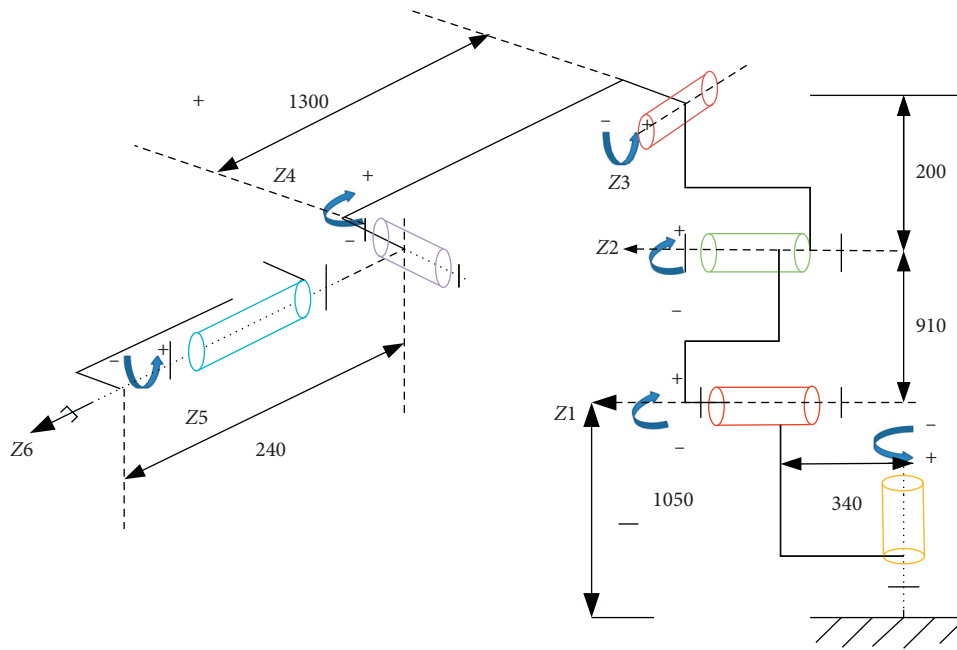


FIGURE 5: Flow chart of drilling trajectory and stiffness evaluation simulation system.

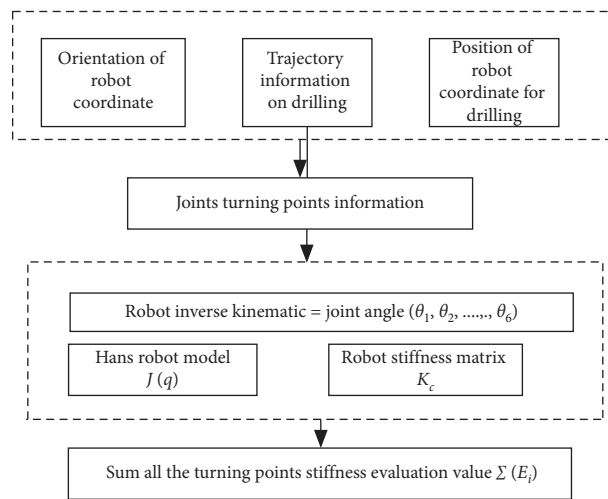


FIGURE 6: Kinematic chains representation of Hans robot HREF 01-LD010-1000-SI.

TABLE 4: Component parts of each joint of 6dof Hans Robot.

Joint	Components
1	Servo motor → gear shaft → harmonic reducer
2	Servo motor → gear shaft → harmonic reducer
3	Servo motor → gear shaft → harmonic reducer
4	Servo motor → gear shaft → harmonic reducer
5	Servo motor → gear shaft → conveyor gear shaft → harmonic reducer
6	Servo motor → gear shaft → conveyor gear shaft → harmonic reducer

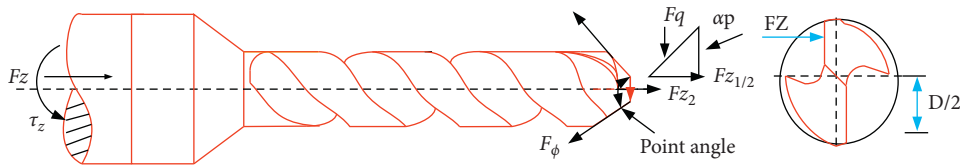


FIGURE 7: Force on twist drill bit during bone drilling of the bone specimen.

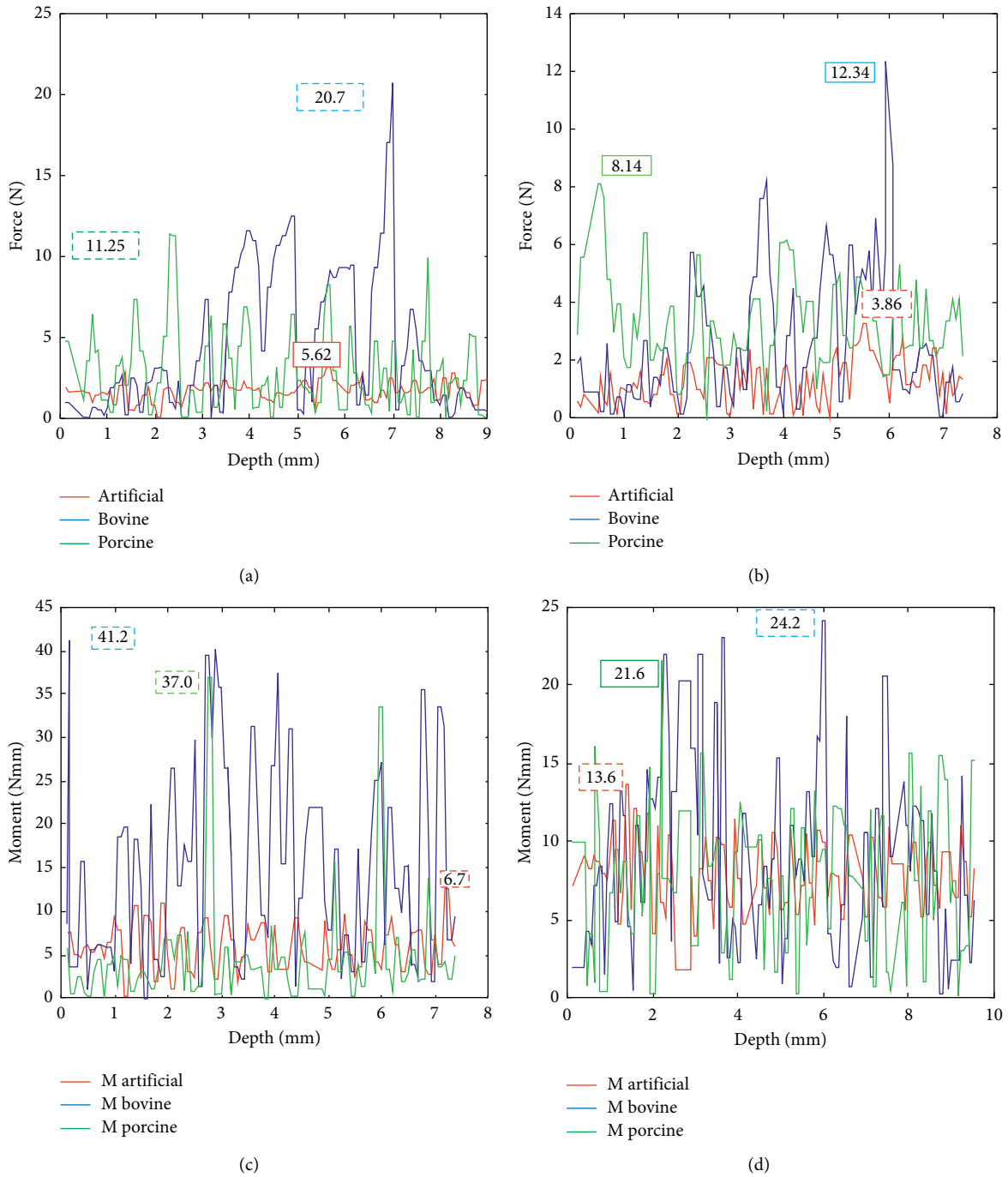


FIGURE 8: Typical data for drilling at a spindle speed of 1000 rev/min to 1500 rev/min for force and torque for bovine, porcine, and artificial femur, respectively. (a) Force at 1500 rev/min vs. depth. (b) Force at 1500 rev/min vs. depth. (c) Torque at 1000 rpm vs. depth. (d) Torque at 1500 rev/min vs. depth.

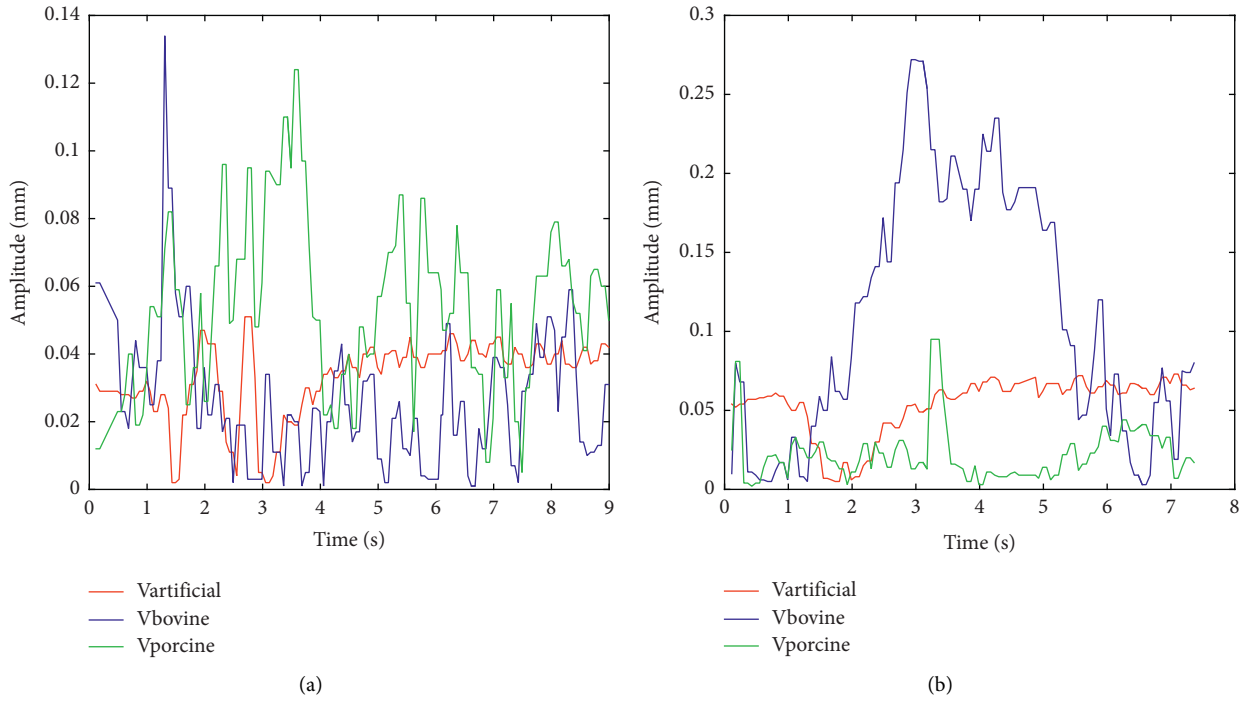


FIGURE 9: Typical vibration data for drilling at a spindle speed of 1000 rev/min to 1500 rev/min for bovine, porcine, and artificial femur, respectively. (a) Torque at 1000 rpm vs. time. (b) Torque at 1500 rev/min vs. time.

where equation (20) is the relative displacement of the vibration sensor mass with respect to the displacement caused by the vibrating bone during drilling. The solution of equation (20) can then be rewritten as

$$y_{rel}(t) = \frac{-m\ddot{y}(t)/k}{\sqrt{\left((1-r^2)^2 + (2\zeta r)^2\right)}} = \frac{r^2 y(t)}{\sqrt{\left((1-r^2)^2 + (2\zeta r)^2\right)}} \quad (21)$$

Assuming the ratio of the frequency,

$$r \frac{\omega}{\omega_n} = \frac{f}{f_n} \ll 1 \approx 0, \quad (22)$$

where f is the frequency of the vibrating bone and f_n is the natural frequency of the sensor attached to the bone. Then, the vibration rate of the bone during drilling is given as

$$y_{rel}(t) = r^2 y(t) = \frac{\omega^2 y(t)}{\omega_n^2}. \quad (23)$$

2.8. Data Analysis. A different set of experiments was conducted to evaluate the drilling force, torque, and vibration resulting on the bone specimens, as shown in Figures 8 and 9, by varying the cutting speed from 1000 rev/min to 1500 rev/min for all the samples with constant feed over

TABLE 5: Variation range of each joint under consideration.

Joint	θ_1	θ_2	θ_3
Range	$0 \sim (\pi/2)$	$0 \sim 2\pi$	$0 \sim 2\pi$

specific interval. All the raw data were processed using Microsoft Office Excel 2010 and normalized with MATLAB 2015b to determine the maximum and minimum forces, torque, and vibration during drilling at the two-set spindle speeds [32]. Table 5 also shows the joint and angular range under consideration.

3. Results

3.1. Maximum Force. At two selected spindle speeds, the result obtained shows that an increase in spindle speed causes a decrease in the average force values on the bovine, artificial femur, and porcine. The following maximum cutting forces of 20.07 N, 5.62 N, and 11.25 N were recorded at 1000 rev/min on each of the specimens as stated: bovine bone, artificial femur, and porcine, respectively. At 1500 rev/min, the maximum cutting force reduced drastically to 12.34 N, 3.86 N, and 8.14 N for bovine bone, artificial femur, and porcine, respectively, as shown in Table 6. This result is amounted to 23.85% (bovine), 22.85% (porcine), and 16% drops (artificial femur), as shown in Figure 8. It was further noted that the bovine bone possessed the highest cutting force which is attributed to its mechanical and material properties.

TABLE 6: Comparison of the present experimental results with prior experimental data for surgical drilling into human and animal bone.

Research type	Type specimen	Type result force (N)
Present	Bovine femur	12.34 to 20.07
Present	Porcine femur	8.14 to 11.25
Present	Artificial femur	3.86 to 5.62
Tsai et al. [33].	Human femoral trochanter (cancellous)	1 to 1.5
Tsai et al. [33].	Human femoral trochanter (cortical)	0 to 50
Powers [12]	Porcine vertebra	0.6 to 29.6
Alams et al. [13]	Bovine femoral shaft	25 to 85
Hillery et al. [34]	Bovine tibial shaft	24 to 48
Lee et al. [35]	Bovine tibial shaft	0 to 20
Troy.MacAvelia et al. [17]	Human femoral shaft	140.2 to 186.3
Troy.MacAvelia et al. [17]	Artificial femoral shaft	67.2 to 53.3
	Torque (N·mm)	
Present	Bovine femur	24.2 to 41.2
Present	Porcine femur	21.6 to 37.0
Present	Artificial femur	6.7 to 13.6
Tsai et al. [33]	Human femoral trochanter (cancellous)	2 to 120
Tsai et al. [33]	Human femoral trochanter (cortical)	0 to 10
Troy.MacAvelia et al. [17]	Human femoral shaft	16.9 to 16.
Troy.MacAvelia et al. [17]	Artificial femoral shaft	42.9 to 8.4
Alams et al. [13]	Bovine femoral shaft	10–23
Allotta et al. [36]	Porcine femoral shaft	55
Hillery et al. [34]	Bovine tibial shaft	10 to 14.5
Lee et al. [35]	Bovine tibial shaft	0 to 38

3.2. Maximum Torque. From the torque data obtained, at increase in the spindle speed from 1000 rpm to 1500 rpm, it gives a continuous drop in the maximum torque obtained from 41.2 N·mm to 24.2 N·mm (bovine), from 37.0 N·mm to 21.6 N·mm (porcine), and from 13.6 N·mm to 6.7 N·mm (artificial), as also indicated in Table 6; all these summarily amounted to 25.99% drop (bovine) and 26.27% drop (porcine), except for the artificial femur which has about 33.99% increase, as illustrated in (Figure 8); this increase may be due to the plasticity of the material composition of the artificial femur.

3.3. Maximum Vibration. At an increase in the spindle speed from 1000 rev/min to 1500 rev/min, the vibration amplitude increases with time by 33.99% for (bovine), 22.48% for (Porcine), and 30.93% for artificial femur, respectively. This indicated that an increase in the spindle speed affects the stiffness of the robot effector thereby increases the vibration rate due to backlash and less stiffness value, as shown in Figure 9; this extensive increase in the vibration of the artificial femur may also be attributed to the effect of temperature gradient on the material composition due to rise in the drilling speed.

3.4. Specimens Quality/Defect Test. A thorough microscopic defect test was conducted on all the bone samples, with no cracks and no necrosis before the test and after, and the drill bit was also checked for excessive or uneven wear.

3.5. Robot Stiffness Effector Simulation. Due to the rotational motion of the end effector, there is a change in stiffness which resulted in deformation difference. Hence, it is important to determine the spatial stiffness of the end effector

while drilling bone specimen and considering optimization of path drilling plan. From equation (9), it is seen that the stiffness values in X and Y directions are affected by rotation of joints 1 to 3, while the stiffness value in Z direction is also related to joints 2 and 3. Primarily, our attention is based on simulation in the Z direction at the effector manipulator joint to stabilize one joint and rotate the other two joints while drilling to observe the effector stiffness. However, Table 5 shows us the range of variations in each joint during the simulation. The spatial behavior of stiffness in the Z direction can be evaluated by changing the value of θ_2 and θ_3 at the effector end while drilling. The stiffness simulation at the robot effector is seen in Figure 10, stiffness in Z direction also causes an increase of θ_3 which leads to a sinusoidal change, as illustrated in Figure 11, and the amplitude of fluctuation is from 2 “N/mm” to 15 “N/mm”. This implies that the phase position and peak value of this sinusoidal change is sensitive to change of θ_2 , as illustrated in Figure 12.

4. Discussion

4.1. Broad Findings. The experimental investigation and analysis showed that maximum forces were obtained at a spindle speed of 1000 rev/min and substantially dropped when the speed increased to 1500 rev/min. These indicated that the lower the speed, the higher the cutting force and the higher the chance of complications such as tool breakage or microcracks on the bone. On the contrary, an increase in speed reduced the torque as seen on all the samples. From earlier data obtained, the graph in Figure 8 shows that both animal and artificial femurs give a substantial rise in the force on the drill bit entering the bone. This is similar to the force and torque fluctuation response pattern as reported by Lee et al. [13, 35, 37]. For the changes at the spindle speed

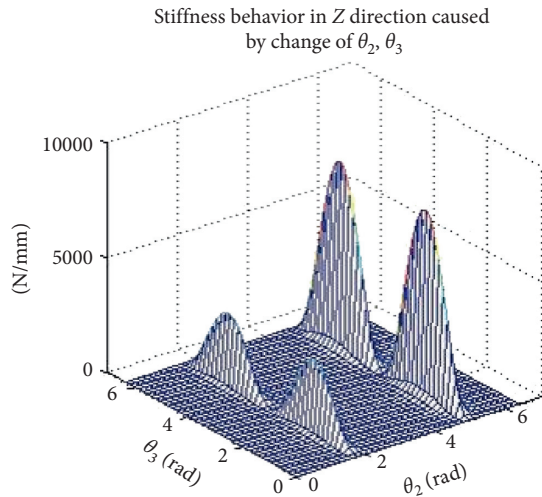


FIGURE 10: Robot effector stiffness in Z direction caused by change from θ_2 to θ_3 .

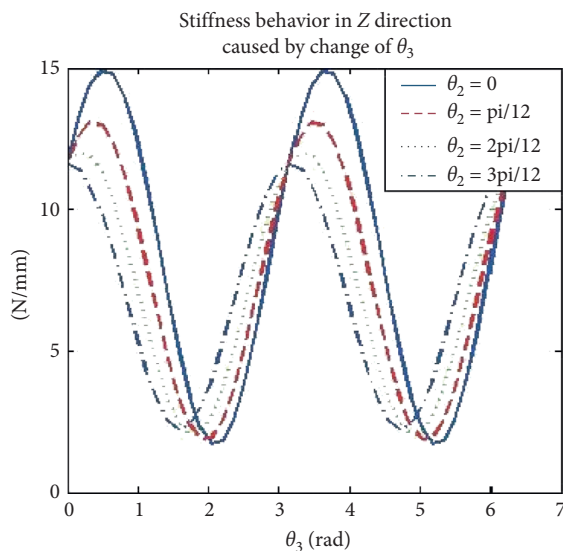


FIGURE 11: Robot effector stiffness in Z direction caused by change of θ_3 .

from 1000 rev/min to 1500 rev/min, there is a significant drop in the average values of maximum drilling force for all the bone specimens with a drop from 20.07 to 12.34 N, approximately 23.85% for bovine, (11.25 to 8.14 N) with 16.03% for Porcine, and (3.86 to 5.62 N) with 33.99% for artificial femur. The maximum average values of torque also decrease from 41.2 to 24.2 N·mm (bovine), 37.0 to 21.6 N·mm (porcine), and 13.6 to 6.7 N·mm (artificial femur), respectively which is close to the result obtained by [13, 36, 38]. At an increase in the spindle speed from 1000 rev/min to 1500 rev/min, it increases the vibration amplitude with time by 33.99% for bovine, 22.48% for porcine, and 30.93% for artificial femur, respectively. This indicated that an increase in the spindle speed affects the

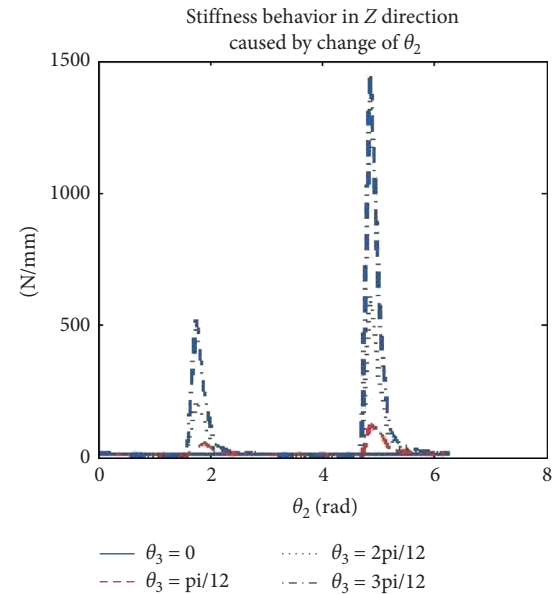


FIGURE 12: Stiffness behaviors in Z direction by change of θ_2 .

stiffness of the robot effector thereby increases the vibration rate, as shown in Figure 9. An increase in the spindle speed from 1000 rev/min to 1500 rev/min increases the rate of depth of cut and reduces the time of cut in all the samples, although the rate of cut also depends on the materials properties of each specimen. The depth of cut in the artificial femur is greatly influenced by increase in speed due to temperature rise on the drill bit which influenced the plasticity behavior of its chemical and materials composition. Generally, the unstable cutting force and torque obtained while drilling can be attributed to the low stiffness of the robot effector; this gives space for a little backlash and vibration during drilling. These results, however, showed a significant variance in the force-torque relationship with the bovine, artificial femur, and porcine and are also used to compare similarities in their parameters and properties which could make them as an experimental substitute to human bone. Force result obtained from the bovine femur is close to the range of findings of Lee et al. [35] which confirms a similarity in the properties of the human bone. From the simulation, the stiffness in Z direction can be evaluated by changing the value of θ_2 and θ_3 at the effector end while drilling; also, a little increase of θ_3 could lead to vibration or an unstable effector manipulator during drilling. All the results obtained when compared with prior studies revealed that the robot stiffness has impending effects on the force, torque, and vibration of the bone during drilling.

5. Conclusion

A comparative study carried out revealed that both porcine and artificial femur samples have different forces and torques response at a different cutting speed, which are not within the specified range of cutting force and torque applicable for drilling human bone with an exception of bovine bone which has the force range close to the reported finding by [17]. These variances revealed that there is possibly

remarkable change in the material properties of both porcine and artificial femur and cannot be a good substitute for human bone unlike bovine for experimental purposes. However, this simulation addressed the effect and behavior of joint rotation on end effector stiffness during bone drilling. The simulation results also show serious mutations during the joint rotation and a sharp peak end curve was generated. Our findings are limited to effector stiffness only, considering all joints will be too complex and out of focus in this study; however, the result evaluated can be regarded as a reference to later research on robot stiffness. To the best of our knowledge, no experiment was done using the 6dof Robot effector to evaluate and compare forces, torques, and vibration in bovine, porcine, and artificial femur drilling, taking into considerations of the stiffness of the effector joint, making this study to be used as a benchmark for further experimental and analytical research on drilling bones for proper orthopedic procedures.

Data Availability

The data used to support the findings of this study are available from the corresponding author upon request.

Conflicts of Interest

The authors declare that there are no conflicts of interest.

Acknowledgments

This research was supported by the National Natural Science Foundation of People Republic of China under Grant 51575100.

References

- [1] O. A. Orelaja, "Vibration reduction, characterization of drill bit and femur bone to forces during robotic-assisted drilling using model soft fixture embedded with pressurized-air damper," in *Proceedings of the International Conference on Intelligent Informatics and Biomedical Sciences (ICIIBMS)*, Shanghai, China, November 2019.
- [2] O. A. Orelaja, W. Xingsong, M. Kaiwei, Z. Tianzheng, S. I. Dauda, and S. Umer, "Experimental investigation of relationship between cutting force, vibration frequency and temperature gradient during robotic assisted bone drilling," in *Proceedings of the International Conference Of Industrial Engineering And Application ICIEA 2020*, ICIEA, Tokyo, Japan, 2020.
- [3] J. Lee, Y. Rabin, and O. B. Ozdoganlar, "A new thermal model for bone drilling with applications to orthopaedic surgery," *Medical Engineering & Physics*, vol. 33, no. 10, pp. 1234–1244, 2011.
- [4] E. Shakouri, H. S. Mohammad, M. Mehdi, and S. Shaghayegh, "Experimental and analytical investigation of the thermal necrosis in high-speed drilling of bone," *Proc IMechE Part H: Journal of Engineering in Medicine*, vol. 228, no. 3, pp. 330–341, 2014.
- [5] J. D. Currey, "Effects of differences in mineralization on the mechanical properties of bone," *Philosophical Transactions of The Royal Society Of London Series B-Biological Sciences*, vol. 304, no. 1121, pp. 509–518, 1984.
- [6] BTS, "Bureau of transportation statistics annual report," 2007, <http://www.bts.gov>.
- [7] A. Gupta and K. M. Tse, "Finite element analysis on vibration modes of femur bone," in *Proceedings of the International Conference on Advances in Mechanical Engineering Aetame*, Zhengzhou, China, 2013.
- [8] A. Bertelsen, J. Melo, E. Sánchez, and D. Borro, "A review of surgical robots for spinal interventions," *The International Journal of Medical Robotics and Computer Assisted Surgery*, vol. 9, no. 4, pp. 407–422, 2013.
- [9] R. Jacob, L. Mitchell, S. Mika, and H. Blake, "Developing a surgical robot from a concept to a transatlantic teleoperation experiment," "Developing a surgical robot from a concept to a transatlantic teleoperation experiment," in *Surgical Robotics-Systems Applications and Visions*, B. H. Jacob Rosen and R. M. Satava, Eds., pp. 159–198, Springer Science and Business Media, New York, NY, USA, 2011.
- [10] U. Hirt, J. A. Auer, and S. M. Perren, "Drill bit failure without implant involvement - an intraoperative complication in orthopaedic surgery," *Injury*, vol. 23, pp. S5–S16, 1992.
- [11] N. Sugita and M. Mitsuishi, "Specifications for machining the bovine cortical bone in relation to its microstructure," *Journal of Biomechanics*, vol. 42, no. 16, pp. 2826–2829, 2009.
- [12] M. J. Powers, "The mechanics of bone drilling:experiments and finite predictions," Ph.D thesis, University of Calary, Calgary, Canada, 2006.
- [13] K. Alam, A. V. Mitrofanov, and V. V. Silberschmidt, "Finite element analysis of forces of plane cutting of cortical bone," *Computational Materials Science*, vol. 46, no. 3, pp. 738–743, 2009.
- [14] T. Karalis and P. Galanos, "Research on the mechanical impedance of human bone by a drilling test," *Journal of Biomechanics*, vol. 15, no. 8, pp. 561–581, 1982.
- [15] K. Branko and V. Miomir, "Calibration and accuracy of manipulation robot models—an overview," *Mechanism and Machine Theory*, vol. 29, no. 3, pp. 479–500, 1994.
- [16] G. Poumarat and P. Squire, "Comparison of mechanical properties of human, bovine bone and a new processed bone xenograft," *Biomaterials*, vol. 14, no. 5, pp. 337–340, 1993.
- [17] T. MacAvelia, A. Ghasemipoor, and F. Janabi-Sharifi, "Force and torque modelling of drilling simulation for orthopaedic surgery," *Computer Methods in Biomechanics and Biomedical Engineering*, vol. 17, no. 12, pp. 1285–1294, 2012.
- [18] K. Yu, S. Iwata, K. Ohnishi, S. Usuda, T. Nakagawa, and H. Kawana, "Modeling and experimentation of drilling vibration for implant cutting force presenting system," in *Proceedings of the IEEE International Workshop on Advanced Motion Control (AMC)*, IEEE, Yokohama, Japan, pp. 711–771, 2014.
- [19] T. MacAvelia, M. Salahi, M. Olsen et al., "Biomechanical measurements of surgical drilling force and torque in human versus artificial femurs," *Journal of Biomechanical Engineering*, vol. 134, no. 12, pp. 124503–124509, 2012.
- [20] C. H. Yonghua and F. H. Dong, "Robot machining recent development and future research issues," *International Journal of Advanced Manufacturing Technology*, vol. 66, no. 9–12, pp. 1489–1497, 2013.
- [21] H. A. R. Yuehuei, *A Draughn Mechanical Testing of Bone and the Bone-Implant Interface*, pp. 69–72, CRC Press, Boca Raton, FL, USA, 1999.
- [22] H. L. Chen and A. A. Gundjian, "Specific heat of bone," *Medical & Biological Engineering*, vol. 14, no. 5, pp. 548–550, 1976.

- [23] M. D. O'Toole, K. Bouazza-Marouf, D. Kerr, M. Gooroochurn, and M. Vloeberghs, "A methodology for design and appraisal of surgical robotic systems," *Robotica*, vol. 28, no. 2, pp. 297–310, 2009.
- [24] G. Paula, "Surgical robotics: reviewing the past, analysing the present, imagining the future," *Robotics and Computer-Integrating Manufacturing*, vol. 27, pp. 261–266, 2011.
- [25] J. Lee, S. J. Huh, and H. J. Lee, "Experimental determination of thermal conductivity of cortical bone by compensating heat loss in parallel plate method," *International Journal of Precision Engineering and Manufacturing*, vol. 19, no. 4, pp. 569–576, 2018.
- [26] G. Alici and R. W. Daniel, "Static friction effects during hard-on-hard contact tasks and their implications for manipulator design," *The International Journal of Robotics Research*, vol. 13, no. 6, pp. 508–520, 1994.
- [27] H. Bruyninckx and J. De Schutter, "Specification of force-controlled actions in the task frame formalism-a synthesis," *IEEE Transactions on Robotics and Automation*, vol. 12, no. 4, pp. 581–589, 1996.
- [28] R. T. Frankle, "Nutrition education in the medical school curriculum: a proposal for action: a curriculum design," *The American Journal of Clinical Nutrition*, vol. 29, no. 1, p. 15, 1976.
- [29] G. Alici and B. Shirinzadeh, "Enhanced stiffness modeling, identification and characterization for robot manipulators," *IEEE Transactions on Robotics*, vol. 21, no. 4, pp. 554–564, 2005.
- [30] J. Frank, B. Gritzbach, C. Winter, B. Maier, and I. Marzi, "Computer-assisted femur fracture reduction," *European Journal of Trauma and Emergency Surgery*, vol. 36, no. 2, pp. 151–156, 2010.
- [31] K. S. Jyoti, *Vibration Analysis, Instruments, and Signal Processing*, CRC Press Taylor & Francis Group, LLC, Boca Raton, FL, USA, 2015.
- [32] N. Bertollo and W. Walsh, "Drilling of bone: practicality, limitations and complications associated with surgical drill-bits," "Drilling of bone: practicality, limitations and complications associated with surgical drill-bits," in *Biomechanics Application*, V. Klika, Ed., , pp. 1–32, InTech, 2011.
- [33] M.-D. Tsai, M.-S. Hsieh, and C.-H. Tsai, "Bone drilling haptic interaction for orthopedic surgical simulator," *Computers in Biology and Medicine*, vol. 37, no. 12, pp. 1709–1718, 2007.
- [34] M. T. Hillery and I. Shuaib, "Temperature effects in the drilling of human and bovine bone," *Journal of Materials Processing Technology*, vol. 92-93, pp. 302–308, 1999.
- [35] J. Lee, B. A. Gozen, O. Arda, and O. B. Ozdoganlar, "Modeling and experimentation of bone drilling forces," *Journal of Biomechanics*, vol. 45, no. 6, pp. 1076–1083, 2012.
- [36] B. Allotta, G. Giacalone, and L. Rinaldi, "A hand-held drilling tool for orthopedic surgery," *IEEE/ASME Transactions on Mechatronics*, vol. 2, no. 4, pp. 218–229, 1997.
- [37] M. J. Powers, *The Mechanics of Bone Drilling: Experiments and Finite Predictions*, University of Calgary, Calgary, Canada, 2006.
- [38] M. S. Troy MacAvelia, M. Olsen, M. Crookshank, and H. Emil, "Schemitsch, ahmad ghasempoor, farrokh janabi-sharifi and rad zdero, biomechanical measurements of surgical drilling force and torque in human versus artificial femurs," *Journal of Biomechanical Engineering*, vol. 134, no. 12, Article ID 124503, 2012.

Research Article

Automatic Detection of Brain Tumor on Computed Tomography Images for Patients in the Intensive Care Unit

Fahmi Fahmi ¹, Fitri Apriyulida,¹ Irina Kemala Nasution,² and Sawaluddin³

¹Department of Electrical Engineering, Faculty of Engineering, Universitas Sumatera Utara, Medan, Indonesia

²Department of Neurology, Faculty of Medicine, Universitas Sumatera Utara, Medan, Indonesia

³Faculty of Computer Science and Information Technology, Universitas Sumatera Utara, Medan, Indonesia

Correspondence should be addressed to Fahmi Fahmi; fahmimn@gmail.com

Received 12 September 2019; Revised 1 June 2020; Accepted 24 June 2020; Published 15 July 2020

Academic Editor: Ahmed F. Hussein

Copyright © 2020 Fahmi Fahmi et al. This is an open access article distributed under the Creative Commons Attribution License, which permits unrestricted use, distribution, and reproduction in any medium, provided the original work is properly cited.

Patients in the intensive care unit require fast and efficient handling, including in-diagnosis service. The objectives of this study are to produce a computer-aided system so that it can help radiologists to classify the types of brain tumors suffered by patients quickly and accurately; to build applications that can determine the location of brain tumors from CT scan images; and to get the results of the analysis of the system design. The combination of the zoning algorithm with Learning Vector Quantization can increase the speed of computing and can classify normal and abnormal brains with an average accuracy of 85%.

1. Introduction

Patients in the intensive care unit require fast and efficient handling, including in-diagnosis service. The development of technological systems in the medical world is now proliferating. Many applications have been built that can process medical image results from modalities such as Computed Tomography (CT), Magnetic Resonance Imaging (MRI), Positron Emission Tomography (PET), and X-ray systems [1]. In the medical world, CT scans are widely used to support the diagnosis of a disease that can display body tissue without the need to go through surgery.

Detection of brain tumors has an essential role in the field of biomedical application in terms of diagnosis of medical image records. The importance of identifying brain tumors has increased in the recent years. The brain tumor classification was developed to help medical staff diagnose the disease. In the classification, there are several processes that need to be performed, e.g., preprocessing, feature extraction, and classification. Preprocessing is part of processing an image before feature extraction is performed to determine an area or object. This process consists of filtering, normalizing, and identifying objects before the extraction stage. Feature extraction is a step to take the core value

(feature) on a CT-scan image to get an object that will be recognized or distinguished from other objects [2]. The extraction features include using the Gray Level Co-Occurrence Matrix (GLCM) with a matrix size of 64×64 pixels [3], with discrete wavelet transform applying Principal Component Analysis (PCA) [4] or zoning method [5].

Classification is the process of determining functions that can distinguish concepts with the aim of estimating the unknown class of an object [6]. One method that can be used in the classification is Learning Vector Quantization (LVQ). LVQ is a classification method that can conduct training at supervised layers of a version of the Kohonen model that has a simple learning algorithm consisting of one input and output layer [7].

The following are several studies that have been previously conducted in the area of brain tumors, including the classification of soft tissues within brain CT scan based on wavelet-dominant gray level run length texture features [8]. This study obtained standard brain accuracy and brain tumor identification of 98.00%. Classification of brain tumors based on the statistical feature set uses the support vector machine with an accuracy of 68.1% [9].

In this study, we used feature extraction with zoning and classification methods with Learning Vector Quantization

(LVQ) techniques. For each sample data that has gone through the image preprocessing process and feature extraction, and tumor location will be determined.

The objectives are to produce a computer-aided system so that it can help radiologists to classify the types of brain tumors suffered by patients quickly and accurately; to build applications that can determine the location of brain tumors from CT scan images, and to get the results of the analysis of the system design. The benefits obtained from this study are to help radiologists to diagnose the types of brain tumors suffered by patients quickly and accurately, especially patients in the intensive care unit, and also, it becomes one of the references for researchers who focus on computer vision technology in the medical field.

2. Materials and Methods

2.1. Brain Tumors. The brain tumor is tissue mass that grows uncontrollably and is suppressing other healthy tissue. Brain tumors can be classified as benign (soft) brain tumors and malignant (severe) brain tumors. It is clinically challenging to distinguish between benign or malignant brain tumors because the symptoms that arise are also determined by the location of the tumor, the rate of growth, and the effect of the tumor mass on brain tissue [10].

Initial diagnosis is made by obtaining data on the patient's family health history and physical examination. After that, a neurological examination is performed to determine the mental status, memory, cranial nerve function, muscle strength, and response to pain. The next step is a radiological examination through CT-scan or MRI (Magnetic Resonance Imaging).

2.2. Computed Tomography. Computed Tomography (CT) scan is a method used to examine patients without direct surgery but uses X-ray and a computer to produce brain images in axial fragments [11]. The number of pieces produced by the CT-scan is determined by the specifications of the CT-scan used. In order to improve the quality of the image in the radiological examination, the patient is sometimes injected with a contrast agent in order to improve the image quality of the desired organ. The size of the images contained on the CT-scan ranges from -1024 to $+3071$ on the Hounsfield unit scale. Hounsfield itself is a measurement of the density of the tissue, as shown in Figures 1 and 2.

Image processing is a method for processing and analyzing images so as to produce images in accordance with image perceptions and needs to be used using computer aids. The image can be interpreted as a function that has two dimensions $f(x, y)$, where x and y are coordinates and f at each point (x, y) expresses the intensity, brightness, and grayscale in the image. The digital image is the study of a matrix in which there are elements of an image that can provide information in a discrete form. Digital images are continuous as in X-ray and television monitors. Thus, the conversion process needs to be performed to get information from the required digital image. To get feature information on images, various applications can be used, one of which is

computer vision, which has been developed in the process of taking image information in the form of features that have been extracted automatically from the image itself. This process is often used to combine several technologies such as image and signal processing, pattern recognition and multimedia, and interaction between humans and computers. This process is often referred to as CBIR (Content-Based Image) in the field of image processing [12].

Some stages contained in the CBIR process include the following:

- (1) Preprocessing aims to determine an object that will be used at the extraction stage
- (2) Feature Extraction is a process for obtaining new features in the form of patterns, shapes, and textures

2.3. Forming a Binary Matrix (Binarization). At this stage, the image will be formed as black and white by converting a gray-level image to a binary image. This process will take the average value of each RGB value, where the pixel value produced is higher than the threshold value, it will be represented as white and if the resulting pixel value is less than the threshold value, it will be represented as black [13]. The thresholding process is used to determine the degree of the gray level in the image and determine the threshold value. The process for determining this threshold value uses the following equation:

$$T = \frac{f_{maks} + f_{min}}{2}, \quad (1)$$

where T = threshold value, f_{maks} = maximum pixel value, and f_{min} = minimum pixel value.

2.4. Feature Selection. Feature selection is the process of determining patterns by obtaining values on image characters to form feature values. Classification uses feature values to recognize input units from output units so that they can easily distinguish objects.

2.5. Zoning Method. The zoning method is a method of feature extraction that can divide the characters into $N \times M$ zones from each zone. The feature value calculation is performed to form the feature values in the $M \times N$ zone. In the classification process, the introduction of the zoning method produces proper and efficient feature extraction. Zoning can be used to calculate the number of white pixel values in a particular zone; the value obtained from the zoning process will be used as a value for the vector input. The results of the zoning process are vector features that can be entered into the classification stage, as in Figure 3 [14].

2.6. Definition of LVQ (Learning Vector Quantization). LVQ is a classification method that can conduct training at supervised layers at the competitive layer. This layer is able to classify the given vector input automatically. Some input vectors have close weights; therefore, the weights will connect the input layer with the competitive layer. The

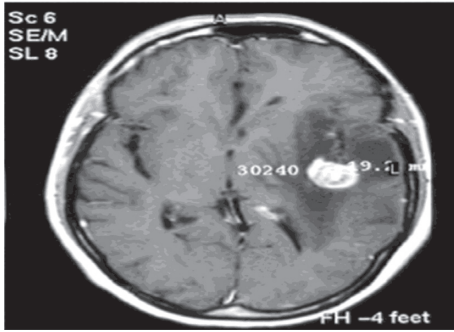


FIGURE 1: Brain tumor on CT-scan [12].

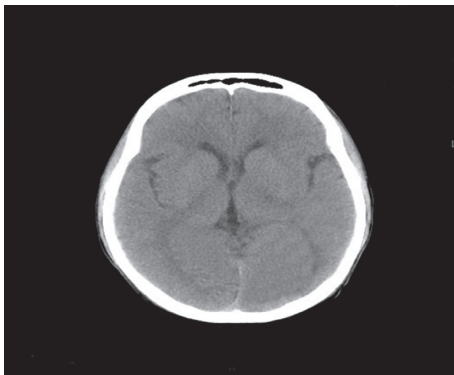


FIGURE 2: Normal brain on CT-scan.

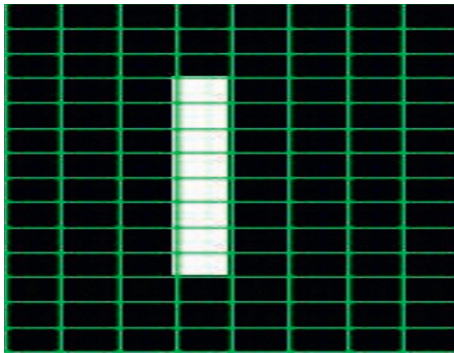


FIGURE 3: Zoning method.

competitive layer produces a class that is connected to the output layer with an activation function. The architecture of an LVQ network with several input layer units and units at the output layer can be seen in Figure 4 [16].

Figure 4 explains that the values X_1 to X_2 are input values where this value will be used for the training process and testing process. W_1 and W_2 as weight vectors that can connect each input layer with the output layer. W_1 and W_n are used to get the smallest weight distance from the weight vector obtained from the calculation of input values. E_1 and E_2 are used as the output layer to represent several classes, while D_1 and D_2 are used as the output values at the output layer for the testing process.

Some of the advantages of LVQ are as follows [16, 17]:

- (1) Able to produce a minimum error value

- (2) At the classification, the stage can summarize large data sets into small vectors
- (3) Can do a gradual renewal of the resulting model

The disadvantages of LVQ are as follows:

- (1) To determine the distance to all attributes, an accurate calculation must be used.
- (2) Calculation of initialization and parameters are needed in determining the accuracy of the LVQ model.
- (3) There is difficulty in determining the number of vectors in new problems before entering into the classification process using the LVQ method, the training process is first carried to simplify the process of class searching so that it can perform an introduction of input patterns based on the output obtained. LVQ can perform input pattern recognition if the distance between the weight vector and the input vector is close together.

2.7. Training and Testing. At LVQ, there are two stages of training and testing as follows: the training algorithm and testing of the LVQ artificial neural network used for the training and testing process. The initial weight of the input values X_1 to X_n towards the output layer that represents the whole class, maximum epoch (MaxEpoch), learning rate parameters (α), reduction of learning rate (Deca), and minimum error (Eps) is determined.

At the training stage, LVQ calculation results are used to get the weight value that will be stored and used in the testing phase. In the testing phase, new input data is classified by calculating the value of each weight in the input and selecting the smallest distance in the two weights that have been stored. The value at the smallest weight distance will represent the class in the input image.

The data used are 40 data stored in the medical record of H. Adam Malik General Hospital in patients aged 40 to 60 years with male sex 60% and female 40%, all anonymized.

2.8. Input of the Brain Image. The image input process is carried out before the image classification process. The image data used in this study is axial piece brain image data obtained from CT Scan. The image used is a grayscale image measuring 512×512 .

2.9. Preprocessing. At the preprocessing stage shown in Figure 5, several stages are carried out to facilitate the next process; the preprocessing stage consists of grayscale and binarization processes. At the stage of binarization, the image is converted into a grayscale form, and then, thresholding will be performed where the grayscale image will be converted into a binary form, which has values 1 and 0 (white and black). In this stage, the threshold value is used to determine the binary value in each image. If the resulting value is above the threshold value, the pixel value is changed to white; if the resulting value is less than the threshold, the pixel value will be changed to black. This is shown in Figure 6.

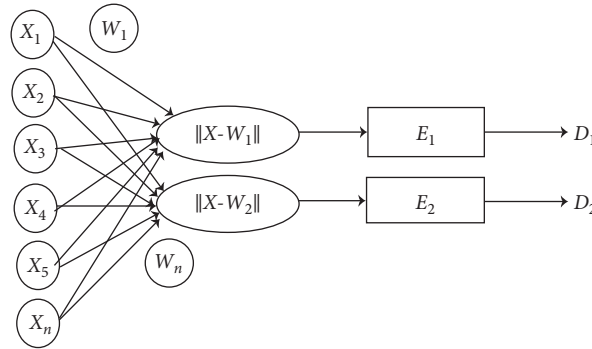


FIGURE 4: LVQ network architecture [15].

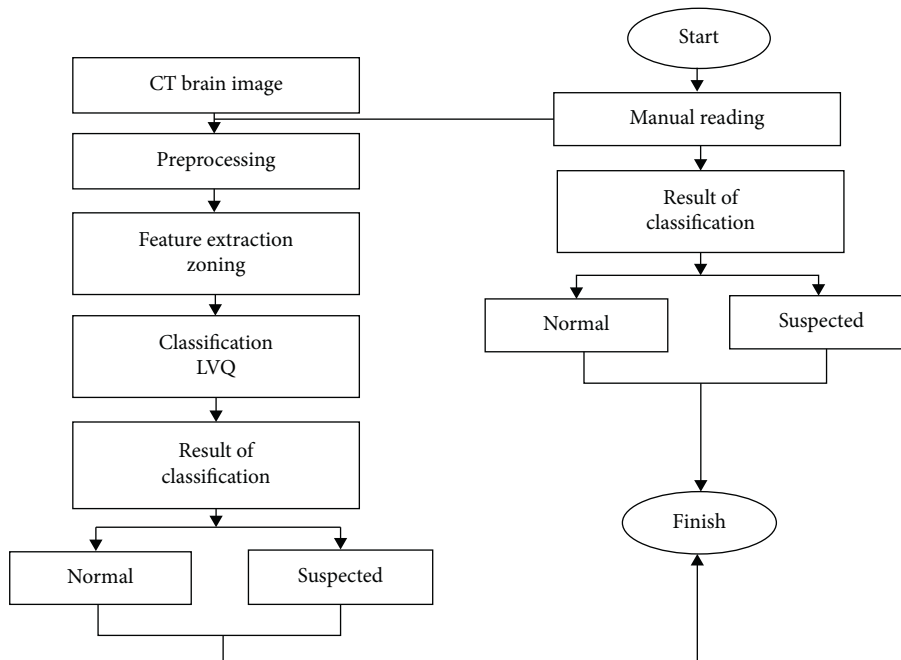


FIGURE 5: Research flowchart.

2.10. *Feature Extraction.* In the next process, after going through the preprocessing, the feature extraction step is carried out by the zoning method to get a good feature value on the image of a brain tumor. Furthermore, the feature values obtained from the method will be classified using the LVQ (learning vector quantization) method.

Zoning is one method that can divide several regions, where each region will produce a feature value by counting the highest number of white pixels. At this stage, the image size of 512×512 will be divided into 8 columns and 8 rows so that it gets 64 zones, and there are 64 feature values in it. The following process of extraction features can be seen in Figure 7, while the division of zones can be seen in Figure 8.

The process of the zoning method on CT brain image tumors is as follows:

- (1) The number of white pixels are counted per zone from Z_1 to Z_{512}

- (2) It is determined which zone has the highest number of white pixels
- (3) The feature values (Z_n) of each zone are calculated from Z_1 to Z_{512}

The following formula is used:

$$Z_n = \frac{Z_n}{Z_{\text{highest}}}, \quad (2)$$

where $1 \leq n \leq 512$.

Feature values (Z_n) are obtained by comparing the number of white pixels from one zone with the zones obtained from process no 2. Examples of zoning method calculations are as follows:

- (1) The number of white pixels in each zone is $Z_4 = 40, Z_{12} = 30, Z_{40} = 70,$ and $Z_{53} = 50$

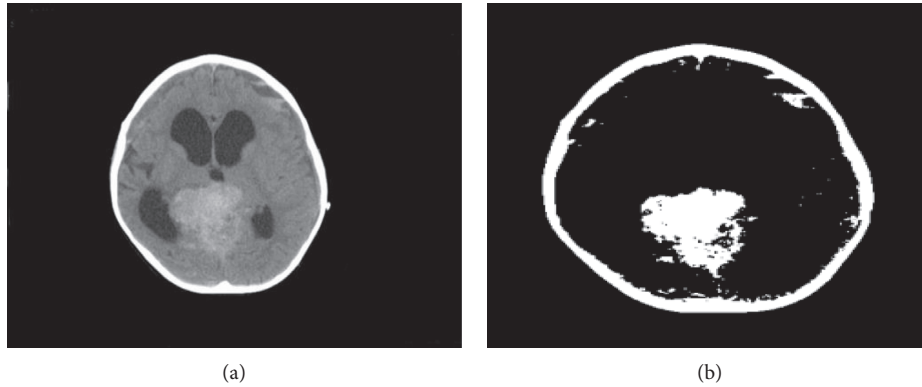


FIGURE 6: Binarization, normal (a) and after binarization (b).

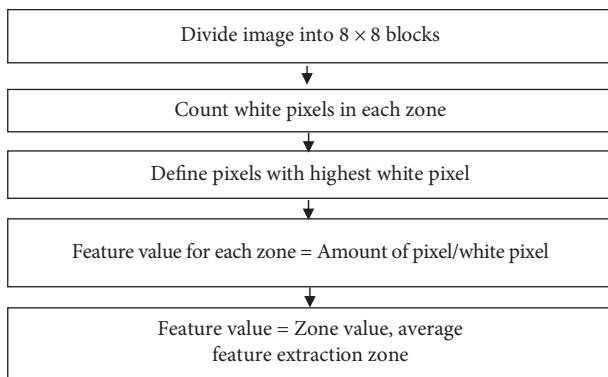


FIGURE 7: Feature extraction process.

8 columns →							
Z1	Z2	Z3	Z4	Z5	Z6	Z7	Z8
Z9	Z10	Z11	Z12	Z13	Z14	Z15	Z16
Z17	Z18	Z19	Z20	Z21	Z22	Z23	Z24
Z25	Z26	Z27	Z28	Z29	Z30	Z31	Z32
Z33	Z34	Z35	Z36	Z37	Z38	Z39	Z40
Z41	Z42	Z43	Z44	Z45	Z46	Z47	Z48
Z49	Z50	Z51	Z52	Z53	Z54	Z55	Z56
Z57	Z58	Z59	Z60	Z61	Z62	Z63	Z64

FIGURE 8: Result of image zoning.

(2) The zone that has the highest number of white pixels is $Z40 = 70$

(3) Feature values for each zone include

$$Z1 = 40/70 = 0.57$$

$$Z12 = 30/70 = 0.42$$

$$Z40 = 70/70 = 1$$

$$Z53 = 50/70 = 0.71$$

$$Z60 = 20/70 = 0.28$$

The feature extraction process by the zoning method will produce 64 features where the feature will be used as an input value at the next stage, which is the classification process using LVQ and can be seen in Figure 9.

2.11. Classification. Classification is a process to train and test the value of features produced through the feature extraction process using the zoning method and classified with Learning Vector Quantization (LVQ). At the classification stage, there are two processes, namely, the training process and the testing process, where the training process is used to train memorization on Learning Vector Quantization (LVQ) while the testing process is testing the value of features that have never been trained [15].

2.12. Training Process. At the training stage, the LVQ algorithm will process the input values by receiving 64 input vectors in the feature class, and then, the vector will calculate the distance of all vectors representing the class.

The process of applying the Vector Quantization Learning Algorithm (LVQ) to the training is as follows [18]:

- (1) The initial process in the LVQ algorithm is the initialization stage to determine the initial weight, maximum iteration, minimum error, and learning rate.
- (2) The input and target values of the input are initialized.
- (3) The next step determines the initial conditions epoch = 0 and error = 1.
- (4) When the epoch is smaller than the maximum epoch, each weight value is calculated, and then, the shortest distance to the weight is set with the value that has been set.
- (5) The next step is to update the weight value if the target class and weight are the same as when using the following equation:

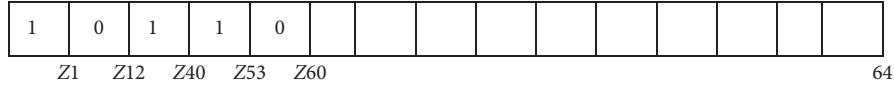


FIGURE 9: Value of feature extraction with zoning.

$$w_j(\text{new}) = w_j(\text{old}) + \alpha[x - w_j(\text{old})]. \tag{3}$$

- (6) The same calculation is repeated for each input using the updated weight.
- (7) After the calculation of the input is complete, the value of α is reduced and α is iterated until it approaches the maximum. The value is determined so that Error $\|X - Wj\|$ becomes a minimum.

2.13. *System Testing and ROC Analysis.* The testing process uses LVQ that has been trained to recognize test data that has never been trained. The testing process is the same as the training process, where the classification calculates the value of each weight input and selects the closest distance between the two weights. When LVQ is tested using training data, testing is performed to see how the memorization of LVQ is developed after going through the training process because the cases included have been studied before.

The results of the testing process on the sample will be adjusted in the contingency table to get the sensitivity, specificity, and accuracy of the contingency table, as can be seen in Table 1. The probability of success from a calculation has four possibilities. The four possibilities are as follows:

- (1) If the doctor diagnoses the brain image as a tumor and the brain image is classified positively identified by the tumor, then true positive (TP) is calculated
- (2) If the doctor diagnoses the brain image as a tumor and the brain image is classified as negatively identified by the tumor, then false negative (FN) is calculated
- (3) If the doctor diagnoses a healthy brain and the brain image is classified as negative, true negative (TN) is calculated
- (4) If the doctor diagnoses a healthy brain image and the brain image is classified as positive, the tumor is calculated as false positive (FP)

$$TPR = \frac{TP}{P} = \text{Recall}, \tag{4}$$

$$FPR = \frac{FP}{N}, \tag{5}$$

$$\text{Precision} = \frac{TP}{TP + FP} \times 100\%, \tag{6}$$

$$\text{Accuracy} = \frac{TP + TN}{P + N} \times 100\%, \tag{7}$$

$$\text{Sensitivity} = \frac{TP}{TP + FN} \times 100\%. \tag{8}$$

TABLE 1: Contingency table.

	P	N
Y	TP (True Positive)	FP (False Positive)
N	FN (False Negative)	TN (True Negative)
Total	P	N

2.14. *Image Preparation.* This part discusses the process of classifying brain images, amounting to 40 images. In the training process, 10 brain images were identified as tumors, and 10 healthy brains for the training process consisted of 10 brain images that were identified as tumors, and 10 were normal. CT-scan brain image data were obtained from medical records of H. Adam Malik General Hospital in patients aged 40 years to 60 years. At this stage, it aims to display the results of the testing process on learning vector quantization. The author builds this application using programming in java.

The CT image data used to support the findings of this study may be released upon application to the Department of Neurology, Adam Malik Hospital, Medan, Sumatera, Utara, Indonesia, who can be contacted at irina.kemala (at) usu.ac.id.

2.15. *Specifications of the CT-Scan Plane Used.* The CT-scan aircraft specifications used are as follows:

- (1) Brand: GE LightSpeed 16 Slice CT
- (2) Rotation: 0.5 s
- (3) Thickness slice: 5 mm
- (4) Kv: 120 kV

3. Results and Discussion

3.1. *Preprocessing.* The initial process carried out in the classification of brain tumors through the stages of pre-processing in which the image will be converted into black and white before the globalization process is carried out. In this study, using a threshold value of 128, determining the threshold value is used to obtain gray values in the image of a brain tumor. The results of this process can be seen in Figure 10.

After the binary image is obtained, the next step is feature extraction using the zoning method. In addition to determining the value of the zoning method, features are also used to determine the location of the tumor. A division of several zones of the same size is performed in order to get the results of the CT scan brain tumor image values. The purpose of this feature extraction stage is to find a collection of features found in the character of the brain image.

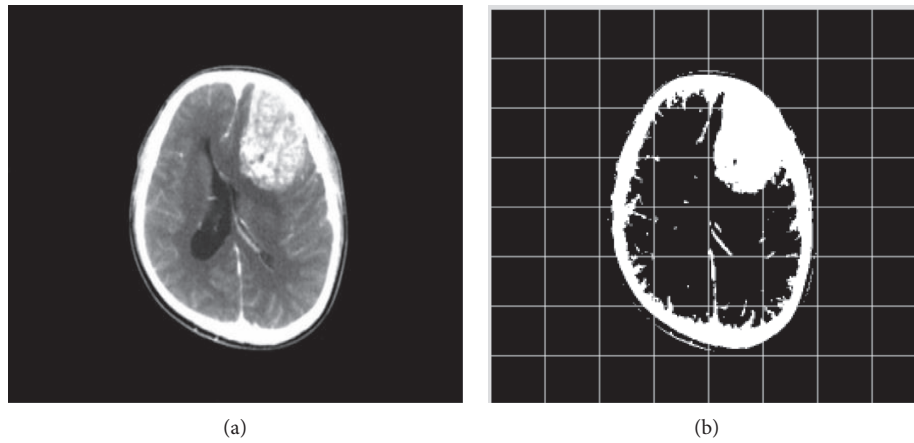


FIGURE 10: Binary image reconstruction.

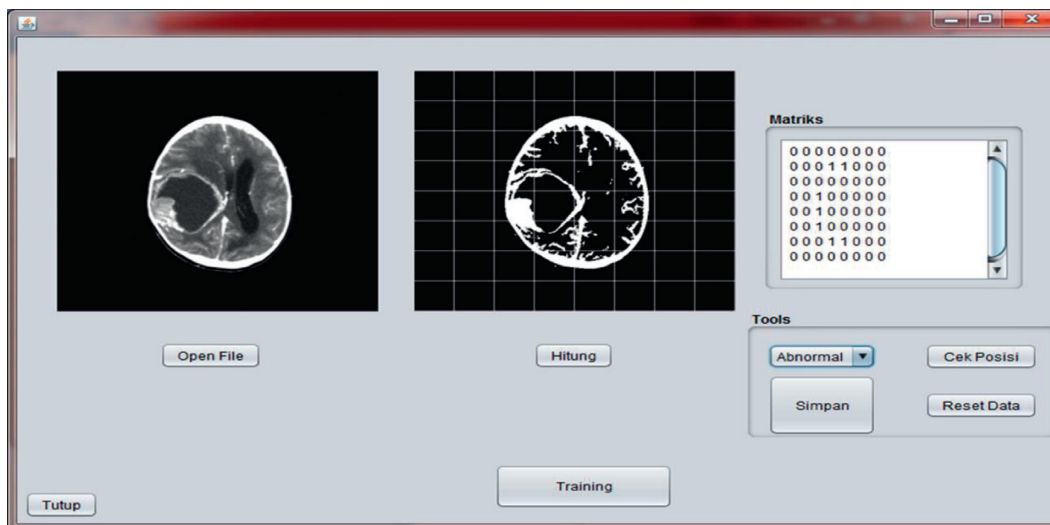


FIGURE 11: Training process.

3.2. Training Process. The image training process uses data in the form of 20 CT scan brain images consisting of 10 normal images and 10 suspected images. CT scan brain images used are 512×512 in size stored on local hard disks, and the classification process uses an artificial neural network LVQ (Learning Vector Quantization). Training can be seen in Figure 11, while the training data from CT brain image can be seen in Table 2.

From Table 2, the weight value in each training data has been seen. The weight value is the final value used in the testing process, where the weight value is obtained from the LVQ calculation process. To make an introduction to the image by calculating the value of each weight in the input and choose the smallest distance on both weights. The value at the smallest weight distance will represent the class in the input image.

3.3. Image Testing Process. During the testing phase, 20 imagery input data were used, consisting of 10 normal brain images and 10 suspected brain images. Display

application of the classification of brain tumors by zoning using learning vector quantization can be seen in Figure 12, and the results of the test can be seen in Table 3.

From Table 3, the input value in data-12 shows the condition of the image for the normal category, but the system shows a suspect; this is because the learning vector quantization method has a weakness of being sensitive to changes in weight values. If the position of the input value in the form of a feature value is changed, the weight value will also change.

3.4. Classification Results Using the LVQ Method. The results of the test data on the application of brain tumor classification are obtained with the learning vector quantization method with an average classification result of 85% so that the results of the accuracy using learning vector quantization can be calculated simply by using the following equation:

TABLE 2: Data set training.

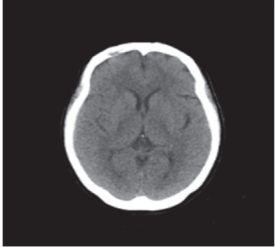
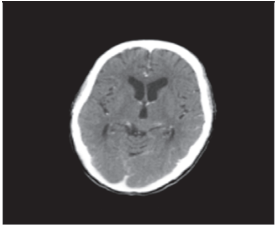
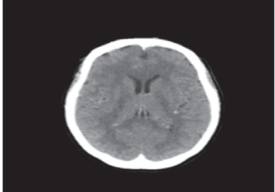
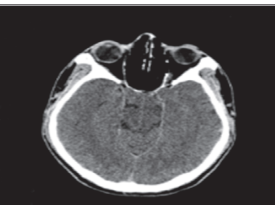
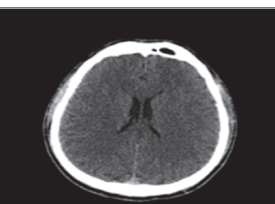
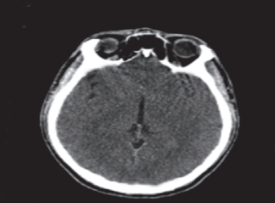
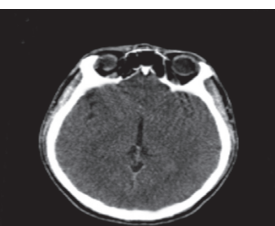
No.	Brain image	Weight	Result
1		0.076161	Normal
2		2.304818	Normal
3		2.2668598	Normal
4		1.456988	Normal
5		2.9700592	Normal
6		1.6688762	Normal
7		1.6688761	Normal

TABLE 2: Continued.

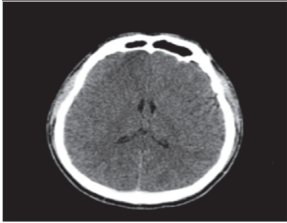
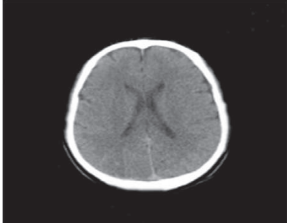
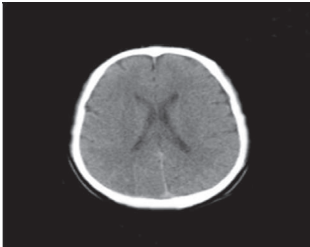
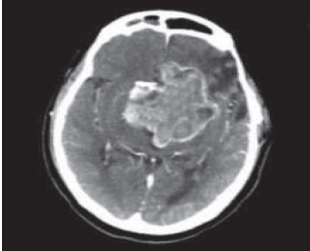
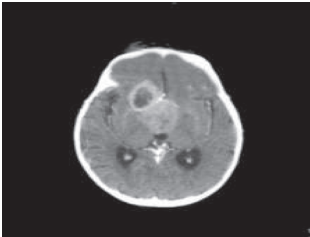
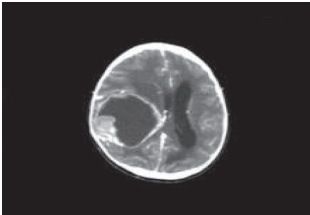
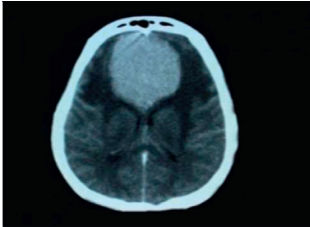
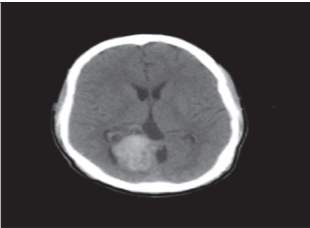
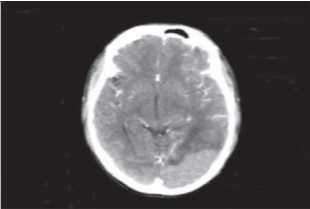
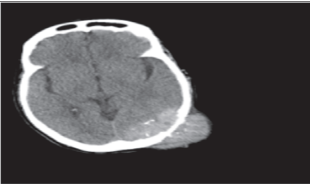
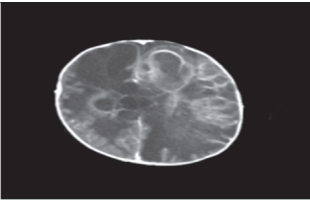
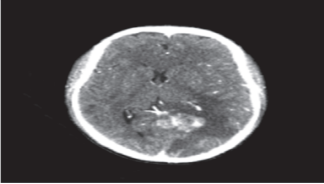
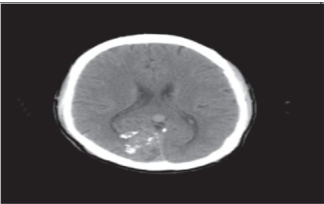
No.	Brain image	Weight	Result
8		2.9700592	Normal
9		2.769984	Normal
10		1.6688762	Normal
11		2.9779766	<i>Suspected</i>
12		2.9736168	<i>Suspected</i>
13		2.9230187	<i>Suspected</i>

TABLE 2: Continued.

No.	Brain image	Weight	Result
14		2.800454	<i>Suspected</i>
15		3.2186778	<i>Suspected</i>
16		1.8768171	<i>Suspected</i>
17		2.3506687	<i>Suspected</i>
18		1.9752706	<i>Suspected</i>
19		3.0961044	<i>Suspected</i>
20		2.006145	<i>Suspected</i>

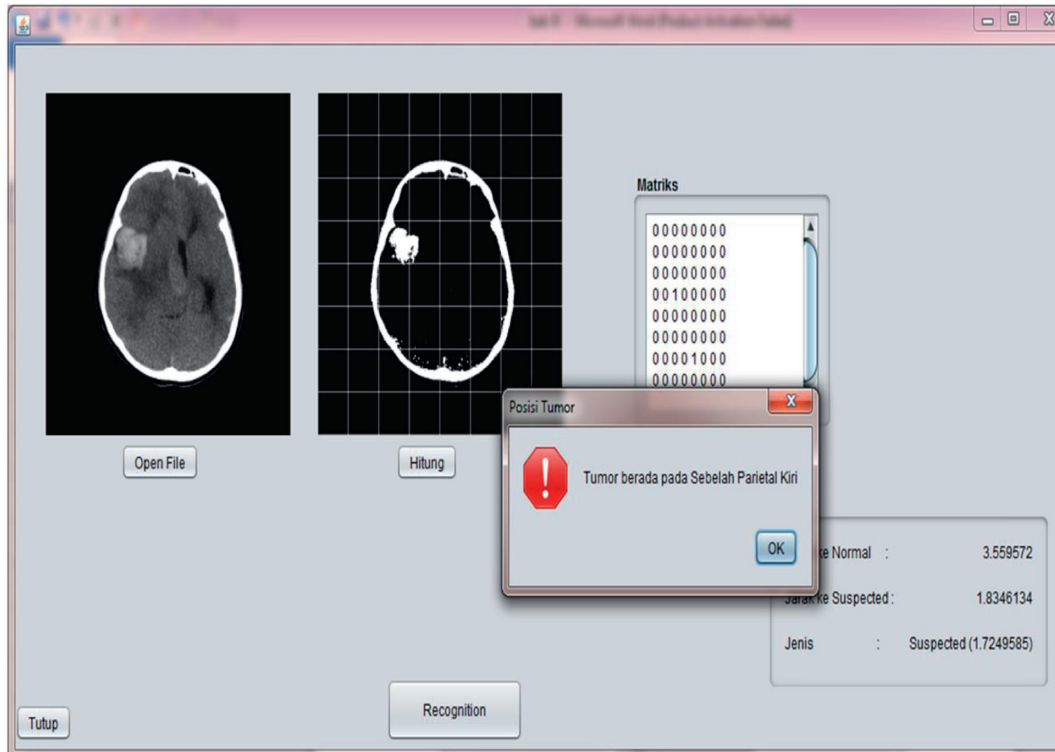


FIGURE 12: Image testing process.

TABLE 3: Result of testings.

No.	Image	Weight 1	Weight 2	Input*	Result	Notes	Pos.
1	Data-5.png	3.489579	2.9736168	Suspected	Suspected	TP	Right
2	Data-9.png	3.7573445	3.2186778	Suspected	Suspected	TP	Right
3	Data-2.png	3.4895792	2.9779766	Suspected	Suspected	TP	Right
4	Data-12.png	3.0037804	2.6869104	Normal	Suspected	FN	Normal
5	Data-13.png	2.304818	2.9392818	Normal	Normal	TN	Normal
7	Data-7.png	3.07729601	1.8768171	Suspected	Suspected	TP	Right
9	Data-19.png	2.2668598	2.9678066	Normal	Normal	TN	Normal
10	Data-11.png	2.305248	2.9393818	Normal	Normal	TN	Normal
11	Data-13.png	2.304818	2.93938118	Normal	Normal	TN	Normal
12	Data-8.png	3.4555268	2.9230187	Suspected	Suspected	TP	Left
13	Data-18.png	2.9360542	2.8076556	Normal	Suspected	FN	Normal
14	Data-4.png	3.5838966	2.800454	Suspected	Suspected	TP	Right
15	Data-1.png	3.043977	2.006145	Suspected	Suspected	TP	Right
16	Data-6.png	3.0350804	2.3506687	Suspected	Suspected	TP	Left
17	Data-10.png	2.3829138	3.0961044	Suspected	Normal	FP	Normal
18	Data-3.png	2.8869388	1.9752706	Suspected	Suspected	TP	Right
19	Data-14.png	2.769984	2.9166098	Normal	Normal	TN	Normal
20	Data-15.png	2.2493293	2.9494078	Normal	Normal	TN	Normal

$$\text{accuracy} = \frac{\text{amount of succesful classification}}{\text{amount of total samples}}$$

$$\times 100\%,$$

$$= \frac{17}{20} \times 100\% = 85\%.$$

(9)

To get accurate results, it is necessary to perform an ROC analysis of the classification results based on the LVQ method; the results for the LVQ method are shown in Table 4.

This study has several limitations. The use of CT imaging in the intensive care unit is very limited nowadays due to the need for a radiographer's presence to analyze and diagnose the patients, sometimes in a not very regular period of time.

TABLE 4: LVQ result.

Classification	LVQ
TP	9
TN	8
FP	2
FN	1
Sensitivity %	90
Specificity %	80
Accuracy %	85

The availability of CT data, therefore, was very limited, especially with manual reading as the golden standard, as explained in the research flowchart (Figure 5). In this study, only 20 images from 40 data images are used for training, and the rest 20 images are used for testing purposes. This split portion of training and testing was applied in order to get the proof on a concept and can be extended in the future.

4. Conclusions

The combination of the zoning algorithm with learning vector quantization can increase the speed of computing and can classify normal and abnormal brains with an average accuracy of 85%. Optimal recognition of image data can be achieved with the learning vector as it is suitable for use in the intensive care unit in hospitals.

The quantization method has a fast calculation in the introduction of an appropriate character so that there are no errors when testing data. The suggestions for developing this study are to compare the learning vector quantization method with the support vector machine method so that it can produce the best way for classifying brain images. The use of the zoning method and learning vector quantization can be applied to further research by adding methods to determine the extent of abnormal brain images.

Data Availability

All the brain CT Image data used to support the findings of this study are available from the corresponding author upon request.

Conflicts of Interest

The authors declare that there are no conflicts of interest regarding the publication of this paper.

Acknowledgments

This research was fully funded by the Ministry of Research, Technology, and Higher Education, Indonesia, through Universitas Sumatera Utara financial year 2019 based on contract no. 11/E1/KP.PTNBH/2019 dated 29 March 2019.

References

- [1] P. N. H. Tra, N. T. Hai, and T. T. Mai, "Image segmentation for detection of benign and malignant tumors," in *Proceedings of IEEE International Conference on Biomedical Engineering (BME-HUST)*, pp. 51–54, IEEE, Hanoi, Vietnam, October 2016.
- [2] A. P. Nanthagopal and R. S. Rajamony, "A region-based segmentation of tumour from brain CT images using non-linear support vector machine classifier," *Journal of Medical Engineering & Technology*, vol. 36, no. 5, pp. 271–277, 2012.
- [3] V. Marita, "Identifikasi tumor otak menggunakan jaringan syaraf tiruan propagasi balik pada citra ct-scan otak," *Prisma Fisika*, vol. 5, no. 3, pp. 117–121, 2014.
- [4] A. Bargaje, A. Kulkarni, and S. Lagad, "Brain tumor detection and classification using adaptive boosting," *International Research Journal of Engineering and Technology (IRJET)*, vol. 4, no. 7, pp. 1961–1965, 2017.
- [5] K. S. Siddharth, R. Dhir, and R. Rani, "Handwritten guru-mukhi character recognition using zoning density and background directional distribution features," *International Journal of Computer Science and Information Technologies*, vol. 2, no. 3, pp. 1036–1041, 2011.
- [6] E. Miranda, M. Aryuni, and E. Irwansyah, "A survey of medical image classification techniques," in *Proceedings of International Conference on Information Management and Technology (ICIMTech)*, pp. 56–61, IEEE, Bandung, Indonesia, November 2016.
- [7] M. Azara, T. Fatayer, and A. E. Halees, "Arabic text classification using learning vector quantization," in *Proceedings of 8th International Conference on Informatics and System (INFOS)*, pp. 40–44, IEEE, Cairo, Egypt, May 2012.
- [8] A. Padma and R. Sukanesh, "SVM based classification of soft tissues in brain CT image using wavelet-based dominant gray level run length texture feature," *Middle-East Journal of Scientific Research*, vol. 13, no. 7, pp. 883–888, 2013.
- [9] M. K. M. Priya, S. Kavitha, and B. Bharathi, "Brain tumor types and grades classification based on statistical feature set using support vector machine," in *Proceedings of 10th International Conference on Intelligent Systems and Control (ISCO)*, pp. 1–8, IEEE, Coimbatore, India, January 2016.
- [10] R. Lavanyadevi, M. Machakowsalya, J. Nivethitha, and A. Niranjil Kumar, "Brain tumor classification and segmentation in MRI images using PNN," in *Proceedings of the International Conference on Electrical, Instrumentation, and Communication Engineering (ICEICE)*, pp. 1–6, IEEE, Karur, India, April 2017.
- [11] F. Fahmi, H. Marquering, G. Streekstra et al., "Automatic detection of CT perfusion datasets unsuitable for analysis due to head movement of acute ischemic stroke patients," *Journal of Healthcare Engineering*, vol. 5, no. 1, pp. 67–78, 2014.
- [12] R. S. Choras, "Image feature extraction techniques and their applications for CBIR and biometrics systems," in *Proceedings of International Journal of Biology and Biomedical Engineering*, vol. 1, no. 1, pp. 6–16, IEEE, Minneapolis, MN, USA, June 2007.
- [13] T. Triantoro, F.R. Batubara, and F. Fahmi, "Image Based water gauge reading developed with ANN Kohonen," in *Proceedings of International Conference on Electrical Engineering and Computer Science (ICEECS)*, pp. 74–78, IEEE, Kuta, Indonesia, November 2014.
- [14] B. Gatos, A. L. Kesidis, and A. Papandreou, "Adaptive zoning features for character and word recognition," in *Proceedings of 11th International Conference on Document Analysis and Recognition*, pp. 1160–1164, IEEE, Beijing, China, September 2011.
- [15] N. B. Karayiannis, "A methodology for constructing fuzzy algorithms for learning vector quantization," in *IEEE*

Transactions on Neural Networks, vol. 8, no. 3, IEEE, New York, NY, USA, May 1997.

- [16] S. K. Khatri, "Recognizing images of handwritten digits using learning vector quantization artificial neural network," in *Proceedings of International Conference on Reliability, Infocom Technologies and Optimization*, pp. 1–4, IEEE, Uttar Pradesh, India, September 2015.
- [17] S. Kusumadewi, "Komputasi dan sistem cerdas," *GRAHA ILMU*, vol. 1, p. 408, 2004.
- [18] F. Fahmi, F. Apriyulida, and S. Suherman, "Brain tumour image classification using learning vector quantization based zoning method," *Journal of Physics: Conference Series*, vol. 1235, no. 1, Article ID 012027, 2019.

Research Article

Cortical Tasks-Based Optimal Filter Selection: An fNIRS Study

Rayyan Azam Khan ¹, Noman Naseer ², Sajid Saleem,³ Nauman Khalid Qureshi ⁴,
Farzan Majeed Noori ⁵, and Muhammad Jawad Khan⁶

¹Department of Mechanical Engineering, University of Saskatchewan, Saskatoon, Saskatchewan S7N 5A9, Canada

²Department of Mechatronics Engineering, Air University, Islamabad 46000, Pakistan

³Department of Electrical Engineering, National University of Modern Languages, Islamabad 46000, Pakistan

⁴Department of Biomedical Engineering, Faculty of Electronic Information and Electrical Engineering,
Dalian University of Technology, Dalian 116000, China

⁵Department of Informatics, Faculty of Mathematics and Natural Sciences, University of Oslo, Oslo 0316, Norway

⁶School of Mechanical and Manufacturing Engineering, National University of Science and Technology,
Islamabad 46000, Pakistan

Correspondence should be addressed to Noman Naseer; noman.naseer@mail.au.edu.pk

Received 16 December 2019; Accepted 25 April 2020; Published 22 May 2020

Academic Editor: Ahmed F. Hussein

Copyright © 2020 Rayyan Azam Khan et al. This is an open access article distributed under the Creative Commons Attribution License, which permits unrestricted use, distribution, and reproduction in any medium, provided the original work is properly cited.

Functional near-infrared spectroscopy (fNIRS) is one of the latest noninvasive brain function measuring technique that has been used for the purpose of brain-computer interfacing (BCI). In this paper, we compare and analyze the effect of six most commonly used filtering techniques (i.e., Gaussian, Butterworth, Kalman, hemodynamic response filter (hrf), Wiener, and finite impulse response) on classification accuracies of fNIRS-BCI. To conclude with the best optimal filter for a specific cortical task owing to a specific cortical region, we divided our experimental tasks according to the three main cortical regions: prefrontal, motor, and visual cortex. Three different experiments were performed for prefrontal and motor execution tasks while one for visual stimuli. The tasks performed for prefrontal include rest (R) vs mental arithmetic (MA), R vs object rotation (OB), and OB vs MA. Similarly, for motor execution, R vs left finger tapping (LFT), R vs right finger tapping (RFT), and LFT vs RFT. Likewise, for the visual cortex, R vs visual stimuli (VS) task. These experiments were performed for ten trials with five subjects. For consistency among extracted data, six statistical features were evaluated using oxygenated hemoglobin, namely, slope, mean, peak, kurtosis, skewness, and variance. Combination of these six features was used to classify data by the nonlinear support vector machine (SVM). The classification accuracies obtained from SVM by using hrf and Gaussian were significantly higher for R vs MA, R vs OB, R vs RFT, and R vs VS and Wiener filter for OB vs MA. Similarly, for R vs LFT and LFT vs RFT, hrf was found to be significant ($p < 0.05$). These results show the feasibility of using hrf for effective removal of noises from fNIRS data.

1. Introduction

Brain-computer interface (BCI) also known as human-machine interface (HMI) or brain-machine interface (BMI) provides a communication mean between the user and external devices through a combination of hardware and software systems [1–3]. These systems are trained to generate control commands based on a specific set of patterns of brain signals [4].

Brain signal acquisition is categorized between invasive and noninvasive techniques. However, due to surgical risks and limited access to the cortical region, noninvasive

techniques are common in practice [5]. Noninvasive modalities include functional magnetic resonance interference (fMRI), functional near-infrared spectroscopy (fNIRS) [6], and electroencephalography (EEG) [4]. fNIRS is a comparatively new modality that has better spatial resolution and low artifacts, cost, and portability [4, 7]. So far, promising results have been shown by fNIRS-BCI [8–10]. Acquired brain signals for a specific task may contain noises that can contaminate signals and can effect informative data. These noises are categorized between physiological noise, experimental noise, and instrumental noise [8, 11]. In fNIRS,

the experimental noises are removed prior to the change of the raw signal to its magnitude through the modified Beer-Lambert law [8, 12, 13]. Noises produced due to hardware or by surrounding are known to be instrumental noises. These noises usually have high frequency that can be removed using low-pass filter; furthermore, keeping isolation from external sources such as light can reduce such type of noises. Experimental noises include motion artifacts such as head motion during signal acquisition that can cause the dislocation of optodes from the assigned position, thus generates a spike-like noise due to change in light intensity. Various studies [13–15] have utilized commonly developed filtering techniques randomly for noise removal. However, obtained signals can be corrupted by different kinds of noises that could affect further analysis. Noises can be physiologically produced due to Mayer waves (~ 0.1 Hz), respiration ($0.2\sim 0.5$ Hz), and heartbeat ($1\sim 1.5$ Hz), mainly due to fluctuations of blood pressure [8, 16–19]. These noises can be removed using adaptive or bandpass filtering [20, 21]. After preprocessing, useful information is extracted from the filtered data afterward classified using different classifiers mainly named as linear discriminant analysis (LDA), support vector machine (SVM), quadratic discriminant analysis (QDA), and naïve bayes (NB) [22] to generate control commands, hence completing the loop for BCI. Previous studies [13, 14, 23] show that an appropriate filter for correctness of data is the key to achieve more accurate results.

In this study, we hypothesized to find an optimal filter for commonly used cortical tasks, owing to a particular cortical region. Hence, we compared six commonly used filters to remove previously discussed noises. These filters include discrete Kalman [24], time-varying Wiener [25], 4th order Butterworth, hemodynamic response filter (hrf), Gaussian [26], and window-based finite impulse response (FIR) [27]. For the said purpose, cortical data were acquired from the three main regions of the brain, namely, prefrontal (PFC), motor (MC), and visual cortex (VC). Since the data acquired from PFC relate to thinking tasks [28–31], hence arithmetic and object rotation tasks were performed for this cortical region [32–34]. Similarly, tasks related to movement of limbs or fingers is related to the motor cortex [35]; therefore, the finger tapping tasks were performed for desired data acquisition [36–38]. Likewise, flickering of checker box was performed for visual cortex data [39]. Keeping in view the target of an optimal filter for a specific cortical region, a previous study [22] reported the different combinations of statistical features. Therefore, for consistency of extracted data, statistical features were kept the same for all experimental tasks, hence making combinations of six features, namely, signal mean (SM), signal slope (SS), signal peak (SP), signal skewness (SK), signal kurtosis (KR), and signal variance (SV). For classification, a number of studies [22, 40, 41] reported nonlinear SVM classifiers for comparatively better accuracies, hence all experimental tasks were classified using a nonlinear SVM classifier. Therefore, the main contribution of this work is (1) to analyze the effect of the six most commonly used filtering techniques and (2) to propose the optimal one among the most frequently

discussed noise removal techniques. For the aforementioned experiment, we select three main cortical regions: prefrontal, motor, and visual cortex with seven various paradigms. The canonical hemodynamic response filter (hrf) [26] performed overall best among the opted techniques. On the basis of these systematic and explicit analyses, it can be seen that selection of an optimal filter has a significant role in enhancing accuracies. Hence, these observations can serve as a standard guide for others to test the effect of noise correction algorithms for fNIRS experiments, and therefore can select a significant methodology.

2. Materials and Methods

2.1. Experimental Setup. To acquire experimental data, seven paradigms owing to three main cortical regions were designed and explicitly performed using a dynamic near-infrared optical tomography (DYNOT-232; NIRx Medical Technologies, NY, USA) device at Pusan National University. It operates on two wavelengths that are 760 and 830 nm where the signal acquisition sampling frequency was 1.81 Hz. Five healthy subjects with normal or corrected-to-normal vision took part in the experiment with a verbal consent before experimentation. All subjects were right-handed with an age range of 26 ± 3 . Right-handed subjects were selected to minimize hemodynamic response variation due to hemispheric-dominance difference. The experimental participants had no history of alcoholism, psychiatric, neurological, and visual disorder, cardiovascular and respiratory disease, mental illness, or any motor disability. Moreover, three hours before the commencement of the study, participants were asked to refrain from caffeinated drinks. As discussed in the literature [28, 30, 31, 35, 37, 38], for thinking-related task, signals were acquired from PFC, similarly for motor execution tasks from the primary motor cortex (PMC), and visual stimuli task from VC. Performed experiments were according to the latest Declaration of Helsinki.

2.2. Experimental Paradigms. In accordance with the literature [35, 39], subjects were seated on a comfortable chair and were asked to take rest with restricted movements as they can, so that the hemodynamic response activation owing to previous activities can be avoided. Hence, each paradigm related to PFC, MC, and VC starts with a rest of 20 s period to set up the baseline conditions. As the literature [42–45] show, (10–12) s task is adequate to acquire hemodynamic response of brain activity, hence 20 s initial rest was followed by 10 s task, and this was followed in turn by another 20 s rest period permitting signals to return to their baseline values before the start of the next trial in paradigm (a). For paradigm (b), 20 s rest after 10 s task 1 was again followed by 10 s task 2. The 20 s rest between two 10 s tasks was added to differentiate two classes through the baseline value. Figure 1 depicts paradigm (a) and paradigm (b). For optimal filter selection, tasks were selected concerning specific cortical regions such that for PFC, three different experiments were performed, rest (R) vs mental arithmetic (MA), R vs object rotation (OB), and OB vs MA task. Similarly, for MC, R vs left finger tapping (LFT), R vs right

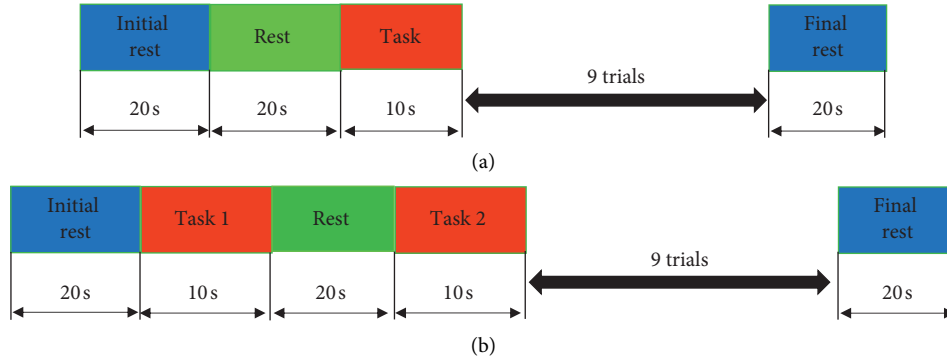


FIGURE 1: Experimental paradigms for cortical tasks. (a) Task vs rest. (b) Task 1 vs task 2.

finger tapping (RFT), and LFT vs RFT. Likewise, for VC, R vs visual stimuli (VS) task.

2.2.1. Prefrontal Tasks

(1) *Mental Arithmetic*. According to previous studies [44, 46, 47], for R vs MA task, subjects were asked to perform a series of arithmetic calculations for 10 s based on the pseudorandom order, such that to subtract the random two-digit number (between 10 and 20) successively from the previous result of the three-digit number subtraction appearing on the screen (e.g., 400-11, 389-17, and 372-14). Afterwards, the screen was turned black so that subjects does not go beyond the 10 s task.

(2) *Object Rotation*. For the object rotation task, subjects were asked to imagine a cube rotating for the 10 s task while the “object rotation” word appeared for 10 s on the screen at about 2 m distance [48–50].

(3) *Mental Arithmetic vs Object Rotation*. In this protocol, subjects were asked to perform the aforementioned MA task versus OB task in between 20 s of rest to distinguish two tasks. The experimental paradigm is depicted in Figure 1(b).

2.2.2. Motor Tasks

(1) *Finger Tapping*. According to the literature [8, 17, 19, 23, 31, 37, 38, 51], subjects were asked to tap the self-paced index finger of one hand for 10 s afterwards the 20 s rest task was performed allowing signals to return to their reference values. Also, repetition for 10 times was performed as depicted in Figure 1(a). Similar trials were performed on the other hand, while for the LFT vs RFT task, 20 s rest was performed in between two tasks for the restoration of the signal to the baseline level as shown in Figure 1(b).

2.2.3. Visual Task

(1) *Checker Box Flickering*. In this experiment [4, 18, 39], a screen was placed in front of the subjects at a distance of approximately 2 m, and also subjects were requested to avoid

eye blinking during the experiment. The 10 s task of checker box flickering at 4 Hz was performed followed by 20 s rest of the black screen. The sound was also generated during the transition between rest and task. The paradigm followed for visual stimuli is shown in Figure 1(a).

2.3. *Experimental Setup*. Since the mental imagery task activates the PFC [34, 43], a total 11 of near-infrared (NI) light optodes were placed on PFC, 3 of which were detectors and 8 were the source in accordance with the literature [46, 47]. Similarly, for the motor execution task, the primary motor cortex (PMC) is activated [37, 43], hence 15 optodes were placed on PMC out of which 8 were the source and 7 were detectors. To extract data for LFT, optodes were placed on the right hemisphere, while for RFT on the left hemisphere [43]. Similarly, for the visual stimuli task data acquisition from the visual cortex [4, 18, 39], eleven optodes were placed having eight sources and three detectors. The distance between the source and the detector was 3 cm. Optode placement with channel configuration for MC, VC, and PFC is shown in Figure 2.

2.3.1. *Signal Acquisition*. In accordance with the literature [6, 8, 29], the raw optical density signal is converted to oxyhemoglobin ($\Delta c_{\text{HbO}}(t)$) and deoxyhemoglobin ($\Delta c_{\text{HbR}}(t)$) concentration using the modified Beer–Lambert law (MBLL) as described in the following equation:

$$\begin{bmatrix} \Delta c_{\text{HbO}}(t) \\ \Delta c_{\text{HbR}}(t) \end{bmatrix} = \frac{\begin{bmatrix} \beta_{\text{HbO}}(\lambda_1) & \beta_{\text{HbR}}(\lambda_1) \\ \beta_{\text{HbO}}(\lambda_2) & \beta_{\text{HbR}}(\lambda_2) \end{bmatrix}^{-1} \begin{bmatrix} \Delta \psi(t, \lambda_1) \\ \Delta \psi(t, \lambda_2) \end{bmatrix}}{d * l}, \quad (1)$$

where $\beta_{\text{HbX}}(\lambda)$ is the HbX extinction coefficient in $\{\mu\text{M}^{-1}\text{cm}^{-1}\}$, d is the differential path length factor for the curved path in (mm), l is the detector and emitter distance in (mm), and $\Delta \psi_{\text{HbX}}(t)$ is the absorbance difference of the light emitter wavelength of λ_i .

2.4. *Signal Processing*. The acquired raw signals of the brain contain various noises that can be categorized into physiological, experimental, and instrumental noise [8, 52]. In

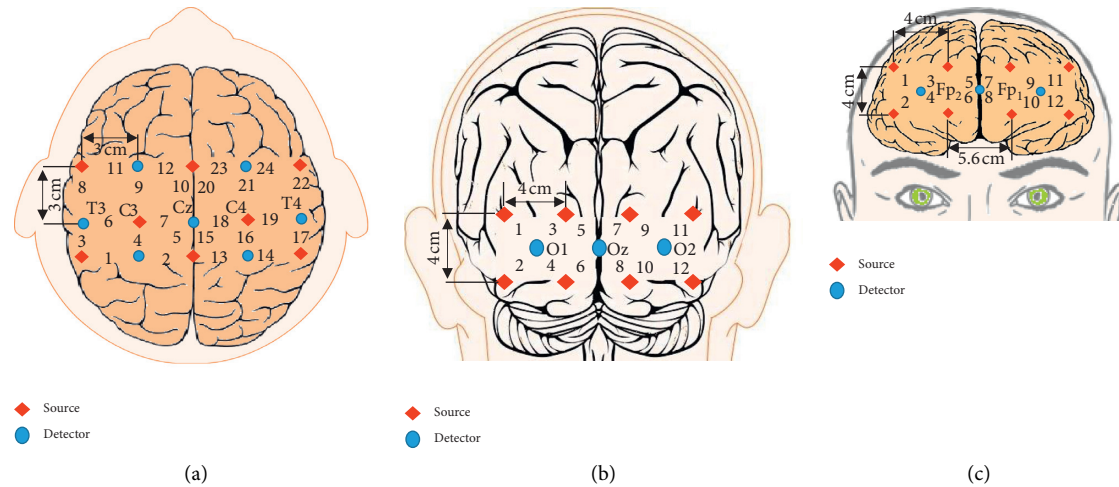


FIGURE 2: Optode placement configuration in accordance with the 10–20 international system. (a) Motor cortex. (b) Visual cortex. (c) Prefrontal cortex.

fNIRS, the instrumental and experimental noises are removed prior to change of the raw signal to its magnitude through MBLL [8, 12, 14].

2.4.1. Instrumental Noises. Noises produced due to hardware or by surrounding are categorized under instrumental noises. These noises usually have high frequency that can be removed using a low-pass filter; furthermore, keeping isolation from external sources such as light can reduce such type of noises [8].

2.4.2. Experimental Noises. These errors contain motion artifacts due to unintentional body movements like head motion during signal acquisition. It can cause the dislocation of optodes from the assigned positions that result in a spike-like noise due to change in light intensity. Filters like Kalman and Wiener can be used to remove such type of noises [12–15].

2.4.3. Physiological Noises. These noises are produced due to Mayer waves (~ 0.1 Hz), respiration (~ 0.5 Hz), and heartbeat ($1\sim 1.5$ Hz) that occur due to fluctuations of blood pressure [16–19]. These noises can be removed using adaptive or bandpass filtering [8, 20, 38].

2.5. Data Analysis. NIRS-SPM is a toolbox designed for fNIRS data analysis. For signal processing, it provides common filtering techniques, namely, Butterworth, Gaussian, and hrf [26]. The comparative data analysis was performed by implementing Gaussian and hrf filtering using the NIRS-SPM toolbox, while other techniques on MATLAB® 2017b. The generalized mathematical models with necessary details are as follows.

2.5.1. Gaussian Filtering. A Gaussian filter is used in various forms depending upon the nature of the signal. Generally, a Gaussian filter is based on a Gaussian function which defines

the probability distribution of noise or data. It can also be used as a smoothing operator. A Gaussian kernel is used for smoothing the signal in which each value is replaced with the weighted average of itself and its neighboring values [14, 21, 26]. A simple representation of the 2D Gaussian filter can be defined in the following equation as

$$G(x, y) = \frac{1}{2\pi\sigma^2} e^{-(x^2+y^2)/2\sigma^2}, \quad (2)$$

where x and y are the distance from the origin in horizontal and vertical axis and σ is the known standard deviation of the distribution.

2.5.2. Hemodynamic Response Filter (hrf). The hrf is based on the canonical representation of the hemodynamic response functions (HRF) and is used for the temporal smoothing of the fNIRS time series signal. In NIRS-SPM, the given functional data were smoothen using the least square estimate with ideal HRF. The hrf and Gaussian filter model details are in accordance with the literature [26].

2.5.3. Butterworth Filter. Butterworth filter is a model-based bandpass filter which performs on frequency attenuation using high and low-pass filter. The filtered value not only depends on the weighted average of the unfiltered time series, but also recursively on the previous values of the filtered time series. This filter aims to have a flat frequency response in the desired pass band [26]. The 4th order Butterworth filter with a band pass of (0.01~0.1) Hz was applied by MATLAB® build in a library for the desired experiments.

2.5.4. Finite Impulse Response Filter. FIR filter is designed by finding the coefficients and filter order so that it performs a cross-correlation between the input signal and the time reversed impulse response; therefore, by sampling the pulse shape, coefficients of the filter are designed [14]. FIR filter of order N can be defined as the following equation:

$$x[n] = \sum_{i=0}^N a_i y[n-i], \quad (3)$$

where $y[n]$ is the input signal, $x[n]$ is the output signal, N is the filter order, and b_i is the value of impulse response at i^{th} instance. Here, the 4th order FIR filter with a low-pass band of 0.1 Hz was utilized. The coefficients were estimated using the least square estimate. However, a time-varying Wiener filter, based on the short-time Fourier series, was implemented as in [25, 53].

2.5.5. Kalman Filter. Kalman filters the input signal containing statistical and other noises by linear quadratic estimation. The estimated unknown variables based on the Bayesian inference and joint probability distribution tend to be more accurate [13, 14]. Its simple model can be seen in the following equation:

$$x_k = F_k x_{k-1} + B_k u_k + w_k, \quad (4)$$

where F_k is the state transition model applied to previous state x_{k-1} , B_k is the control input model applied to the control vector u_k , and w_k is the process noise. A discrete model of Kalman was implemented in accordance with [24].

2.6. Feature Selection. For the consistency between extracted data across all paradigms, six statistical features (SV, KR, SS, SM, SK, and SP) were used to extract information across data [28, 43, 46, 54, 55]. SM is calculated in the following equation as

$$SM = \frac{1}{n} \sum_{x=1}^n A_x, \quad (5)$$

where A_x is the input signal such that $\Delta c_{\text{HbO}}(t)$ and n is the total number of observations. Signal variance is calculated in equation (6) as

$$\sigma^2 = \frac{1}{n-1} \sum_{x=1}^{n-1} (Z_x - \mu)^2, \quad (6)$$

where Z_x is the input signal, μ is the mean found from equation (6), n is the number of samples, and σ is the standard deviation. For KR, calculation was made by the following equation:

$$\text{kurt}(X) = E \left[\left(\frac{X - \mu}{\sigma} \right)^4 \right], \quad (7)$$

where X is the input signal and E is the expected value of X .

SK is the asymmetry of values relative to normal distribution around the mean, hence calculated in the following equation:

$$\text{skew}(X) = E \left[\left(\frac{X - \mu}{\sigma} \right)^3 \right]. \quad (8)$$

MATLAB[®] polyfit function fits the line to all input data points, therefore used to calculate SS. Similarly, max

function was used to calculate SP. Statistical features were rescaled between 0 and 1 using the following equation:

$$Z' = \frac{Z - \min(Z)}{\max(Z) - \min(Z)}, \quad (9)$$

where Z' is the rescaled feature and Z refers to the original feature values. The scatter plot across all six statistical features for the OB vs MA task of subject 1 is shown in Figure 3.

2.7. Support Vector Machine. Statistical significance of accuracy is analyzed for selection of an optimal filter for a specific cortical region; therefore, for higher classification performance, nonlinear SVM is used [35, 38]. It can rescale high-dimensional data and can control errors explicitly by maximizing the margins between two or more classes thus creating hyperplanes named as support vectors [40, 41, 56].

The cost function that is to be maximized for the SVM classifier gives a correlation between training data and hyperplane as defined in equations (10) and (11), respectively,

$$\text{Minimize } \frac{1}{2} \|z\|^2 + k \sum_{x=1}^N \varepsilon_x, \quad (10)$$

$$\text{Provided } y_x (Z^T \xi_x + a)^3 \geq 1 - \varepsilon_x, \quad \varepsilon_x \geq 0, \quad (11)$$

where z , $\xi_x \in R^2$, $b \in R^1$, $z^2 = z^T z$, k is the positive regularization parameter, ε_x is the measure of the training error, and y_x is the class label for the n^{th} sample. Here, the third-degree polynomial kernel function with $k = 0.5$ and 10-fold cross-validation was applied for the estimation of classification accuracies [53].

3. Results and Discussion

3.1. Results. In this study, an optimal filter was chosen based on cortical tasks. Activities were categorized based on three main regions such as PFC, MC, and VC. $\Delta c_{\text{HbO}}(t)$ signals were filtered using six filters. Figures 4–6 show the averaged $\Delta c_{\text{HbO}}(t)$ filtered signals across trials of prefrontal, motor execution and, visual stimuli tasks. The three different signals show various paradigms for each brain region, while the horizontal axis is aligned with one complete event. The pictorial analysis of filtered responses shows that using the 4th order Butterworth changes data form altogether while discrete Kalman and Wiener filtered the signals, but there remain some noises in the output response, whereas, canonical hrf and Gaussian give much smoother response as compared to any other technique. Moreover, previous studies have commonly utilized Butterworth for signal processing, while the obtained visual does not show any significant improvement in comparison. Likewise, the Gaussian filter is also utilized in various studies that assume the acquired data with some normal distribution; therefore, it considers Gaussian function which defines the probability distribution of noise or data. It can also be used as a smoothing operator. A Gaussian kernel is used for smoothing the signal in which each value is replaced with the weighted average of itself and its neighbouring values.

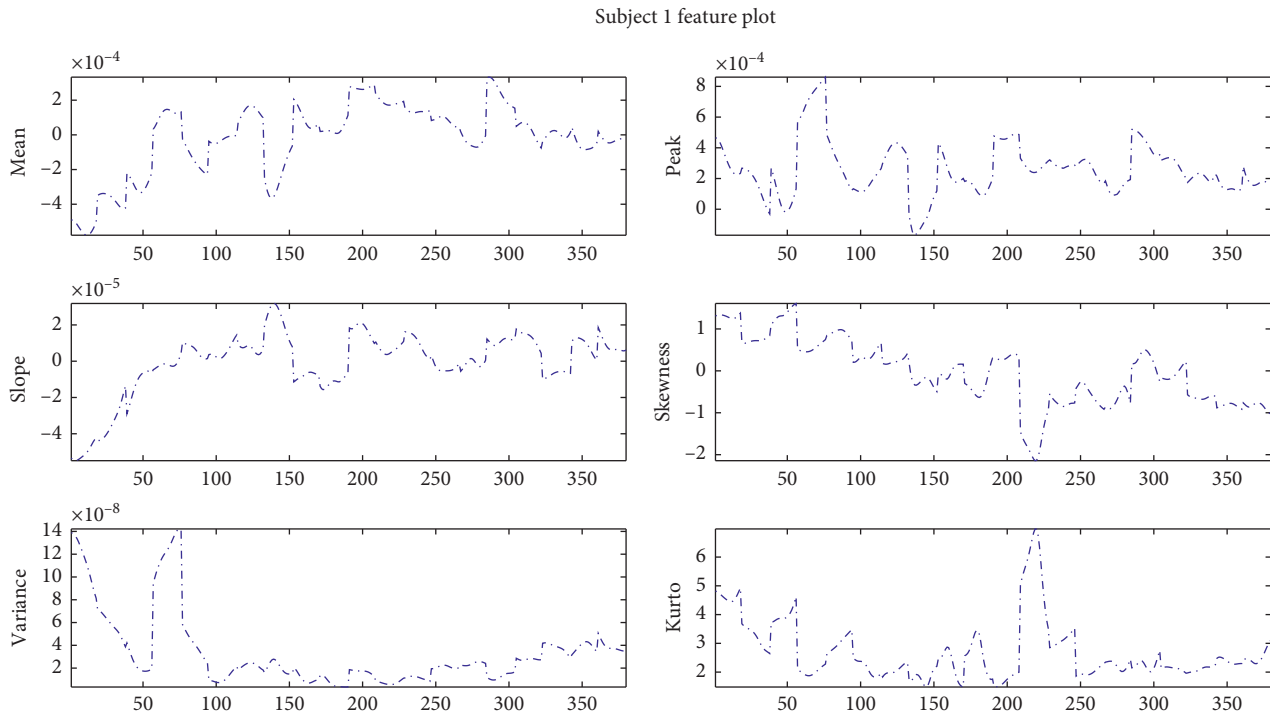


FIGURE 3: Extracted feature scatter plot for OB vs MA.

However, the hrf filter considers ideal hemodynamic response as a reference for smoothing the data that are closely related to chi-squared distribution. Due to this fact, hrf outperforms any other considered technique.

For consistency among extracted information, classification accuracies were obtained across six statistical features. The accuracies obtained across these features are shown in Table 1. The two-tailed independent t -test was performed to check statistical significance with Holm–Bonferroni for multiple comparison of filters. Results obtained in Table 2 show significance using hrf or the Gaussian filter for R vs MA and R vs OB while for the OB vs MA task, no significant filter was found; however, the time-varying Wiener filter outperformed others. Similarly, in motor execution tasks, hrf was found to be significant for R vs LFT, likewise for R vs RFT hrf and Gaussian. Moreover, for LFT vs RFT, the hrf filter shows better performance. In the VS task, hrf and Gaussian were significant. Moreover, we plot the mean accuracies of filters with respect to cortical regions as depicted in Figure 7. The Gaussian and canonical hrf performed consistently better across all three cortical regions. However, comparatively better accuracies were obtained using hrf only. The statistical results validate our hypothesis of optimal filter selection by assuring that hrf generally has better performance for fNIRS-based studies, which is in accordance with a previous study [53].

3.2. Discussion. Despite of the fact that fNIRS offers portability, low cost, and ease of equipment setup, there still remains a challenge of removing noises like systematic physiological (Mayer waves, muscle activity, blood pressure,

and respiration and heart rate) and artifacts [17, 57], as fNIRS signals are highly contaminated by measurement noises and physiology-based systemic interference [58]. Several studies have proposed methodologies that can remove noises robustly. In [59], temporal filtering using a low-pass filter with 0.6 Hz cutoff frequency and canonical hemodynamic response function with 4 s full width at half maximum was applied. In [60], exponential moving average and Chebyshev filter were used to remove artifacts from the fNIRS data. Similarly, in [61], only low-pass filter with a 0.14 Hz cutoff was applied to remove physiological noises from fNIRS signals. Aqil et al. [62] used recursive least square estimation for online imaging. This adaptive approach provided a spatial filtering with low and high pass, detrending, and baseline correction. Similarly, Seo et al. [63] assessed the utility of NIRS in removal of physiological noises in fMRI data by reducing variance of the residual error in the baseline fMRI signal through the NIRS signal in the model. Similarly, in [64], adaptive filtration with the affine projection algorithm was used to accelerate convergence with colored noise, but it increases computational cost. In [65], a bandpass filter based on the 5th order Butterworth filter was used to filter motor execution signals based on EEG. In literature [52], fNIRS-based walking signals and walking signals while talking were acquired. These signals were preprocessed using a low-pass with finite impulse response filter, while the talking task results in low-amplitude artifacts with a similar frequency of hemodynamic response, hence it may affect cortical activity [57]. In [66], multiple filters were applied for EEG- and ECG-based signal preprocessing such as for removal of motion artifacts, a median filter with 5-point, for systemic component

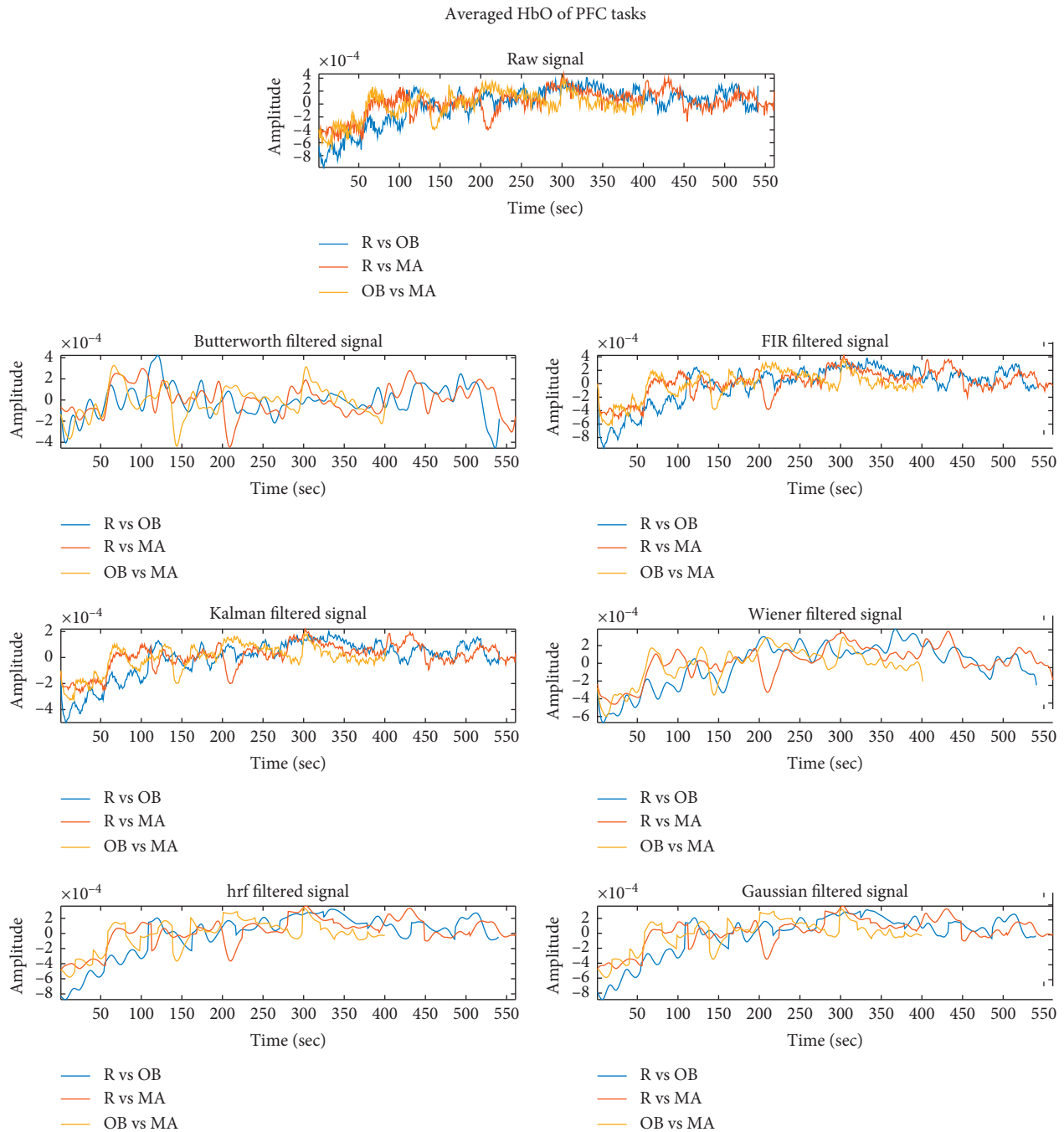


FIGURE 4: Filtered averaged HbO of PFC tasks.

removal, a second-order Chebychev type-2 filter, high-pass filter for signal drift removal, 1st order low-pass Butterworth filter for blood pressure signal, and the 4th order Butterworth bandpass filter for ECG were applied, while using too many filters for every aspect may result in cost of computation. In [8], previously mentioned aspects in Section 2.4 were briefly discussed. To remove such noise methods like MBL, eigen-based vector approach [19], a bandpass filter was introduced in a MATLAB-based graphical user interface-based program, HomER. However, no such statistical significance comparison was seen for generic tasks. In literature [14, 15],

cancellation of motion artifacts using Wiener and discrete Kalman filter was discussed; meanwhile, t -tests performed in comparison showed better performance with Kalman. Similarly, in [12, 13], four techniques, namely, Kalman, principal component analysis, wavelet analysis, and spline interpolation, were compared to remove NIRS data artifacts. Results showed that spline interpolation and wavelet analysis were significant for such noise removals. In [67], systemic noise was removed using wavelet minimum description length detrending approach and artifact using moving standard deviation and spline interpolation. Eggenberger

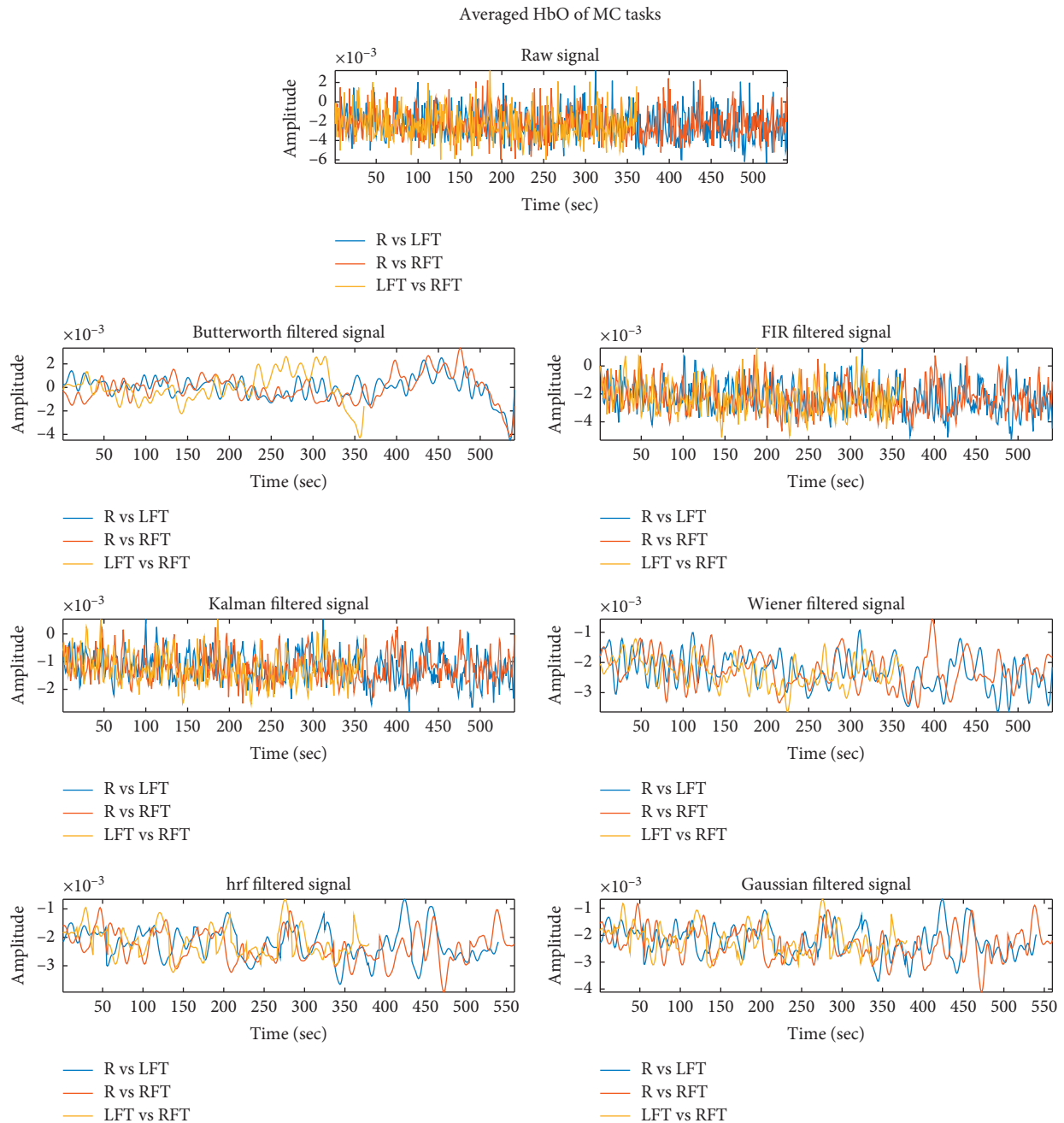


FIGURE 5: Filtered averaged HbO of MC tasks.

et al. [68] removed movement artifacts by using visual inspection, and Mayer waves were avoided using averaged blocks. In [69], physiological noise was removed with a low-pass filter, and sliding window was applied for motion artifact rejection. Holtzer et al. [70] combined independent component analysis and principal component analysis to remove noise and signal drifts. In [70–77], the signal was low-pass filtered with a cutoff frequency at 0.14 Hz, and in [78], with a cutoff frequency of 0.2 Hz and in [78], a low-pass filter set at 0.67 Hz, meanwhile a moving average filter with a width of 4 s was used to smoothen the signal. In [79], Gaussian smoothing with a full width at half max of 2 s was

applied, while motion artifacts were removed using the wavelet minimum description length detrending algorithm. In [80], a bandpass filter (0.01–1.25 Hz) was applied to the signal. Likewise, in [81], a bandpass filter (0.01–0.2 Hz) was applied while motion artifacts were removed through principal component analysis and spike rejection. Similarly, in [82], data were bandpass filtered (0.01 Hz to 0.14 Hz), while the wavelet filter and correlation-based signal improvement were applied to remove motion artifacts. In [83], data were filtered with a 0.01 Hz high-pass filter and a 5.0 s moving average filter and also principal component analysis were applied to reduce physiological noise. Metzger et al.

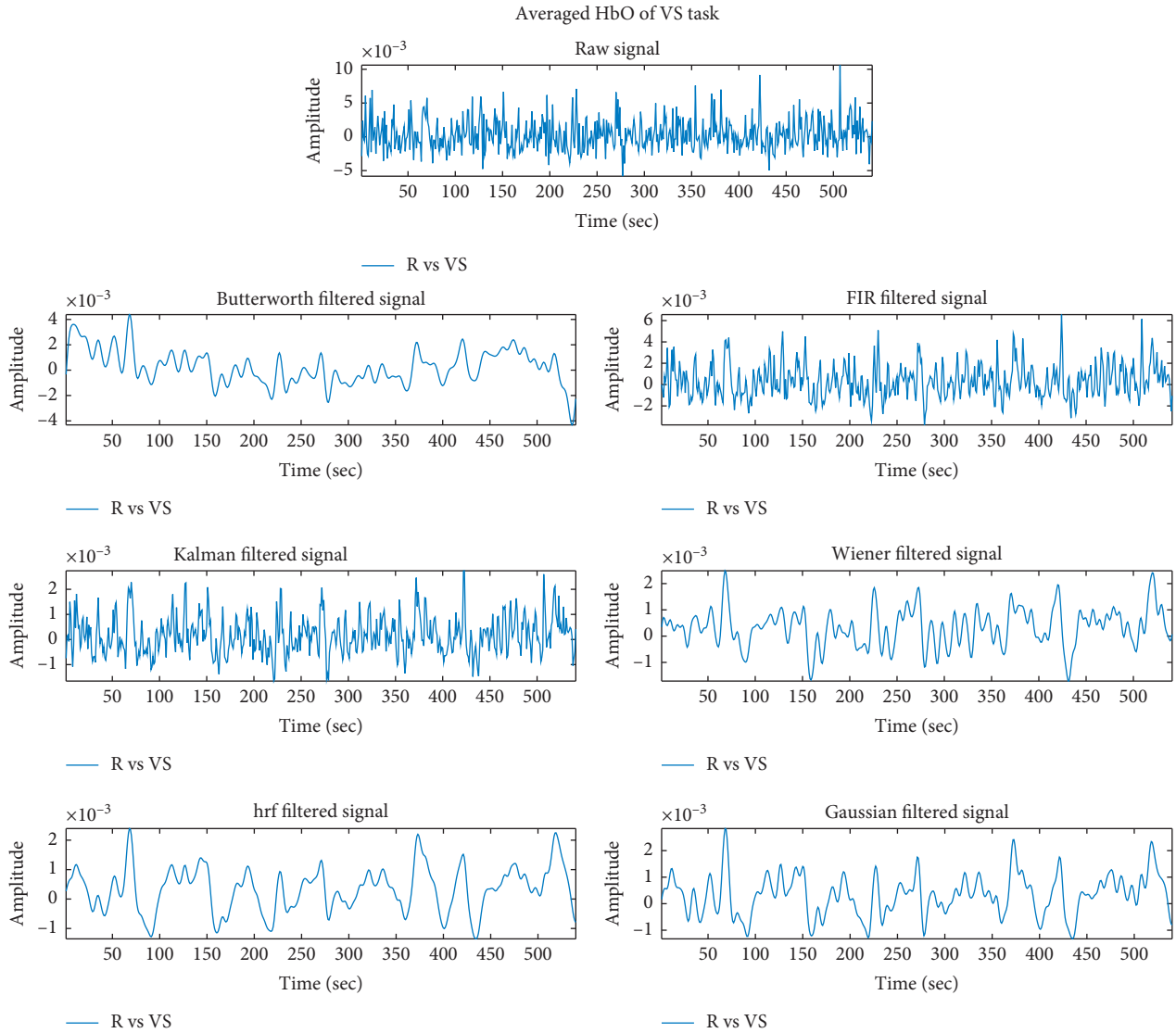


FIGURE 6: Filtered averaged HbO of VS task.

TABLE 1: Accuracies across six features for multiple cortical paradigms.

<i>Prefrontal tasks</i>						
R vs MA						
Subjects	Butter	FIR	Gaussian	hrf	Kalman	Wiener
S1	57.03	62.22	81.48	82.96	82.96	80
S2	57.77	59.25	71.85	83.7	68.148	69.62
S3	58.51	54.07	88.14	90.37	73.33	82.22
S4	64.44	71.85	82.22	82.96	72.59	74.81
S5	55.55	69.62	85.18	82.22	61.48	74.81
R vs OB						
S1	63.7	68.14	80	86.66	71.48	75.18
S2	54.81	68.88	78.51	80	68.88	73.33
S3	60	65.92	82.22	89.62	89.22	74.81
S4	63.7	71.11	97.03	97.03	90.37	94.81
S5	60	60	82.96	77.03	68.14	65.18
OB vs MA						
S1	50	64.44	68.88	75.55	85.55	90
S2	53.33	66.66	72.22	72.22	84.44	86.66

TABLE 1: Continued.

S3	54.44	68.88	85.55	80	76.66	74.44
S4	56.66	71.11	81.11	83.33	85.55	86.66
S5	57.77	75.55	82.22	82.22	85.55	88.88
<i>Motor execution tasks</i>						
R vs LFT						
S1	65.18	57.03	77.03	81.48	57.03	66.66
S2	60	57.77	78.51	85.18	45.18	50.37
S3	55.55	49.62	67.4	72.59	59.25	59.25
S4	53.33	56.29	68.14	73.33	60	61.48
S5	45.18	57.77	76.29	76.29	45.18	45.18
R vs RFT						
S1	61.48	43.7	78.51	89.62	66.66	65.92
S2	59.25	58.51	68.88	79.25	59.25	59.25
S3	57.77	65.92	68.88	62.96	46.66	60.74
S4	54.81	51.85	66.66	74.07	60	47.4
S5	62.96	58.51	71.85	77.03	55.77	56.29
LFT vs RFT						
S1	54.44	46.66	87.77	92.22	64.44	60
S2	55.55	61.11	64.44	76.66	53.33	51.11
S3	58.88	58.88	64.44	68.88	63.33	45.55
S4	54.44	57.77	78.88	80	48.88	52.22
S5	60	62.22	70	80	55.55	56.66
<i>Visual stimuli task</i>						
R vs VS						
S1	53.33	60.74	71.11	65.18	48.88	51.85
S2	54.81	66.66	74.07	75.55	59.25	62.96
S3	59.25	64.44	76.29	82.22	71.11	69.62
S4	57.77	47.4	68.14	73.33	49.62	57.77
S5	68.88	62.96	73.33	78.51	56.29	61.48

TABLE 2: Statistical significance of filters across multiple cortical paradigms.

Filters	<i>p</i> values
<i>Prefrontal tasks</i>	
R vs MA	
Butter vs hrf, FIR, Gaussian, Kalman, Wiener	0.089, 0.012, 0.012, 0.012, 0.012
hrf vs Gaussian, Wiener, FIR, Kalman	0.089, 0.012, 0.012, 0.022
Gaussian vs FIR, Kalman, Wiener	0.012, 0.089, 0.012
Kalman vs Wiener, FIR	0.089, 0.089
Wiener vs FIR	0.012
R vs OB	
Butter vs FIR, Gaussian, Kalman, Wiener, hrf	0.022, 0.012, 0.012, 0.012, 0.012
hrf vs Kalman, Gaussian, Wiener, FIR	0.012, 0.158, 0.012, 0.012
Gaussian vs FIR, Kalman, Wiener	0.012, 0.089, 0.012
Kalman vs Wiener, FIR	0.327, 0.022
Wiener vs FIR	0.012
OB vs MA	
Butter vs FIR, Gaussian, Kalman, Wiener, hrf	0.012, 0.012, 0.012, 0.012, 0.012
hrf vs Kalman, Gaussian, Wiener, FIR	0.089, 0.281, 0.089, 0.012
Gaussian vs FIR, Kalman, Wiener	0.012, 0.089, 0.089
Kalman vs Wiener, FIR	0.089, 0.012
Wiener vs FIR	0.012
<i>Motor execution tasks</i>	
R vs LFT	
Butter vs FIR, Gaussian, Kalman, Wiener, hrf	0.65, 0.025, 1, 0.158, 0.025
hrf vs Kalman, Gaussian, Wiener, FIR	0.012, 0.022, 0.012, 0.025
Gaussian vs FIR, Kalman, Wiener	0.012, 0.012, 0.012
Kalman vs Wiener, FIR	0.041, 1
Wiener vs FIR	0.32

TABLE 2: Continued.

Filters	<i>p</i> values
R vs RFT	
Butter vs FIR, Gaussian, Kalman, Wiener, hrf	0.089, 0.012, 0.5, 0.5, 0.012
hrf vs Kalman, Gaussian, Wiener, FIR	0.012, 0.089, 0.012, 0.089
Gaussian vs FIR, Kalman, Wiener	0.012, 0.012, 0.012
Kalman vs Wiener, FIR	0.5, 0.32
Wiener vs FIR	0.32
LFT vs RFT	
Butter vs FIR, Gaussian, Kalman, Wiener, hrf	0.158, 0.012, 0.32, 0.089, 0.012
hrf vs Kalman, Gaussian, Wiener, FIR	0.012, 0.012, 0.012, 0.012
Gaussian vs FIR, Kalman, Wiener	0.012, 0.012, 0.012
Kalman vs Wiener, FIR	0.32, 0.32
Wiener vs FIR	0.089
<i>Visual stimuli</i>	
R vs VS	
Butter vs FIR, Gaussian, Kalman, Wiener, hrf	0.32, 0.012, 0.32, 0.5, 0.012
hrf vs Kalman, Gaussian, Wiener, FIR	0.012, 0.089, 0.012, 0.012
Gaussian vs FIR, Kalman, Wiener	0.012, 0.012, 0.012
Kalman vs Wiener, FIR	0.089, 0.32
Wiener vs FIR	0.32

Filters mean accuracies with standard deviation

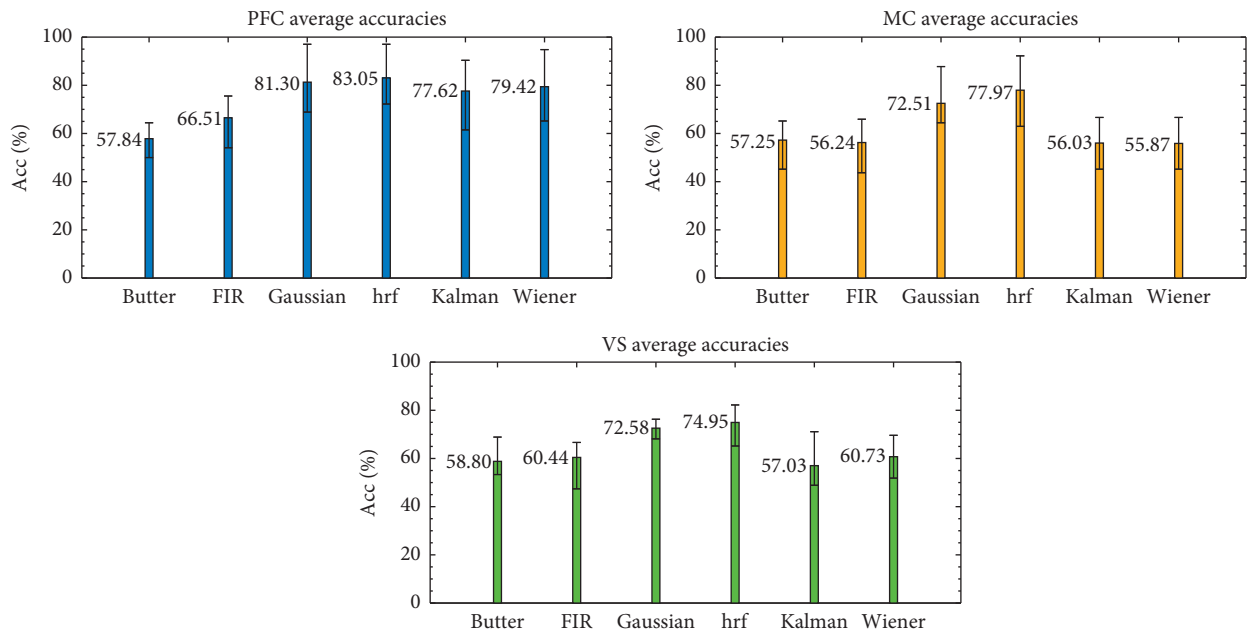


FIGURE 7: Filters' mean accuracies.

[84] removed channels with large movement or technical artifacts. Smaller artifacts were corrected with the correlation-based signal improvement method while a low-pass filter with a 5.0 s moving average filter was applied. In [85–87], signals were analyzed with SPM99 (Statistical Parametric Mapping software; Wellcome Department of Cognitive Neurology, London, UK). In [88], moving standard deviation-based artifact removal (moving artifact reduction algorithm: MARA) with a threshold of 0.45 for HbO and 0.18 for HbR was applied and signals were linearly detrended and low-pass filtered at 0.1 Hz.

Keeping in view the discussions in the literature, various methodologies were adopted for artifact removal while for systematic physiological noises, mostly high and low-pass filter were applied. Therefore, to make use of the best optimal filter for a specific cortical task, we performed an explicit and systematic analysis to find the filter based on statistical significance for mostly used cortical tasks in fNIRS study applications. The result shows that hrf outperforms the discussed techniques due to the fact that it considers ideal hemodynamic response distribution for smoothing the data. Keeping this in view, our future work involves designing of

an adaptive filter technique, considering different distributions of data and noise. Therefore, opting more accurate separation of data.

4. Conclusion

To the best of our knowledge, this is the first study to propose filter selection for commonly used cortical tasks of functional near-infrared spectroscopy (fNIRS) contaminated with artifacts and systematic physiological noises. Six filters, namely, Gaussian, hemodynamic response filter (hrf), Butterworth, time-varying Wiener, discrete Kalman, and window-based finite impulse response, were tested. The results obtained have validated the overall statistical significance of the hrf for prefrontal, motor, and visual cortex tasks. Furthermore, signals acquired from different cortical regions may contain different types of noises. Hence, the prime goal of this study was to suggest an optimal filter for a specific task, owing to the specific cortical region so that further studies can achieve maximum accuracies by reliably improving the recovered hemodynamic response function. Outcome of this study shows that there is a significant impact of filter selection on the accuracy of the classified data, therefore facilitating users to avoid analysis of complex signal techniques by themselves.

Data Availability

The data used to support the findings of this study are available from the corresponding author upon request.

Conflicts of Interest

The authors declare that there are no conflicts of interest regarding the publication of this paper.

Acknowledgments

The authors would like to thank Prof. Keum-Shik Hong from Pusan National University for providing them an opportunity to visit his lab and use the equipment in his lab for data acquisition.

References

- [1] N. Naseer and K.-S. Hong, "fNIRS-based brain-computer interfaces: a review," *Frontiers in Human Neuroscience*, vol. 9, pp. 1–15, 2015.
- [2] L. F. Nicolas-Alonso and J. Gomez-Gil, "Brain computer interfaces, a review," *Sensors*, vol. 12, no. 2, pp. 1211–1279, 2012.
- [3] J. R. Wolpaw, N. Birbaumer, D. J. McFarland, G. Pfurtscheller, and T. M. Vaughan, "Brain-computer interfaces for communication and control," *Clinical Neurophysiology*, vol. 113, no. 6, pp. 767–791, 2002.
- [4] A. Ferreira, W. C. Celeste, F. A. Cheein, T. F. Bastos-Filho, M. Sarcinelli-Filho, and R. Carelli, "Human-machine interfaces based on EMG and EEG applied to robotic systems," *Journal of NeuroEngineering and Rehabilitation*, vol. 5, no. 1, p. 10, 2008.
- [5] S. Waldert, "Invasive vs. Non-invasive neuronal signals for brain-machine interfaces: will one prevail?" *Frontiers in Neuroscience*, vol. 10, pp. 1–4, 2016.
- [6] M. Aqil, K.-S. Hong, M.-Y. Jeong, and S. S. Ge, "Detection of event-related hemodynamic response to neuroactivation by dynamic modeling of brain activity," *Neuroimage*, vol. 63, no. 1, pp. 553–568, 2012.
- [7] S. Fok, R. Schwartz, M. Wronkiewicz et al., "An EEG-based brain computer interface for rehabilitation and restoration of hand control following stroke using ipsilateral cortical physiology," in *Proceedings of the 2011 Annual International Conference of the IEEE Engineering in Medicine and Biology Society*, pp. 6277–6280, IEEE, Boston, MA, USA, August 2011.
- [8] T. J. Huppert, S. G. Diamond, M. A. Franceschini, and D. A. Boas, "HomER: a review of time-series analysis methods for near-infrared spectroscopy of the brain," *Applied Optics*, vol. 48, no. 10, pp. 280–298, 2009.
- [9] M. Schneider and I. Miyai, "Review of functional near-infrared spectroscopy in neurorehabilitation," *Neurophotonics*, vol. 3, Article ID 031414, 2016.
- [10] A. Venkatakrishnan, G. E. Francisco, and J. L. Contreras-Vidal, "Applications of brain-machine interface systems in stroke recovery and rehabilitation," *Current Physical Medicine and Rehabilitation Reports*, vol. 2, no. 2, pp. 93–105, 2014.
- [11] F. Jobsis, "Noninvasive, infrared monitoring of cerebral and myocardial oxygen sufficiency and circulatory parameters," *Science*, vol. 198, no. 4323, pp. 1264–1267, 1977.
- [12] S. Brigadoi, L. Ceccherini, S. Cutini et al., "Motion artifacts in functional near-infrared spectroscopy: a comparison of motion correction techniques applied to real cognitive data," *Neuroimage*, vol. 85, pp. 181–191, 2014.
- [13] R. J. Cooper, J. Selb, L. Gagnon et al., "A systematic comparison of motion artifact correction techniques for functional near-infrared spectroscopy," *Frontiers in Neuroscience*, vol. 6, pp. 1–10, 2012.
- [14] M. Izzetoglu, P. Chitrapu, S. Bunce, and B. Onaral, "Motion artifact cancellation in NIR spectroscopy using discrete Kalman filtering," *BioMedical Engineering OnLine*, vol. 9, no. 1, p. 16, 2010.
- [15] M. Izzetoglu, A. Devaraj, S. Bunce, and B. Onaral, "Motion artifact cancellation in NIR spectroscopy using wiener filtering," *IEEE Transactions on Biomedical Engineering*, vol. 52, no. 5, pp. 934–938, 2005.
- [16] D. a. Boas, K. Chen, D. Grebert, and M. A. Franceschini, "Improving the diffuse optical imaging spatial resolution of the cerebral hemodynamic response to brain activation in humans," *Optics Letters*, vol. 29, no. 13, p. 1506, 2004.
- [17] D. A. Boas, A. M. Dale, and M. A. Franceschini, "Diffuse optical imaging of brain activation: approaches to optimizing image sensitivity, resolution, and accuracy," *Neuroimage*, vol. 23, pp. S275–S288, 2004.
- [18] M. A. Franceschini, D. K. Joseph, T. J. Huppert, S. G. Diamond, and D. A. Boas, "Diffuse optical imaging of the whole head," *Journal of Biomedical Optics*, vol. 11, no. 5, Article ID 054007, 2006.
- [19] Y. Zhang, D. H. Brooks, M. A. Franceschini, and D. A. Boas, "Eigenvector-based spatial filtering for reduction of physiological interference in diffuse optical imaging," *Journal of Biomedical Optics*, vol. 10, no. 1, Article ID 011014, 2005.
- [20] G. Bauernfeind, S. C. Wriessnegger, I. Daly, and G. R. Müller-Putz, "Separating heart and brain: on the reduction of physiological noise from multichannel functional near-infrared spectroscopy (fNIRS) signals," *Journal of Neural Engineering*, vol. 11, no. 5, Article ID 056010, 2014.

- [21] E. Kirilina, N. Yu, A. Jelzow, H. Wabnitz, A. M. Jacobs, and I. Tachtsidis, "Identifying and quantifying main components of physiological noise in functional near infrared spectroscopy on the prefrontal cortex," *Frontiers in Human Neuroscience*, vol. 7, pp. 1–17, 2013.
- [22] N. Naseer, N. K. Qureshi, F. M. Noori, and K.-S. Hong, "Analysis of different classification techniques for two-class functional near-infrared spectroscopy-based brain-computer interface," *Computational Intelligence and Neuroscience*, vol. 2016, Article ID 5480760, 11 pages, 2016.
- [23] M. D. Pfeifer, F. Scholkmann, and R. Labruyère, "Signal processing in functional near-infrared spectroscopy (fNIRS): methodological differences lead to different statistical results," *Frontiers in Human Neuroscience*, vol. 11, pp. 1–12, 2018.
- [24] M. J. Grimble, *Robust Industrial Control Systems*, John Wiley & Sons, Chichester, UK, 2006.
- [25] A. Y. Kostiev, A. Y. Butrym, and S. N. Shulga, "Time-varying wiener filtering based on short-time fourier transform," in *Proceedings of the 2012 6th International Conference on Ultrawideband and Ultrashort Impulse Signals*, pp. 305–308, IEEE, Kiev, Ukraine, 2012.
- [26] J. Ye, S. Tak, K. Jang, J. Jung, and J. Jang, "NIRS-SPM: statistical parametric mapping for near-infrared spectroscopy," *Neuroimage*, vol. 44, no. 2, pp. 428–447, 2009.
- [27] R. B. Lake, "Programs for digital signal processing," *Proceedings of the IEEE*, vol. 69, no. 7, pp. 856–857, 1981.
- [28] K.-S. Hong, N. Naseer, and Y.-H. Kim, "Classification of prefrontal and motor cortex signals for three-class fNIRS-BCI," *Neuroscience Letters*, vol. 587, pp. 87–92, 2015.
- [29] M. Mihara, I. Miyai, M. Hatakenaka, K. Kubota, and S. Sakoda, "Role of the prefrontal cortex in human balance control," *Neuroimage*, vol. 43, no. 2, pp. 329–336, 2008.
- [30] S. D. Power and T. Chau, "Automatic single-trial classification of prefrontal hemodynamic activity in an individual with Duchenne muscular dystrophy," *Developmental Neurorehabilitation*, vol. 16, no. 1, pp. 67–72, 2012.
- [31] S. D. Power, T. H. Falk, and T. Chau, "Classification of prefrontal activity due to mental arithmetic and music imagery using hidden Markov models and frequency domain near-infrared spectroscopy," *Journal of Neural Engineering*, vol. 7, no. 2, Article ID 026002, 2010.
- [32] N. Naseer, F. M. Noori, N. K. Qureshi, and K.-S. Hong, "Determining optimal feature-combination for LDA classification of functional near-infrared spectroscopy signals in brain-computer interface application," *Frontiers in Human Neuroscience*, vol. 10, pp. 1–10, 2016.
- [33] F. M. Noori, N. Naseer, N. K. Qureshi, H. Nazeer, and R. A. Khan, "Optimal feature selection from fNIRS signals using genetic algorithms for BCI," *Neuroscience Letters*, vol. 647, pp. 61–66, 2017.
- [34] N. K. Qureshi, N. Naseer, F. M. Noori, H. Nazeer, R. A. Khan, and S. Saleem, "Enhancing classification performance of functional near-infrared spectroscopy- brain-computer interface using adaptive estimation of general linear model coefficients," *Frontiers in Neuroinformatics*, vol. 11, 2017.
- [35] K.-S. Hong and N. Naseer, "Reduction of delay in detecting initial dips from functional near-infrared spectroscopy signals using vector-based phase Analysis," *International Journal of Neural Systems*, vol. 26, no. 3, Article ID 1650012, 2016.
- [36] P.-H. Chang, S.-H. Lee, K.-M. Gu et al., "The cortical activation pattern by a rehabilitation robotic hand: a functional NIRS study," *Frontiers in Human Neuroscience*, vol. 8, pp. 1–7, 2014.
- [37] S. P. Perrey, "Possibilities for examining the neural control of gait in humans with fNIRS," *Frontiers in Physiology*, vol. 5, pp. 10–13, 2014.
- [38] N. Thanh Hai, N. Q. Cuong, T. Q. Dang Khoa, and V. Van Toi, "Temporal hemodynamic classification of two hands tapping using functional near-infrared spectroscopy," *Frontiers in Human Neuroscience*, vol. 7, pp. 1–12, 2013.
- [39] X. Liu and K.-S. Hong, "fNIRS based color detection from human visual cortex," in *Proceedings of the 2015 54th Annual Conference of the Society of Instrument and Control Engineers of Japan (SICE)*, pp. 1156–1161, IEEE, Hangzhou, China, July 2015.
- [40] C. J. C. Burges, "A tutorial on support vector machines for pattern recognition," *Data Mining and Knowledge Discovery*, vol. 2, pp. 121–167, 1998.
- [41] C. Ashina and V. Vapnik, "Support-vector networks," *Machine Learning*, vol. 20, no. 3, pp. 273–297, 1995.
- [42] M. Naito, Y. Michioka, K. Ozawa, Y. Ito, M. Kiguchi, and T. Kanazawa, "A communication means for totally locked-in ALS patients based on changes in cerebral blood volume measured with near-infrared light," *IEICE Transactions on Information and Systems*, vol. E90-D, no. 7, pp. 1028–1037, 2007.
- [43] N. Naseer and K.-S. Hong, "Classification of functional near-infrared spectroscopy signals corresponding to the right- and left-wrist motor imagery for development of a brain-computer interface," *Neuroscience Letters*, vol. 553, pp. 84–89, 2013.
- [44] N. Naseer and K.-S. Hong, "Decoding answers to four-choice questions using functional near infrared spectroscopy," *Journal of Near Infrared Spectroscopy*, vol. 23, no. 1, pp. 23–31, 2015.
- [45] R. Lima-Saad, H. Zhang, C. Guan et al., "Temporal classification of multichannel near-infrared spectroscopy signals of motor imagery for developing a brain-computer interface," *Neuroimage*, vol. 34, no. 4, pp. 1416–1427, 2007.
- [46] N. Naseer, M. J. Hong, and K.-S. Hong, "Online binary decision decoding using functional near-infrared spectroscopy for the development of brain-computer interface," *Experimental Brain Research*, vol. 232, no. 2, pp. 555–564, 2014.
- [47] S. D. Power, A. Kushki, and T. Chau, "Towards a system-paced near-infrared spectroscopy brain-computer interface: differentiating prefrontal activity due to mental arithmetic and mental singing from the no-control state," *Journal of Neural Engineering*, vol. 8, no. 6, Article ID 066004, 2011.
- [48] B. Abibullaev and J. An, "Classification of frontal cortex haemodynamic responses during cognitive tasks using wavelet transforms and machine learning algorithms," *Medical Engineering & Physics*, vol. 34, no. 10, pp. 1394–1410, 2012.
- [49] A. Faress and T. Chau, "Towards a multimodal brain-computer interface: combining fNIRS and fTCD measurements to enable higher classification accuracy," *Neuroimage*, vol. 77, pp. 186–194, 2013.
- [50] H.-J. Hwang, J.-H. Lim, D.-W. Kim, and C.-H. Im, "Evaluation of various mental task combinations for near-infrared spectroscopy-based brain-computer interfaces," *Journal of Biomedical Optics*, vol. 19, Article ID 077005, 2014.
- [51] N. Naseer, F. Ali, S. Ahmed, S. Iftikhar, R. A. Khan, and H. Nazeer, "EMG based control of individual fingers of robotic hand," in *Proceedings of the 2018 International Conference on Sustainable Information Engineering and Technology (SIET)*, Malang, Indonesia, November 2018.

- [52] R. Holtzer, J. R. Mahoney, M. Izzetoglu, C. Wang, S. England, and J. Verghese, "Online fronto-cortical control of simple and attention-demanding locomotion in humans," *Neuroimage*, vol. 112, pp. 152–159, 2015.
- [53] R. A. Khan, N. Naseer, N. K. Qureshi, F. M. Noori, H. Nazeer, and M. U. Khan, "fNIRS-based Neurobotic Interface for gait rehabilitation," *Journal of NeuroEngineering and Rehabilitation*, vol. 15, no. 1, p. 7, 2018.
- [54] R. Khan, N. Naseer, H. Nazeer, and M. N. Khan, "Control of a prosthetic leg based on walking intentions for gait rehabilitation: an fNIRS study," *Frontiers in Human Neuroscience*, vol. 12, 2018.
- [55] F. M. Noori, N. K. Qureshi, R. A. Khan, and N. Naseer, "Feature selection based on modified genetic algorithm for optimization of functional near-infrared spectroscopy (fNIRS) signals for BCI," in *Proceedings of the 2016 2nd International Conference on Robotics and Artificial Intelligence (ICRAI)*, pp. 50–53, IEEE, Los Angeles, CA, USA, April 2016.
- [56] R. A. Khan, N. Naseer, and M. J. Khan, "Drowsiness detection during a driving task using fNIRS," in *Neuroergonomics*, pp. 79–85, Elsevier, Amsterdam, Netherlands, 2019.
- [57] R. Vitorio, S. Stuart, L. Rochester, L. Alcock, and A. Pantall, "fNIRS response during walking-artefact or cortical activity? A systematic review," *Neuroscience & Biobehavioral Reviews*, vol. 83, pp. 160–172, 2017.
- [58] S. Kubota and J. C. Ye, "Statistical analysis of fNIRS data: a comprehensive review," *Neuroimage*, vol. 85, pp. 72–91, 2014.
- [59] R. Rosas-Romero, E. Guevara, K. Peng et al., "Prediction of epileptic seizures with convolutional neural networks and functional near-infrared spectroscopy signals," *Computers in Biology and Medicine*, vol. 111, Article ID 103355, 2019.
- [60] A. Rahimpour, H. A. Noubari, and M. Kazemian, "A case-study of NIRS application for infant cerebral hemodynamic monitoring: a report of data analysis for feature extraction and infant classification into healthy and unhealthy," *Informatics in Medicine Unlocked*, vol. 11, pp. 44–50, 2018.
- [61] R. Lamb, P. Antonenko, E. Etopio, and A. Seccia, "Comparison of virtual reality and hands on activities in science education via functional near infrared spectroscopy," *Computers & Education*, vol. 124, pp. 14–26, 2018.
- [62] M. Aqil, K.-S. Hong, M.-Y. Jeong, and S. S. Ge, "Cortical brain imaging by adaptive filtering of NIRS signals," *Neuroscience Letters*, vol. 514, no. 1, pp. 35–41, 2012.
- [63] R. J. Seo, L. Gagnon, D. M. Goldenholz, D. A. Boas, and D. N. Greve, "The utility of near-infrared spectroscopy in the regression of low-frequency physiological noise from functional magnetic resonance imaging data," *Neuroimage*, vol. 59, no. 4, pp. 3128–3138, 2012a.
- [64] M. A. Kamran and K.-S. Hong, "Linear parameter-varying model and adaptive filtering technique for detecting neuronal activities: an fNIRS study," *Journal of Neural Engineering*, vol. 10, no. 5, Article ID 056002, 2013.
- [65] J. Höhne, E. Holz, P. Staiger-Sälzer, K.-R. Müller, A. Kübler, and M. Tangermann, "Motor imagery for severely motor-impaired patients: evidence for brain-computer interfacing as superior control solution," *PLoS One*, vol. 9, no. 8, Article ID e104854, 2014.
- [66] R. Zimmermann, L. Marchal-Crespo, J. Edelmann et al., "Detection of motor execution using a hybrid fNIRS-biosignal BCI: a feasibility study," *Journal of NeuroEngineering and Rehabilitation*, vol. 10, no. 1, p. 4, 2013.
- [67] R. Beurskens, I. Helmich, R. Rein, and O. Bock, "Age-related changes in prefrontal activity during walking in dual-task situations: a fNIRS study," *International Journal of Psychophysiology*, vol. 92, no. 3, pp. 122–128, 2014.
- [68] P. Eggenberger, M. Wolf, M. Schumann, and E. D. de Bruin, "Exergame and balance training modulate prefrontal brain activity during walking and enhance executive function in older adults," *Frontiers in Aging Neuroscience*, vol. 8, pp. 1–16, 2016.
- [69] A. Izzetoglu, C. Bohil, J. Lewis, and M. Neider, "Prefrontal cortex activity during walking while multitasking," *Proceedings of the Human Factors and Ergonomics Society Annual Meeting*, vol. 57, no. 1, pp. 1224–1228, 2013.
- [70] R. Holtzer, J. R. Mahoney, M. Izzetoglu, K. Izzetoglu, B. Onaral, and J. Verghese, "fNIRS study of walking and walking while talking in young and old individuals," *The Journals of Gerontology Series A: Biological Sciences and Medical Sciences*, vol. 66A, no. 8, pp. 879–887, 2011.
- [71] M. E. Hernandez, R. Holtzer, G. Chaparro et al., "Brain activation changes during locomotion in middle-aged to older adults with multiple sclerosis," *Journal of the Neurological Sciences*, vol. 370, pp. 277–283, 2016.
- [72] R. Holtzer, C. Schoen, E. Demetriou et al., "Stress and gender effects on prefrontal cortex oxygenation levels assessed during single and dual-task walking conditions," *European Journal of Neuroscience*, vol. 45, no. 5, pp. 660–670, 2017.
- [73] R. Verghese, J. Verghese, G. Allali, M. Izzetoglu, C. Wang, and J. R. Mahoney, "Neurological gait abnormalities moderate the functional brain signature of the posture first hypothesis," *Brain Topography*, vol. 29, no. 2, pp. 334–343, 2016.
- [74] R. Holtzer, J. Yuan, J. Verghese, J. R. Mahoney, M. Izzetoglu, and C. Wang, "Interactions of subjective and objective measures of fatigue defined in the context of brain control of locomotion," *The Journals of Gerontology Series A: Biological Sciences and Medical Sciences*, vol. 72, pp. 167–423, 2016.
- [75] I. Maidan, H. Bernad-Elazari, E. Gazit, N. Giladi, J. M. Hausdorff, and A. Mirelman, "Changes in oxygenated hemoglobin link freezing of gait to frontal activation in patients with Parkinson disease: an fNIRS study of transient motor-cognitive failures," *Journal of Neurology*, vol. 262, no. 4, pp. 899–908, 2015.
- [76] A. Mirelman, I. Maidan, H. Bernad-Elazari et al., "Increased frontal brain activation during walking while dual tasking: an fNIRS study in healthy young adults," *Journal of NeuroEngineering and Rehabilitation*, vol. 11, no. 1, p. 85, 2014.
- [77] J. Verghese, C. Wang, E. Ayers, M. Izzetoglu, and R. Holtzer, "Brain activation in high-functioning older adults and falls," *Neurology*, vol. 88, no. 2, pp. 191–197, 2017.
- [78] M.-I. B. Lin and K.-H. Lin, "Walking while performing working memory tasks changes the prefrontal cortex hemodynamic activations and gait kinematics," *Frontiers in Behavioral Neuroscience*, vol. 10, 2016.
- [79] H. Y. Kim, S. P. Yang, G. L. Park, E. J. Kim, and J. H. You, "Best facilitated cortical activation during different stepping, treadmill, and robot-assisted walking training paradigms and speeds: a functional near-infrared spectroscopy neuroimaging study," *NeuroRehabilitation*, vol. 38, no. 2, pp. 171–178, 2016.
- [80] K. L. M. Koenraadt, E. G. J. Roelofsen, J. Duysens, and N. L. W. Keijsers, "Cortical control of normal gait and precision stepping: an fNIRS study," *Neuroimage*, vol. 85, pp. 415–422, 2014.
- [81] C.-F. Lu, Y.-C. Liu, Y.-R. Yang, Y.-T. Wu, and R.-Y. Wang, "Maintaining gait performance by cortical activation during dual-task interference: a functional near-infrared spectroscopy study," *PLoS One*, vol. 10, no. 6, Article ID e0129390, 2015.

- [82] I. Maidan, F. Nieuwhof, H. Bernad-Elazari et al., “The role of the frontal lobe in complex walking among patients with Parkinson’s disease and healthy older adults,” *Neuro-rehabilitation and Neural Repair*, vol. 30, no. 10, pp. 963–971, 2016.
- [83] M. J. Kurz, T. W. Wilson, and D. J. Arpin, “Stride-time variability and sensorimotor cortical activation during walking,” *Neuroimage*, vol. 59, no. 2, pp. 1602–1607, 2012.
- [84] F. G. Metzger, A.-C. Ehlis, F. B. Haeussinger et al., “Functional brain imaging of walking while talking—an fNIRS study,” *Neuroscience*, vol. 343, pp. 85–93, 2017.
- [85] I. Hausdorff, H. C. Tanabe, I. Sase et al., “Cortical mapping of gait in humans: a near-infrared spectroscopic topography study,” *Neuroimage*, vol. 14, no. 5, pp. 1186–1192, 2001.
- [86] M. Shimizu, I. Miyai, T. Ono, and K. Kubota, “Activities in the frontal cortex and gait performance are modulated by preparation. An fNIRS study,” *Neuroimage*, vol. 39, no. 2, pp. 600–607, 2008.
- [87] M. Suzuki, I. Miyai, T. Ono et al., “Prefrontal and premotor cortices are involved in adapting walking and running speed on the treadmill: an optical imaging study,” *Neuroimage*, vol. 23, no. 3, pp. 1020–1026, 2004.
- [88] F. Nieuwhof, M. F. Reelick, I. Maidan et al., “Measuring prefrontal cortical activity during dual task walking in patients with Parkinson’s disease: feasibility of using a new portable fNIRS device,” *Pilot and Feasibility Studies*, vol. 2, no. 1, p. 59, 2016.

Research Article

Modular Organization of Muscle Synergies to Achieve Movement Behaviors

Kunkun Zhao ^{1,2}, Zhisheng Zhang ¹, Haiying Wen,¹ Zihan Wang,³ and Jiankang Wu ^{2,3}

¹School of Mechanical Engineering, Southeast University, Nanjing, Jiangsu 211189, China

²CAS (Nanjing) Digital Health Industrial Technology Research Institute, Nanjing, Jiangsu 210046, China

³School of Electronic, Electrical Communication Engineering, University of Chinese Academy of Sciences, Beijing 101407, China

Correspondence should be addressed to Zhisheng Zhang; oldbc@seu.edu.cn

Received 17 September 2019; Accepted 21 October 2019; Published 15 November 2019

Guest Editor: Abbas AlZubaidi

Copyright © 2019 Kunkun Zhao et al. This is an open access article distributed under the Creative Commons Attribution License, which permits unrestricted use, distribution, and reproduction in any medium, provided the original work is properly cited.

Muscle synergy has been applied to comprehend how the central nervous system (CNS) controls movements for decades. However, it is not clear about the motion control mechanism and the relationship between motions and muscle synergies. In this paper, we designed two experiments to corroborate the hypothesis: (1) motions can be decomposed to motion primitives, which are driven by muscle synergy primitives and (2) variations of motion primitives in direction and scale are modulated by activation coefficients rather than muscle synergy primitives. Surface electromyographic (EMG) signals were recorded from nine muscles of the upper limb. Nonnegative matrix factorization (NMF) was applied to extract muscle synergy vectors and corresponding activation coefficients. We found that synergy structures of different movement patterns were similar ($\alpha = 0.05$). The motion modulation indexes (MMI) among movement patterns in reaching movements showed apparent differences. Merging coefficients and reconstructed similarity of synergies between simple motions and complex motions were significant. This study revealed the motion control mechanism of the CNS and provided a rehabilitation and evaluation method for patients with motor dysfunction in exercise and neuroscience.

1. Introduction

A large amount of research has reported that the CNS uses a dimensionality reduction pattern to coactivate a set of motion primitives (MP) to achieve daily activity living (DAL). However, motor control is redundancy and we could achieve a specific motion by combining various activation muscles [1]. How the CNS selects primitives from a vast pool and achieves movement behaviors is a complicated issue in the field of movement neuroscience and neurorehabilitation.

Modularity or muscle synergy as a building block, both structural and computational, exhibited feasibility for achieving motion control [2]. It has been proven in animal experiments, such as in cats, frogs, and monkeys. d'Avella [3] analyzed the movements of frogs during jumping, swimming, and walking in naturalistic conditions and found three shared and two task-specific muscle synergies across behaviors. Research in rhesus macaques showed that the

grasping and transporting movements were achieved by modulating the muscle synergies [4, 5]. Ting and Macpherson [6] analyzed the postural and balance control of cats and found that muscle synergies were correlated to the movement direction and endpoint force.

The modularity of motion control was also found in human motions. The study in various human locomotions, consisting of walking and running at different speeds, walking forward or backward, and walking under different loading conditions and different styles (rectilinear and curvilinear trajectories) [7, 8], showed that motions were driven by combining a few muscle synergy primitives. Shared and task-specific muscle synergies were also found in human locomotion [9, 10]. And, Barroso found muscle synergies merging in human walking and cycling [11], and cycling synergies are a linear combination of walking synergies. In the clinical research of stroke, decomposing and merging were more evident [12]. Comparing to the lower

limb, the upper limb movement is more complicated and exquisite. d'Avella et al. [13, 14] analyzed and summarized the movements of point-to-point at different speeds, loads, forearm postures, and via-point movements, showing that the CNS achieved a goal by combining a set of building blocks (muscle synergy primitives). Israely et al. [15] studied the muscle synergy modulation function of hand-reaching tasks from different directions and found a representative set of synergies, which were from the muscle synergies extracted from the center of the reaching space, which could be modulated to achieve motions in different directions. Similar results were found in poststroke [12, 15]. However, there was little research on the relationship between movement patterns and muscle synergies. Besides, the relationship between simple motions and complex motions is ambiguous. A deeper understanding of motion control in modularity is necessary.

In this paper, we would mainly analyze the relationship between muscle synergies and motion primitives. Based on the prior research, two hypotheses are tested: (1) any motion can be decomposed to motion primitives, which are driven by muscle synergy primitives and (2) variations of motion primitives in direction and scale are modulated by activation coefficients rather than muscle synergy primitives.

2. Materials and Methods

2.1. Subjects. Twenty-eight subjects with no neurological injury (male: eleven, female: seventeen, and age: 23.68 ± 1.74 years) were recruited for the study. All subjects are right-hand dominant. They were informed about the procedure and possible discomfort before giving their informed consent. The research was approved by the ethical committee of the university.

2.2. Experiment Procedures. Two experiments were designed for corroborating hypotheses. The first experiment (E1) consisted of three simple upper limb motions (SM) and five complex upper limb motions (CM). The simple motions included shoulder flexion/extension, shoulder abduction, and elbow flexion/extension. The complex motions covered touching head in the sagittal plane and the frontal plane, respectively, putting one hand behind the back, and shoulder pushing up in the sagittal plane and the frontal plane, respectively. All participants stood in the anatomic pose. More detailed motion information was illustrated by Pan et al. [12]. All subjects participated in the E1. The second experiment (E2) [16] was carried out in eleven male subjects. The subjects for E2 were instructed to execute reaching movements in six directions and three distances in a horizontal plane in a seating pose. Repeating the procedure six times for every reaching movement, 108 ($3 \times 6 \times 6$) trials were performed for every subject.

2.3. Data Collecting and Preprocessing. Surface electromyographic (EMG) signals were recorded (Trigno Wireless EMG System, Delsys, USA) from nine dominant muscles of the right upper limb, including triceps brachii long and lateral head

(TriLong and TriLat); pectoralis major (Pecm); deltoid anterior, medial, and posterior (DeltA, DeltM, and DeltP); trapezius upper (TrapUpper); biceps brachii (Bic); and brachioradialis (Brad). Electrodes were placed longitudinally along with the muscle fiber direction on corresponding muscles based on the guidelines of the Surface Electromyography for the Non-invasive Assessment of Muscles (SENIAM) [17].

Before the EMG processing, we eliminated the recordings contaminated due to disturbance and noise. Then, raw EMG signals were high-pass filtered (5th order Butterworth filter, the cutoff frequency of 50 Hz), zero-meaned, rectified, low-pass filtered (5th order Butterworth filter, the cutoff frequency of 5 Hz), and integrated over 20 ms [3, 11, 16]. To facilitate comparison across subjects, the EMG envelope was normalized by the average of the top 10 maximum of each muscle from every individual [11].

2.4. Data Analysis

2.4.1. Extracting Muscle Synergies. Muscle synergy theory assumes that EMG patterns can be described as a linear combination of a set of muscle synergies (time invariant) activated by corresponding activation coefficients (time variant). It can be described as follows:

$$E_{m \times t} = W_{m \times n} C_{n \times t} + e_{m \times t}, \quad (1)$$

where $E_{m \times t}$ is the preprocessed EMG, m is the number of muscles, and t is the number of sampling. $W_{m \times n}$ specifies the spatial profiles of activation, named the muscle synergy matrix, n is the number of muscle synergies. $C_{n \times t}$ is the activation coefficient, which is time varying. $e_{m \times t}$ is the error of reconstruction. We applied the nonnegative matrix factorization (NMF) [18] to extract muscle synergies. To avoid W and C converge to a local minimum, we repeated 50 times for each synergy.

2.4.2. Determining the Minimum Number of Muscle Synergy. The NMF algorithm starts with an initialized n . We increased the number of muscle synergy from one to nine. Reconstruction quality was evaluated by calculating the variance accounted for (VAF) [14]. The structure of muscle synergy was affected by the minimum number of synergy. To reconstruct the EMG patterns better and decrease the dimensionality of the muscle synergies, two criteria were applied. Criteria 1: the minimum of muscle synergy was defined as the number that the total VAF was greater than 95% [12] (in the E2, VAF > 90% [19]) and criteria 2: an additional synergy did not contribute more than 5% in the reconstruction of the EMG envelope. The VAF is defined as follows [20]:

$$\text{VAF} = 1 - \frac{\sum_{i=1}^m \sum_{j=1}^t (e_{i,j})^2}{\sum_{i=1}^m \sum_{j=1}^t (E_{i,j})^2}. \quad (2)$$

2.4.3. Evaluating the Similarity and Merging the Synergies. Before calculating the synergies similarity, we first matched the muscle synergy vectors from all synergy sets adopting the

Hungarian algorithm [21]. The Pearson correlation coefficient ($r_{i,j}$) and cosine similarity ($s_{i,j}$) were used to assess the similarity of synergy vectors. To identify how the synergies extracted from complex motions were reconstructed by the linear combination of synergies extracted from simple motions, we applied the algorithm proposed by Cheung et al. [22], in

$$w_i^{\text{CM}} = \sum_{k=1}^{n_{\text{SM}}} m_k^i w_k^{\text{SM}}, \quad m_k^i \geq 0, \quad i = 1, \dots, n_{\text{CM}}, \quad (3)$$

where w_i^{CM} is the i th synergy vector from a complex motion, w_k^{SM} is the k th synergy vector from simple motion, and m_k^i is a nonnegative coefficient which denotes contributions of the k th synergy vector from simple motion for the structure of i th synergy vector from the complex motion.

2.4.4. Motion Modulation Indexes (MMI). In the E2, we executed reaching movements in different directions and distances. To assess the modulating extent of activation coefficients among motion patterns, the motion modulation indexes were applied. We applied two indexes, root mean square of modulating signals (RMS-MS) and the VAF of synergy (VAF-Syn). RMS-MS represented an absolute activation degree, and VAF-Synergy ($\text{VAF}_i^{\text{syn}}$) showed a relative activation degree. The two indexes could give an objective description of modulation. For one synergy, the $\text{VAF}_i^{\text{syn}}$ is defined as [16]

$$\text{VAF}_{S_i} = \frac{\sum_{i=1}^m \sum_{j=1}^t (WC - w_i c_i^T)^2}{\sum_{i=1}^m \sum_{j=1}^t (E_{i,j})^2}, \quad (4)$$

$$\text{VAF}_i^{\text{syn}} = \frac{\text{VAF}_{S_i}}{\sum_{i=1}^N \text{VAF}_{S_i}},$$

where w_i is the i th muscle synergy and c_i^T is the corresponding activation coefficient. VAF_{S_i} and $\text{VAF}_i^{\text{syn}}$ are the VAF and the synergy VAF of the i th muscle synergy, respectively.

3. Results

3.1. Analysis of E2

3.1.1. Extracting Muscle Synergies. The VAF is shown in Figure 1. According to the criteria described above, we identified three synergies (2.82 ± 0.40 , corresponding VAF is 0.94 ± 0.01) in reaching movement (E2) for further analysis. Figure 2 exhibits three synergy structures extracted from preprocessed and pooled EMG data. Every synergy activated certain muscles corresponding to the upper limb motion. The first synergy mainly drove the shoulder flexion/abduction and internal rotation (Pecm and DeltA) and elbow flexion (Bic). The second synergy typically involved the movement of elbow extension (TriLat and TriLong), shoulder abduction (DeltM and DeltP), shoulder external rotation (DeltP), and shoulder extension (TriLat, TriLong, and DeltP). The third synergy covered the elbow flexors (Brad and Bic) and TrapUpper.

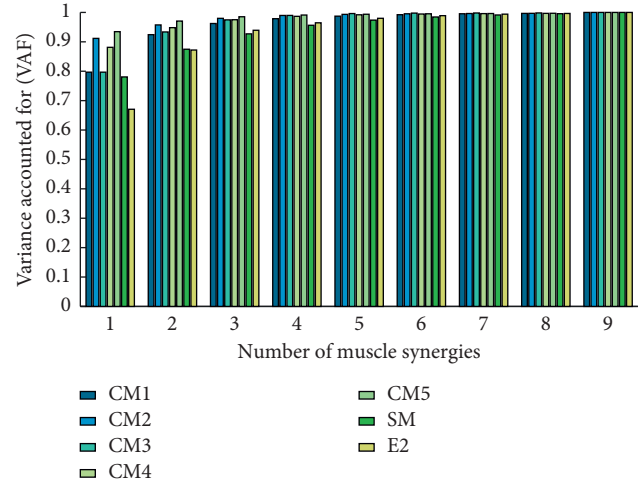


FIGURE 1: The variance accounted for (VAF) with respect to the number of muscle synergies. Colored bars indicate different motion patterns, respectively. Muscle synergies were extracted by the NMF algorithm. For reaching movement (E2), three synergies were extracted from the concatenated ENG. We extracted four synergies from concatenated simple motions (SM). 3, 2, 3, 2, and 2 synergies were extracted from five complex motions (CM1, CM2, CM3, CM4, and CM5), respectively.

The cosine similarity (s) and the Pearson correlation coefficient (r) between synergy vectors from all subjects are shown in Table 1. Results showed that the parallel synergy vector in all subjects was relevant. t -test results also illustrated that there was no significant difference among synergy vectors ($\alpha = 0.05$).

3.1.2. Similarity Analysis in Different Directions and Distances. To compare the variance of synergy vectors from different directions and distances, t -test was performed. Figure 3 shows the mean p values of the t -test among directions (a) and distances (b). Results showed that all p values were greater than 0.54 in directions (Table 2) and 0.59 in distances (Table 3), indicating that the synergy vectors from all directions and distances were from a population. Then, we concatenated the data from all directions and distances, respectively. The t -test results showed that there was also no significant correlation in all directions and distances. For every synergy in six directions (Table 2), the average p values are 0.71 ± 0.21 , 0.70 ± 0.21 , and 0.73 ± 0.19 ($\alpha = 0.05$, $n = C_{66}^2 = 2145$). And for every synergy in three distances (Table 3), the corresponding average p values are 0.69 ± 0.24 , 0.78 ± 0.16 , and 0.72 ± 0.19 ($\alpha = 0.05$, $n = C_{33}^2 = 528$), respectively.

3.1.3. Motion Modulation Indexes (MMI). The MMI for every direction and distance are shown in Figure 4. We found that every synergy was activated mainly in certain directions or distances. For example, the first synergy was activated mainly in 0 and -45 direction. The second synergy was in the direction of 45, 90, 135, and 180. The third synergy was activated in all directions. In terms of distances, the first

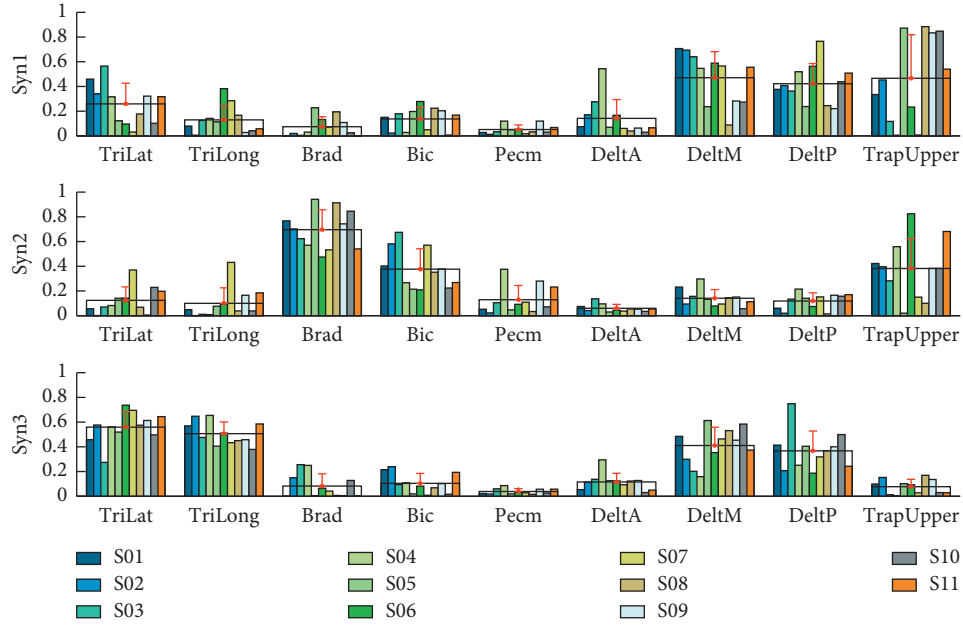


FIGURE 2: The structure of muscle synergies extracted from reaching movement. Colored bars indicate different subjects (11), and each muscle is shown in a group. Black wireframes and red bars are the group mean and standard deviation, respectively.

TABLE 1: Cosine similarity (s) and Pearson correlation coefficient (r) among synergy vectors from all subjects and the t -test results. The null hypothesis is that the synergy vectors come from a population ($\alpha = 0.05$, $N = C_{11}^2 = 55$).

Synergies	s	r	t -test
Syn1	0.94 ± 0.04	0.91 ± 0.07	0.56 ± 0.24
Syn1	0.93 ± 0.04	0.81 ± 0.12	0.80 ± 0.16
Syn1	0.85 ± 0.09	0.73 ± 0.16	0.73 ± 0.19

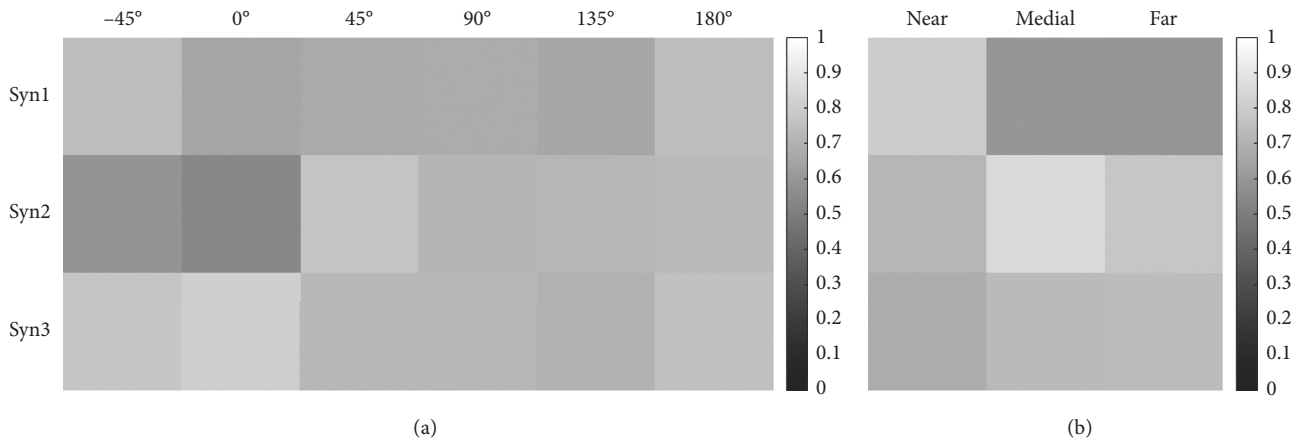


FIGURE 3: t -test results from six directions (a) and three distances (b) among all subjects. The samples are 55 (C_{11}^2). The deeper color indicates a smaller p value.

TABLE 2: t -test results from six directions ($n = 2145$, $\alpha = 0.05$).

Synergies	-45°	0°	45°	90°	135°	180°
Syn1	0.75 ± 0.18	0.65 ± 0.21	0.67 ± 0.19	0.68 ± 0.28	0.66 ± 0.27	0.75 ± 0.24
Syn2	0.59 ± 0.23	0.54 ± 0.28	0.77 ± 0.17	0.71 ± 0.22	0.72 ± 0.20	0.73 ± 0.18
Syn3	0.77 ± 0.17	0.81 ± 0.14	0.72 ± 0.22	0.72 ± 0.20	0.70 ± 0.24	0.75 ± 0.18

TABLE 3: *t*-test results from three distances ($n = 528$, $\alpha = 0.05$).

Synergies	Near	Medial	Far
Syn1	0.79 ± 0.17	0.60 ± 0.26	0.59 ± 0.27
Syn2	0.72 ± 0.19	0.85 ± 0.12	0.77 ± 0.16
Syn3	0.68 ± 0.20	0.73 ± 0.19	0.74 ± 0.18

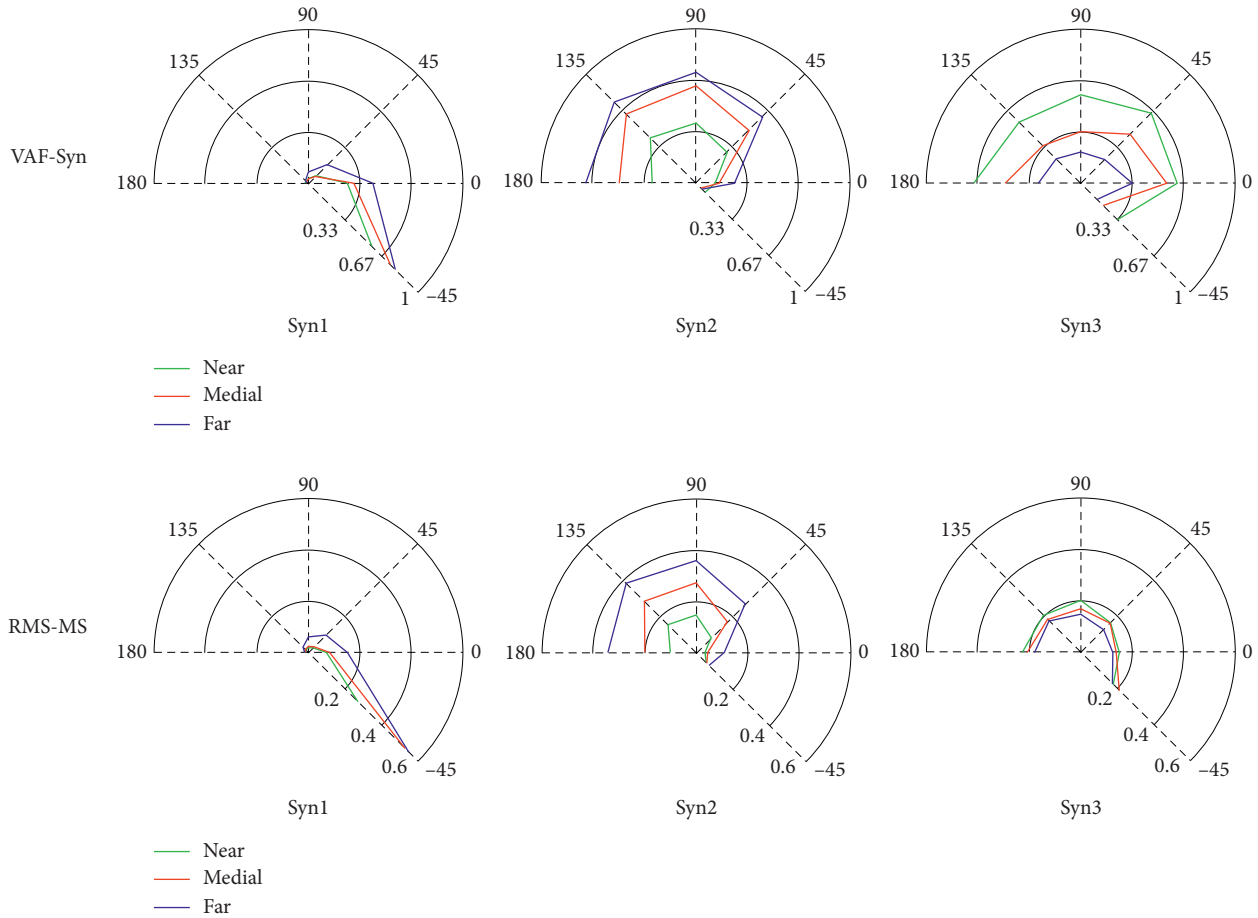


FIGURE 4: The radar map of MMI for three synergies (Syn1, Syn2, and Syn3). The first row is the VAF of synergy (VAF-Syn), and the second row is the root mean square of modulation signals (RMS-MS). Each column corresponds to a synergy. The radar map shows the six directions (-45 , 0 , 45 , 90 , 135 , and 180), and colored lines indicate different distances (near, medial, and far).

two synergies showed similar trends, i.e., the farther the distance, the greater the MMI. However, the third synergy exhibited the inverse characters, i.e., the farther the distance, the smaller the MMI. Two criteria, VAF-Syn and RMS-MS, demonstrated similar characters.

3.2. Analysis of E1

3.2.1. Extracting Muscle Synergies. For E1, we preprocessed the raw EMG data according to the abovementioned methods. However, the threshold was set 0.95 for determining the number of minimum synergies. Four synergies were selected for simple motion and 3, 2, 3, 2, and 2 synergies were identified for every complex motion, respectively (Figure 1): more specifically, 4.11 ± 0.63 , 3.11 ± 0.50 , 2.21 ± 0.57 , 2.71 ± 0.66 ,

2.43 ± 0.57 , and 1.82 ± 0.55 . The spatial structure of muscle synergies from every motion pattern is shown in Figure 5. For simple motion, the first synergy mainly activated shoulder abductor (DeltA and DeltM) and TrapUpper, which drove the motion of shoulder abduction. The second synergy primarily stimulated elbow flexor (Bic and Brad), which actuated the motion of elbow flexion. The third synergy drove the shoulder and elbow extension (TriLat, TriLong, DeltM, and DeltP). The fourth synergy led to the motion of shoulder flexion (Pecm and DeltA). For every complex motion, every synergy chiefly activated certain muscles also, which actuated similar upper motions.

t-test analysis was conducted among the subjects ($\alpha = 0.05$). The synergy similarity among subjects is shown in Figure 6. The results rejected the null hypothesis (the sample data come from a population). We analyzed the

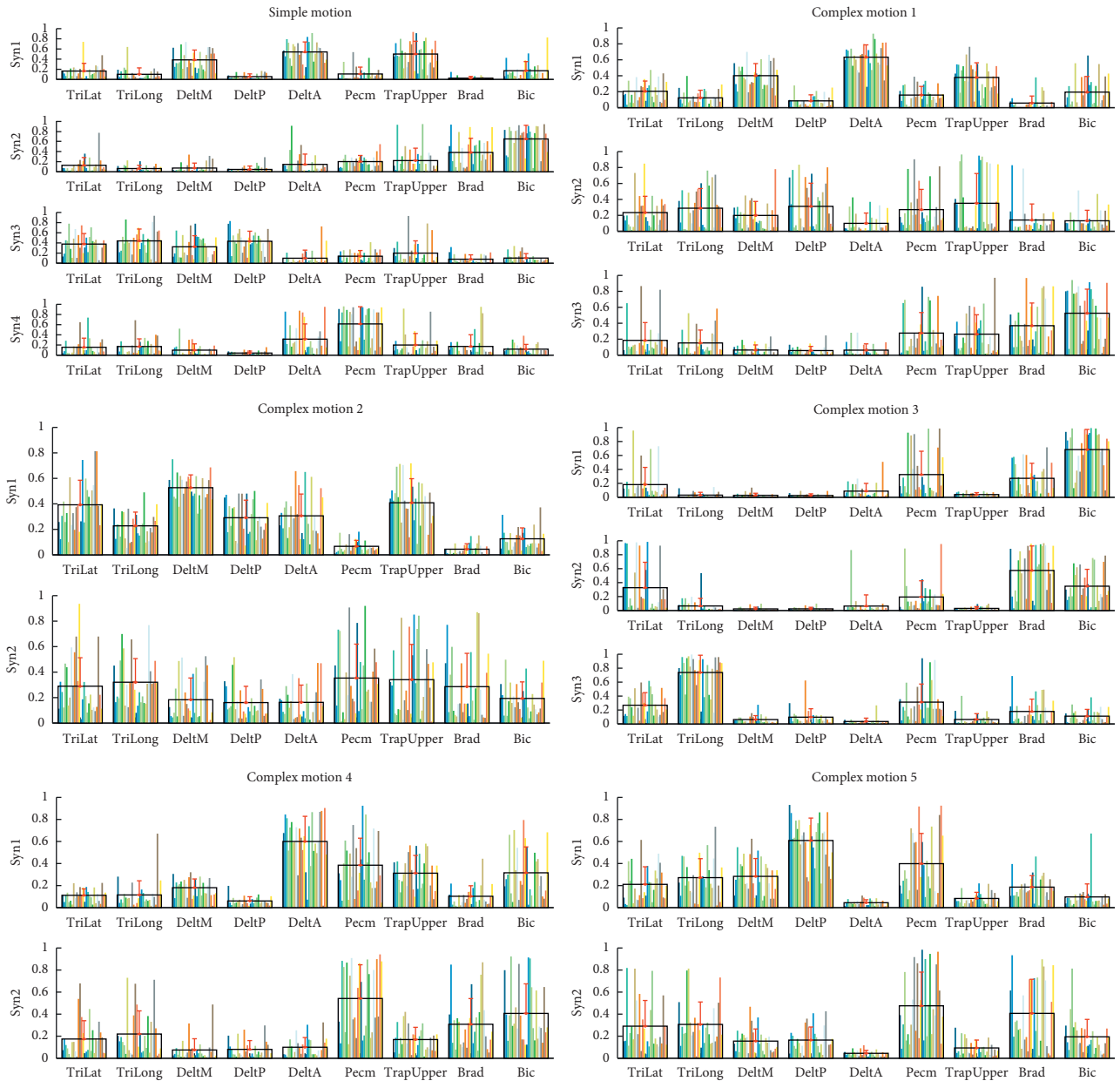


FIGURE 5: Synergy structures extracted from concatenated simple motion and complex motions. Four synergies were extracted from simple motion, and 3, 2, 3, 2, and 2 synergies were extracted from five complex motions, respectively. Colored bars indicate different subjects (28 subjects for E2). Black wireframes are group means, and red bars are standard deviation.

synergy similarity of all complex motions given in Table 4. A paired synergy is considered significantly correlated if the p is >0.5 . We found that the synergy structure exhibited correlations between CM1 and CM2, and CM4 and CM5. However, the first synergy from CM4 and CM5 displayed a negative correlation.

3.2.2. Analysis of Synergy Similarity between Simple Motion and Complex Motions. The similarity of every extracted synergy between complex motions and the simple motion was computed by cosine similarity (Figure 7). Table 5 shows the average of synergy similarity that every complex motion relates to simple motion. The higher similarity was found

between the synergies from the complex motions and synergies from simple motion which composed the complex motion. For instance, touching head in the sagittal plane (CM1) consists of shoulder and elbow flexion. And, we found a greater similarity in the CM1-Syn1 and SM-Syn1, and CM1-Syn3 and SM-Syn2, which was similar in the synergy structure analysis (Figure 5: complex motion 1). We also found the merging process between simple motion and complex motions. Table 6 demonstrates the merging coefficients (Mer-Coe) and reconstructed similarity (ReSim). We considered that the merging process was significant when the Mer-Coe was higher than 0.3 [11]. The results displayed that all reconstructing similarity was higher than 0.8.

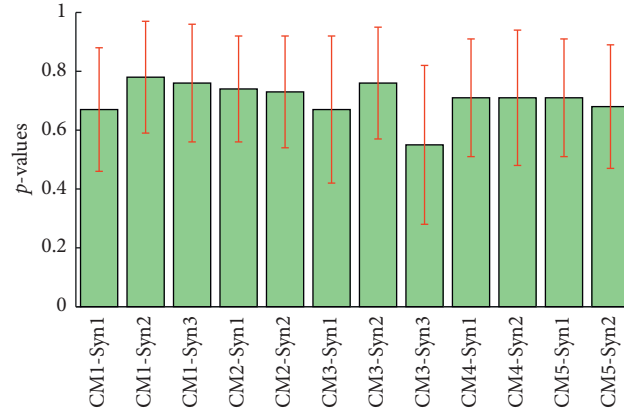


FIGURE 6: The synergy similarity among subjects from complex motions. The red bar indicates the standard deviation. CM1-Syn1 means the first synergy from complex motion 1. Other horizontal axis labels are similar.

TABLE 4: Similarity of the synergy among complex motions (CM1 and CM2, CM4 and CM5).

CM2	CM1			CM5		CM4	
	Syn1	Syn2	Syn3	Syn1	Syn2	Syn1	Syn2
Syn1	0.56	0.25	-0.64	Syn1	-0.53	-0.02	
Syn2	-0.35	0.51	0.30	Syn2	-0.34	0.73	

TABLE 5: Average of the synergy similarity between complex motions and simple motion.

	CM1	CM2	CM3	CM4	CM5
SM-Syn1	0.74	0.79	0.34	0.69	0.43
SM-Syn2	0.71	0.60	0.74	0.77	0.57
SM-Syn3	0.69	0.85	0.53	0.55	0.81
SM-Syn4	0.71	0.71	0.60	0.87	0.74

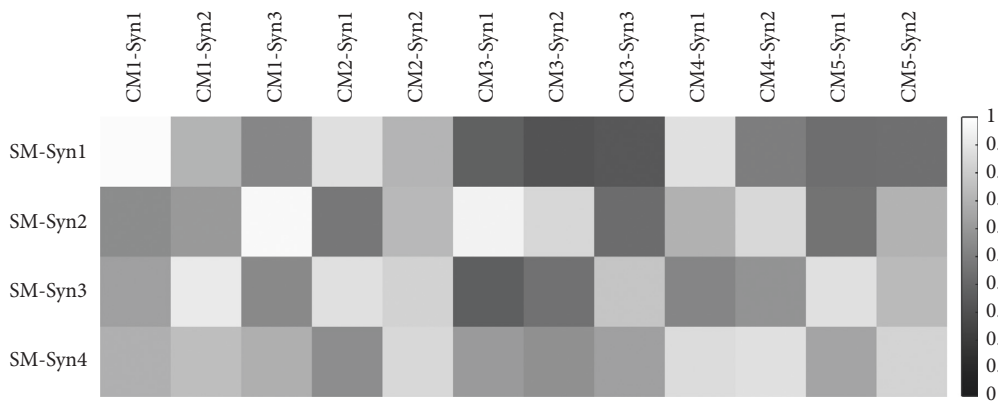


FIGURE 7: Cosine similarity of synergies between simple motion and complex motions. CM1-Syn1 means the first synergy from complex motion 1. SM-Syn1 expresses the first synergy from simple motion. Other abbreviations are sembable. A deeper color means a lower similarity.

4. Discussion

The purpose of this study was to investigate the relationship between muscle synergies and motion primitives of the upper limb motions. In previous studies, two muscle synergy

models, time-varying synergy and time-invariant synergy, were used to analyze muscle patterns [13, 23]. In our study, we extracted time-invariant muscle synergies adopting the NMF algorithm. Two experiments were designed, reaching movements and simple/complex motions. According to the

TABLE 6: Merging coefficients and reconstructed similarity.

SM-Syn	CM1			CM2			CM3			CM4		CM5	
	Syn1	Syn2	Syn3	Syn1	Syn2	Syn3	Syn1	Syn2	Syn3	Syn1	Syn2	Syn1	Syn2
SM-Syn1	0.93	0.06	0.00	0.59	0.02	0.00	0.00	0.00	0.00	0.52	0.00	0.00	0.00
SM-Syn2	0.00	0.10	0.81	0.00	0.25	0.90	0.71	0.00	0.18	0.48	0.00	0.25	0.25
SM-Syn3	0.04	0.58	0.10	0.60	0.44	0.00	0.07	0.64	0.00	0.07	0.78	0.35	0.35
SM-Syn4	0.11	0.24	0.12	0.00	0.42	0.07	0.07	0.33	0.48	0.57	0.26	0.50	0.50
ReSim	0.98	0.92	0.97	0.98	0.95	0.95	0.84	0.81	0.96	0.97	0.88	0.89	0.89

criteria predefined, we found three synergies were sufficient to explain >90% of the total variability of EMG activity of the nine studied muscles for reaching movements from eleven subjects. In the study of reaching movements of different conditions, three to five time-varying muscle synergies were extracted [24, 25]. The results were coincident with the prior study. For simple motion and complex motions, we just selected one or two synergies in the threshold of 0.9, which could not describe the spatiotemporal structure of the synergy. Thus, the threshold was set to 0.95, and we selected 4, 3, 2, 3, 2, and 2 synergies, respectively.

The study discussed the influence of directions and distances to muscle synergy in reaching movements (E2). *t*-test analysis (Tables 2 and 3) showed that synergies in different directions and distances were irrelevant. In the analysis of MMI, we found that RMS-MS and VAF-Syn exhibited resembled distributions in the radar map (Figure 4). The main performance was that the first synergy was activated mainly in the right and right rear motions. The second synergy mainly involved front, front-left, and left motions. However, the third synergy covered all directions. In the analysis of distance, the first two synergies displayed similar characters, farther distance with greater MMI. However, the third synergy showed an inverse character. We speculated that the third synergy was a shared synergy structure for reaching movements. The conjecture was verified by analyzing the synergy structure (Figure 2). The results revealed that the CNS controlled the motions in different patterns (directions and distances) by adaptively modulating the corresponding activation coefficients.

The E1 mainly analyzed the muscle synergy patterns of the simple motion and complex motions. *t*-test analysis showed synergy coincidence among subjects. However, there was one case which rejected the null hypothesis in CM3-Syn1, CM3-Syn2, CM3-Syn3, and CM5-Syn1, respectively ($n = C_{28}^2 = 378$). Considering the interference and noise of EMG signals, we thought the results were reliable.

The CM1 (touching head in the sagittal plane) could be decomposed into shoulder and elbow flexion. And, the CM2 (touching head in the frontal plane) included the simple motions of shoulder abduction and elbow flexion. The analysis of synergy similarity between CM1 and CM2 showed a positive correlation (>0.5) in the corresponding synergy. The synergy structure of the two motions (Figure 5) also displayed analogy. Semblable results were observed between CM4 and CM5. The results coincided with the conclusion in E2.

The similarity of synergy vectors was analyzed between simple motion and complex motions. The results verified

that the CNS controlled the motions by recruiting a set of muscle synergy primitives. Combining the study of reaching movements in E2, we knew that every muscle synergy pattern corresponded to a motion primitive.

As a quantitative assessment tool, muscle synergy has been used widely in motor neuroscience and rehabilitation neuroscience. However, the raw EMG signals are contaminated easily, and various preprocessing methods increase the difficulty to compare among researchers. Researchers have reported that experiment conditions have an effect on the envelope of the EMG, including speed, load, and posture [13]. In further work, we could study how the synergy modulates the motion in more conditions.

5. Conclusions

This study presented the possible patterns of the CNS controlling motions by two experiments, reaching movements in a horizontal plane and simple/complex motions. We applied the NMF to extract muscle synergies. Similarity analysis and *t*-test in muscle synergies indicated that the CNS modulated activation coefficients to achieve different motion patterns. Besides, for a complex motion, which included several motion primitives, the CNS recruited a set of muscle synergy primitives which drove the corresponding motion to coactivate the motion. Our results provided an interpretable strategy for the CNS controlling the motions. This would be a potential implication for evaluating and making rehabilitation plans in rehabilitation neuroscience.

Data Availability

The raw data used to support the findings of this study are available from the corresponding author upon request.

Conflicts of Interest

There are no conflicts of interest regarding the publication of this paper.

Acknowledgments

The authors would like to thank all the subjects and members from the Sensor Network and Application Research Center, School of Electronic, Electrical and Communication Engineering, University of Chinese Academy of Sciences, and the subjects who participated in the study. This work was supported by the Postgraduate Research and

Practice Innovation Program of Jiangsu Province (grant no. KYCX19_0061, 2019).

References

- [1] A. d'Avella, M. Giese, Y. P. Ivanenko, T. Schack, and F. Flash, "Modularity in motor control: from muscle synergies to cognitive action representation," *Frontiers in Computational Neuroscience*, vol. 9, p. 126, 2015.
- [2] R. E. Singh, K. Iqbal, G. White, and T. E. Hutchinson, "A systematic review on muscle synergies: from building blocks of motor behavior to a neurorehabilitation tool," *Applied Bionics and Biomechanics*, vol. 2018, Article ID 3615368, 15 pages, 2018.
- [3] A. d'Avella and E. Bizzi, "Shared and specific muscle synergies in natural motor behaviors," *Proceedings of the National Academy of Sciences*, vol. 102, no. 8, pp. 3076–3081, 2005.
- [4] S. A. Overduin, A. d'Avella, J. M. Carmena, and E. Bizzi, "Microstimulation activates a handful of muscle synergies," *Neuron*, vol. 76, no. 6, pp. 1071–1077, 2012.
- [5] S. A. Overduin, A. d'Avella, J. Roh, and E. Bizzi, "Modulation of muscle synergy recruitment in primate grasping," *Journal of Neuroscience*, vol. 28, no. 4, pp. 880–892, 2008.
- [6] L. H. Ting and J. M. Macpherson, "A limited set of muscle synergies for force control during a postural task," *Journal of Neurophysiology*, vol. 93, no. 1, pp. 609–613, 2005.
- [7] F. Lacquaniti, Y. P. Ivanenko, and M. Zago, "Patterned control of human locomotion," *The Journal of Physiology*, vol. 590, no. 10, pp. 2189–2199, 2012.
- [8] N. Chia Bejarano, A. Pedrocchi, A. Nardone et al., "Tuning of muscle synergies during walking along rectilinear and curvilinear trajectories in humans," *Annals of Biomedical Engineering*, vol. 45, no. 5, pp. 1204–1218, 2017.
- [9] G. Boccia, C. Zoppirolli, L. Bortolan, F. Schena, and B. Pellegrini, "Shared and task-specific muscle synergies of Nordic walking and conventional walking," *Scandinavian Journal of Medicine & Science in Sports*, vol. 28, no. 3, pp. 905–918, 2018.
- [10] M. M. Nazifi, H. U. Yoon, K. Beschoner, and P. Hur, "Shared and task-specific muscle synergies during normal walking and slipping," *Frontiers in Human Neuroscience*, vol. 11, p. 40, 2017.
- [11] F. O. Barroso, D. Torricelli, J. C. Moreno et al., "Shared muscle synergies in human walking and cycling," *Journal of Neurophysiology*, vol. 112, no. 8, pp. 1984–1998, 2014.
- [12] B. Pan, Y. Sun, B. Xie et al., "Alterations of muscle synergies during voluntary arm reaching movement in subacute stroke survivors at different levels of impairment," *Frontiers in Computational Neuroscience*, vol. 12, p. 69, 2018.
- [13] A. d'Avella, A. Portone, L. Fernandez, and F. Lacquaniti, "Control of fast-reaching movements by muscle synergy combinations," *Journal of Neuroscience*, vol. 26, no. 30, pp. 7791–7810, 2006.
- [14] A. d'Avella and F. Lacquaniti, "Control of reaching movements by muscle synergy combinations," *Frontiers in Computational Neuroscience*, vol. 7, p. 42, 2013.
- [15] S. Israely, G. Leisman, C. C. Machluf, and E. Carmeli, "Muscle synergies control during hand-reaching tasks in multiple directions post-stroke," *Frontiers in Computational Neuroscience*, vol. 12, p. 10, 2018.
- [16] L. Sun, B. Pan, S. Ye et al., "Modulation of muscle synergies with direction and distance during reaching movements," in *Proceedings of the 2019 9th International IEEE/EMBS Conference on Neural Engineering (NER)*. IEEE, pp. 1146–1150, San Francisco, CA, USA, March 2019.
- [17] H. J. Hermens, B. Freriks, R. Merletti et al., "European recommendations for Surface ElectroMyoGraphy," *Roessingh Research and Development*, vol. 8, no. 2, pp. 13–54, 1999.
- [18] D. D. Lee and H. S. Seung, "Algorithms for non-negative matrix factorization," in *Proceedings of the Advances in Neural Information Processing Systems*, pp. 556–562, Vancouver, BC, Canada, December 2001.
- [19] J. Roh, W. Z. Rymer, E. J. Perreault, S. B. Yoo, and R. F. Beer, "Alterations in upper limb muscle synergy structure in chronic stroke survivors," *Journal of Neurophysiology*, vol. 109, no. 3, pp. 768–781, 2013.
- [20] G. Torres-Oviedo, J. M. Macpherson, and L. H. Ting, "Muscle synergy organization is robust across a variety of postural perturbations," *Journal of Neurophysiology*, vol. 96, no. 3, pp. 1530–1546, 2006.
- [21] H. W. Kuhn, "The Hungarian method for the assignment problem," *Naval Research Logistics*, vol. 52, no. 1, pp. 7–21, 2005.
- [22] V. C. K. Cheung, A. Turolla, M. Agostini et al., "Muscle synergy patterns as physiological markers of motor cortical damage," *Proceedings of the National Academy of Sciences*, vol. 109, no. 36, pp. 14652–14656, 2012.
- [23] L. H. Ting and J. L. McKay, "Neuromechanics of muscle synergies for posture and movement," *Current Opinion in Neurobiology*, vol. 17, no. 6, pp. 622–628, 2007.
- [24] A. d'Avella, L. Fernandez, A. Portone, and F. Lacquaniti, "Modulation of phasic and tonic muscle synergies with reaching direction and speed," *Journal of Neurophysiology*, vol. 100, no. 3, pp. 1433–1454, 2008.
- [25] S. Israely, G. Leisman, C. Machluf, T. Shnitzer, and E. Carmeli, "Direction modulation of muscle synergies in a hand-reaching task," *IEEE Transactions on Neural Systems and Rehabilitation Engineering*, vol. 25, no. 12, pp. 2427–2440, 2017.